Stony Brook University

Studies of Quantum Transitions of Magnetic Flux in a rf SQUID Qubit

A Dissertation Presented

by

Luigi Longobardi

to

The Graduate School

in Partial Fulfillment of the Requirements

for the Degree of

Doctor of Philosophy

in

Physics

Stony Brook University

August 2009

Stony Brook University

The Graduate School

Luigi Longobardi

We, the dissertation committee for the above candidate for the Doctor of Philosophy degree, hereby recommend acceptance of this dissertation.

Dr. James E. Lukens – Dissertation Advisor
Professor, Department of Physics and Astronomy

Dr. Harold J. Metcalf – Chairperson of Defense
Distinguished Professor, Department of Physics and Astronomy

Dr. Dmitri V. Averin
Professor, Department of Physics and Astronomy

Dr. Francesco Tafuri
Associate Professor, Department of Information Engineering
Seconda Universitá di Napoli

This dissertation is accepted by the Graduate School.

Lawrence Martin
Dean of the Graduate School

Abstract of the Dissertation

Studies of Quantum Transitions of Magnetic Flux in a rf SQUID Qubit

by

Luigi Longobardi

Doctor of Philosophy

in

Physics

Stony Brook University

2009

At low temperature and low damping, the magnetic flux of a rf Superconducting QUantum Interference Device (SQUID) acts as a macroscopic quantum variable whose dynamic is described by a double well potential. A rf SQUID consists of a superconducting loop interrupted by a thin insulating barrier, known as a Josephson junction. The modified rf SQUID design discussed in this thesis has independent, in situ, controls that allow varying the barrier height between the potential wells and their relative tilt. This high level of control of the potential together with the capability to implement an experimental setup optimized to reduce coupling to external sources of noise, made this system ideal not only for tests of quantum transition at a macroscopic level, but also as a scalable solid state device for quantum computation.

A variety of measurements of quantum phenomena are reported in this thesis, including microwave level spectroscopy, coherent oscillations, and macroscopic resonant tunneling (MRT). These measurements are compared with theoretical models to study the pos-

sible sources of decoherence in a rf SQUID qubit. The analysis confirmed that the main source of decoherence is not due to coupling to the external environment, but it can be linked to intrinsic low frequency flux noise. Work from many groups over the last several years has shown that the performance of a superconductive qubit is limited by coupling to spurious defects in the materials used for the device fabrication. In this work we analyze the possibility of using the MRT as a tool for future studies of effects of materials and fabrication process in the realization of improved qubits, and we also explore the feasibility for measurements of quantum phenomena that involve fast pulsing of the potential barrier height.

To Rosa
In loving memory

Contents

List of Figures

List of Tables

Acknowledgements

Over the years spent in Stony Brook I have met many wonderful individuals that have made the accomplishment of the work here presented more bearable. To them I very much owe.

Above others I wish to thank my adviser Jim Lukens for his support, his patience, and encouragement. I have much profited form his guidance and experience.

I also need to acknowledge professor Kostya Likharev and professor Dima Averin for their insight and theoretical support.

I wish to thank all the other members of the research group for their help and friendship. Vijay Patel and Wei Chen who fabricated the devices and filters. Shawn Pottorf, Esteban Monge, Pete Davis, Pernille Jensen and all the crew of the machine and electronic shop for their assistance.

On a special note, I wish to acknowledge Douglas Bennett for the incredible contribution he has made to the measurements and the analysis.

I also need to thank all my friends for helping me keep some of my sanity. Especially I need to thank Manolo, Gerit, David, Nuria and Torsten for the great moments we have shared together and Sara Rombetto for, among other reasons, having read and revised this work.

Over the past few years I have been involved in many side projects without which I would have never come out of the lab. For these I need to thank Pedro and the artists at Gallery 4222, all the friends at the Graduate Student Organization, and the fantastic crew of the Hera Group. A big thank to Professor Sultan Hameed for volunteering to be the Hera Group's faculty advisor.

Finally I owe special thanks to my parents and my family for their constant encouragement.

Chapter 1

Introduction and Background

1.1 Introduction to Quantum Computing

All matter is composed of atoms whose interactions and dynamics are regulated by quantum mechanics, and although it is hard to recognize the peculiarity of the quantum world at a first glance, a closer look reveals that applications of quantum mechanics surround us. Without a clear quantum mechanical understanding of the solid state and the band theory of metals, insulators and semiconductors, the whole of the semiconductor industry with its transistors and integrated circuits, the building blocks of modern computers, could not have developed. The same applies to quantum optics and lasers and their applications to optical communications and to music and video compact disks.

A quantum computer represents yet another step closer to the exploitation of quantum mechanical effects to develop more modern and better technologies [1]. In an ordinary computer all the bits always have a definite state at any instant in time. In a quantum computer the ordinary bits are replaced by an ensemble of quantum two level system called quantum binary digits or qubits, and a quantum algorithm consists in the controlled evolution of the quantum state of the whole processor [2, 3]. Due to the superposition principle, a quantum computer could operate at the same time on a linear combination of several input data and give the output as a superposition of all the results.

The key to quantum algorithms is to take advantage of this intrinsic parallelism by following a superposition of computational paths and to produce a final state based on a quantum interference of all these paths [4], thus circumventing the projective nature of quantum measurements.

In just over 2 decades, since 1982 when Richard Feynman suggested that building computers based on the principles of quantum mechanics would avoid

the difficulty of simulating a quantum system on classical computers [5], the field of quantum computation has moved giant steps forward and it has been suggested that quantum computers have the potential to exceed the computational power of a classical computer [6]. The real strength of quantum computers seems to lie not in the perspective of building a faster computational machine (which is not at all demonstrated), but in the possibility to change the class of complexity of specific computational problems. For instance it has been demonstrated that quantum computers can outperform classical machines with Peter Shor's discovery of quantum algorithms for factorization of prime numbers and discrete logarithms that are exponentially faster than the known classical algorithms [7, 8] or with Grover's search algorithm [9]. The exponential speed increase in factoring large numbers is of special relevance since prime numbers factorization is at the basis of the current standard encryption system.

From the experimental point of view the implementation of a quantum processor is obviously a formidable task because quantum states are extremely fragile. The requirements for a physical implementation of a quantum computer are given by the following five "DiVincenzo criteria" [10]:

1. Scalability: a large number of reliable qubits is needed
2. The ability to efficiently initialize the qubit state (reset)
3. Quantum coherence: long coherence times compared to gate operation time
4. Availability of a universal set of quantum gates
5. High fidelity readout of individual qubits

Despite the existence of many two level quantum systems with well understood Hamiltonians, simultaneously satisfying all five criteria is actually very challenging. Most physical qubits can be classified as either microscopic systems like nuclear spins [11, 12], ions [13, 14] or atoms [15], which are intrinsically quantum and have long coherence times but are also not easily scalable, or macroscopic systems, like quantum dots [16] or superconducting circuits [17, 18], which are easily scalable with modern lithographic techniques, but not easily quantum, since they are strongly coupled to their environment which ultimately causes loss of quantum coherence.

The remainder of this thesis will be devoted to the description of macroscopic superconducting qubits, and in particular of a rf SQUID qubit designed and realized at Stony Brook University, with particular focus on quantum phenomena in a rf SQUID including measurements of macroscopic resonant tunneling and quantum coherence.

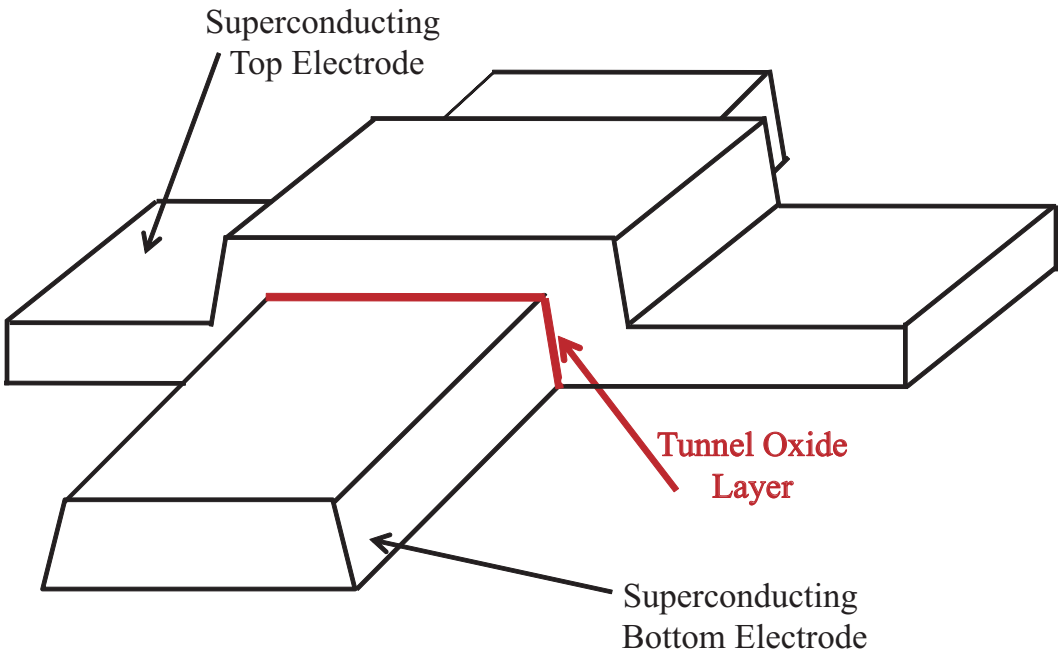

Figure 1.1: Cartoon of a Josephson tunnel junction.

1.2 Superconducting Qubits

Superconducting qubits are solid state electrical circuits that exploits the numerous advantages of using superconductors as well as the macroscopic quantum behavior of devices based on Josephson tunnel junctions [19] to engineer quantum states suitable for quantum computing. As shown in Fig. 1.1 a Josephson tunnel junction consists of an insulating tunnel barrier between two superconducting electrodes, and it can be characterized by its Josephson energy ($E_J = I_c\Phi_0/2\pi$), where I_c is the critical current of the Josephson junction and Φ_0 is a flux quantum, and the Coulomb charging energy ($E_C = (2e)^2/2C$) where e is the charge on the electron and C is the capacitance across the junction [20].

The first experimental evidence of quantum behavior in a Josephson tunnel junction came from measurements displaying energy levels quantization [21] and macroscopic quantum tunneling [22] in excellent agreement with theoretical predictions [23]. These experiments showed unequivocally that the phase difference between the phases of the superconductors constituting a Josephson junction is a quantum variable.

Superconductors are particularly suited to be used for quantum integrated circuits since they allow for design and fabrication of circuits using techniques

that can be borrowed from conventional integrated circuits, and they have intrinsically low dissipation and low noise due to the fact that the experiment are often conducted at millikelvin temperatures. For this latter property it should be noted that most superconducting qubits use energy levels spaced in the 5-20 GHz range and that 20GHz corresponds to a temperature of about 1K. Since it is important to operate the experiment at temperatures much lower than the energy spacing, dilution refrigerators are often involved in the experiments so that the devices are cooled to around 10-20mK. This allows one to also cool to these low temperatures the wires of the control and readout ports connected to the chip which require careful electromagnetic filtering. The quantum nature of these circuits is observable because they can be engineered to be isolated from the electrical environment and are thus represented by a single degree of freedom. Significant coupling to other degrees of freedom causes rapid decoherence, destroying the quantum state of the circuit so that it behaves classically, therefore proper filtering is of high importance.

Another key component of Josephson devices, that makes them ideal for qubit circuits is the fact that they have a strongly non-parabolic inductive potential energy. Superconducting qubits are not real two level system. In any possible implementation, the energy level spectrum of such qubits is more complex, therefore an anharmonic potential is important since it ensures that the transition frequency between the states constituting the qubit basis is sufficiently different from the transition between other eigenstates.

Ideally, each type of qubit is described by a single degree of freedom and they are usually divided in three main categories and are denominated phase, flux or charge qubits, depending on the macroscopic quantum variables describing the dynamics of the system which is basically determined by the E_J to E_C ratio.

A phase qubit is based on the difference of the superconducting phase across the Josephson junction as quantum degree of freedom and by E_J to E_C ratio much lager that one. Flux qubits, $E_J > E_C$, are based on the quantized flux in a superconducting loop interrupted by a Josephson junction. In some designs the geometrical inductance of the superconducting loop is replaced by a Josephson inductance, obtained by inserting 2 or 3 extra Josephson junctions in the superconducting loop. This design allows for implementing qubits that are physically smaller and therefore less sensitive to pick-up from stray external field, and is usually referred to also as a persistent current qubits. Charge qubits, $E_J \ll E_C$, are based on the number of cooper pairs on a superconducting island.

As already mentioned, superconducting qubits are macroscopic, so they could be expected to be very sensitive to decoherence. Obvious extrinsic

sources are related to the local electromagnetic environment: for example, contributions from the leads that are coupled to qubit bias and to read-out devices. These leads allow great flexibility in control of the system but they cause considerable coupling to the environment. This issue was promptly recognized and largely motivated the Caldeira-Leggett theory of quantum dissipation [23] which maps any linear dissipation onto a bath of harmonic oscillators. Clever engineering has greatly reduced, yet not fully removed, this source of decoherence.

The main limitation on the coherence of superconducting qubits is however intrinsic and results from low-frequency, '1/f' noise. Many 1/f noise sources can be well described by the Dutta-Horn model [24] as arising from a uniform distribution of two-state defects. Each defect produces random telegraph noise, and a superposition of such uncorrelated processes leads to a 1/f power spectrum.

There are three main sources of 1/f noise affecting superconducting qubits. The first is critical-current fluctuations, which are caused by the trapping and untrapping of electrons in the Josephson tunnel barrier [25]. These slow fluctuations modulate the energy-level splitting. All superconducting qubits are subject to dephasing by this mechanism which ultimately leads to decoherence. The second source of 1/f noise is charge fluctuations, which arise from the hopping of electrons between traps on the surface of the superconducting film or the surface of the substrate. This motion induces charges onto the surface of nearby superconductors. This decoherence mechanism is particularly problematic for charge qubits, except at the degeneracy point, where the qubits are (to first order) insensitive. The third source of 1/f noise is magnetic-flux fluctuations. Recently this source of noise has been associated to fluctuations of unpaired electron spins on the surface of the superconductor or substrate [26, 27], but the details of the mechanism remain controversial. Flux noise causes decoherence in flux qubits, except at the energy degeneracy point, as well as in phase qubits, which have no degeneracy point.

In general, all three low-frequency processes lead to decoherence. However, there is strong evidence that charge fluctuations can be associated with the high-frequency resonators that have been observed, in particular, in phase qubits [28]. Improvements in the quality of the oxide layers that are used in the junctions and capacitors have resulted in large reductions in the concentration of these high-frequency resonators [29].

The qubit object of this thesis is an rf SQUID with a tunable E_J, which is especially flexible and can be used as either a flux qubit or a phase qubit.

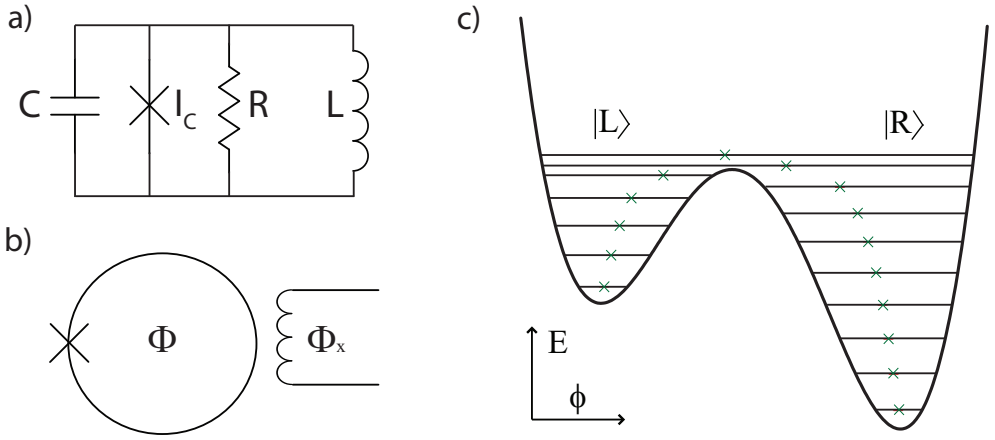

Figure 1.2: a) Equivalent lumped circuit for a rf SQUID. b) A schematic representation of a rf SQUID including an external flux bias coil. c) The potential of a rf SQUID at a $\beta_L = 1.32$ and $\phi_x = 0.505$ showing localized energy levels and the corresponding value of mean flux (green x).

1.3 The rf SQUID

In its simplest form a rf SQUID qubit consists of a superconducting ring of inductance L interrupted by a single Josephson junction with critical current I_c. A schematic of the equivalent circuit along with an external flux bias coil is shown in Fig. 1.2. The Josephson junction can be modeled as a non-linear circuit element I_c shunted by a capacitance C and a resistance R [30]. An external static flux (Φ_x) applied to the superconductive loop induces a screening current $I_s = -I_c \sin(2\pi\Phi/\Phi_0)$ where $\Phi_0 \equiv \frac{h}{2e}$ is the flux quantum and Φ is the screened flux linking the loop: $\Phi = \Phi_x + LI_s$ [20].

1.3.1 Classical Picture

The classical dynamics of this device (in terms of the flux Φ) is equivalent to the motion of a particle of mass C, moving, with damping R^{-1} in a potential $U(\Phi, \Phi_x)$:

$$C\ddot{\Phi} + \frac{\dot{\Phi}}{R} + \frac{\partial U(\Phi, \Phi_x)}{\partial \Phi} = 0 \tag{1.1}$$

The potential U is the sum of the loop's magnetic energy and of the Josephson junctions coupling energy. If the total and external flux are expressed in

units of $\Phi_0/2\pi$, this potential is [31, 32]

$$U(\phi, \phi_x) = U_0 \left[\frac{1}{2}(\phi - \phi_x)^2 + \beta_L \cos(\phi) \right], \tag{1.2}$$

where $U_0 \equiv \Phi_0^2/4\pi^2 L$, $\beta_L \equiv 2\pi L I_c/\Phi_0$.

For $1 < \beta_L < 4.6$ and ϕ_x near $1/2$, the potential, shown in Fig. 1.2c, has the form of a double well with the two wells representing different fluxoid states of the rf SQUID and having screening currents (of equal magnitude at the symmetry point, $\phi_x = 1/2$) circulating in opposite directions around the loop [32]. The net effect of changing ϕ_x is to tilt the double well potential. The two local energy minima can be calculated by minimizing equation (1.2) with respect to ϕ giving

$$\frac{dU(\phi, \phi_x)}{d\phi} = 0 \;\Rightarrow\; \phi_{min} = \phi_x - \beta_L \sin(\phi_{min}) \tag{1.3}$$

which must then be solved numerically for ϕ_{min}.

The small oscillation frequency at the bottom of one of the wells due to the oscillation of the current between the capacitance of the junction and the inductance of the loop can be calculated from the potential as:

$$\omega_p = \left(\frac{1}{C} \left(\frac{2\pi}{\Phi_0} \right)^2 \frac{\partial^2 U}{\partial \phi^2}\Big|_{\phi=\phi_m} \right)^{1/2} = \sqrt{\frac{1 + \beta_L \cos(\phi_{min})}{LC}} \tag{1.4}$$

This frequency of oscillation is called the plasma frequency and it sets the energy scale for the rf SQUID energy level structure.

1.3.2 Hamiltonian and Quantum Description

The quantum behavior of a rf SQUID may be studied by calculating its the energy levels and wavefunctions. In the limit of zero temperature and zero dampening the Hamiltonian of an isolated rf SQUID is [31, 33]

$$H(\phi, \phi_x) = \frac{Q^2}{2C} + U(\phi, \phi_x) \tag{1.5}$$

Since the charge on the junction, Q, is conjugate to the phase (or flux), $p_\phi = Q$ is the momentum operator conjugate to the position operator ϕ [30]. The Hamiltonian can be rewritten as the sum of a simple harmonic oscillator and

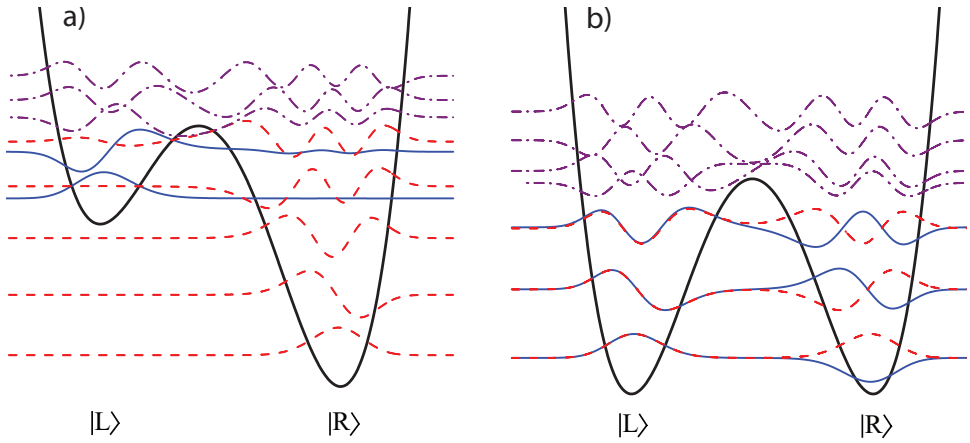

Figure 1.3: a) The potential of a rf-SQUID at a $\beta_L = 1.2$ and $\phi_x = 0.5038$ showing the eigenfunctions localized in the right well (red dashed line), left well (blue solid line) and above the barrier (purple dashed dotted line). b) The potential of a rf-SQUID at a $\beta_L = 1.2$ and $\phi_x = 0.5$ showing the symmetric (red dashed line) and antisymmetric (blue solid line) states and also states above the barrier (purple dashed dotted line)

a cosinusoidal term

$$H = \frac{-\hbar^2}{2C}\left(\frac{2\pi}{\Phi_0}\right)^2 \frac{\partial^2}{\partial\phi^2} + \frac{1}{2}U_0\left(\phi - \phi_x\right)^2 + E_J\cos(\phi) \tag{1.6}$$

where $E_J \equiv I_c\Phi_0/2\pi$.

It is possible to exploit the similarity of this hamiltonian to that of a simple harmonic oscillator, and the fact that the cosine term can be expressed in terms of raising, and lowering operators to construct a matrix in the basis states of the simple harmonic oscillator. This matrix can then be numerically diagonalized to find the eigenenergies and eigenstates of the rf SQUID [34]. This method of finding the energies and eigenstates was used extensively in the data analysis presented in this thesis. Using the Hermite polynomials it is also possible to extend this calculation to obtain the wavefunctions of the system. Figure 1.3 shows the results of doing this for a potential configuration with relatively low barrier ($\beta_L = 1.2$) and two different values of tilt. Figure 1.3a shows the wavefunction for a $\phi_x = 0.5038$. The wavefunction localized in the right well are plotted using red dashed lines while those localized in the left well are plotted using blue solid lines. It is clear from the figure that near the top of the barrier the wavefunctions begin to have some amplitude in the other well, and based on the value of the external flux bias, levels in opposite wells

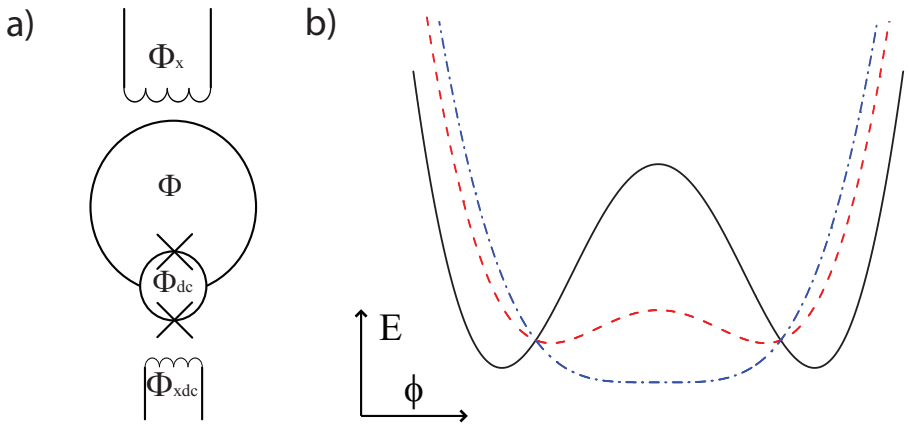

Figure 1.4: a) A schematic representation of a modified rf SQUID including an external Φ_{xdc} bias coil to allow for barrier height modulation in the potential. b) The potential energy of a rf SQUID at the symmetry point ($\phi_x = 1/2$) for L=189 pH and different barrier hieght corresponding to $\beta_L = 2.1$ (black solid), 1.4 (red dashed) and 1 (blue dash dot)

will approximately align resulting in eigenstates that are no longer localized in individual wells. An extreme case is shown in Fig. 1.3b for a fully symmetric potential at $\phi_x = 0.5$. In this case the symmetric wavefunctions are shown using a dashed red line while the antisymmetric wavefunctions are shown using a solid blue line. The fluxoid states are not eigenstates of the system but superpositions of the eigenstates, therefore if the system is initialized in one of the fluxoid states, the system will tunnel back and forth though the barrier and will oscillate between the fluxoid states.

Experimentally it is convenient to have the ability to adjust the height of the barrier of the double well potential independently of the tilt which is controlled by the external flux Φ_x. From a careful study of the potential it is possible to show that the height of the barrier is fixed by the critical current of the Josephson junction, however the critical current can be modulated if the single junction is replaced by two junctions in parallel in a superconductive loop, a dc-SQUID, with inductance ℓ. By applying flux to this loop using a dedicated bias coil, Φ_{xdc}, the critical current of the dc-SQUID can be suppressed allowing the barrier of the double well potential to be modulated. A schematic representation of a rf SQUID modified with the capability to modulate the barrier height is shown in Fig. 1.4. The addition of the dc SQUID turns the potential into a two dimensional potential. In terms of flux through

the two loops, ϕ and ϕ_{dc} such potential is given by [35]

$$\begin{aligned} U(\phi,\phi_{dc}) &= U_0[\frac{1}{2}(\phi-\phi_x)^2+\frac{1}{2}\gamma(\phi_{dc}-\phi_{xdc})^2 \\ &\quad +\beta_{L0}\cos(\phi_{dc}/2)\cos(\phi)-\delta_{Ic}\beta_{L0}\sin(\phi_{dc}/2)\sin(\phi)] \end{aligned} \tag{1.7}$$

where $\delta_{Ic} \equiv (I_{c2}-I_{c1})/(I_{c2}+I_{c1})$ represents the critical current asymmetry among the two junctions, $\gamma \equiv L/\ell$ is the ratio of the inductances of the rf and dc SQUID loops and ϕ_{dc} is the flux in the dc SQUID loop.

If the β_L for the small loop is much less then one and L is much bigger then ℓ (large γ), then the potential can be treated as one dimensional potential with small corrections [35–37] and the previous discussion for the treatment of the hamiltonian of the system still holds with the simple variation that the β_L in equation (1.2) can now be replaced with

$$\beta_L(\Phi_{xdc}) = \beta_{L0}\cos\left(\frac{\pi\Phi_{xdc}}{\Phi_0}\right) \tag{1.8}$$

where the maximum (β_{L0}) occurs at integer values of applied flux.

The ability to modulate the barrier height also offers extra flexibility when it comes to select the energy levels that one wishes to use as a basis for qubit operation with a rf SQUID. One can select either the lowest level in each well or the two lowest levels in a single well for the basis states of the qubit. The latter is referred to as the flux basis, since the two states have an easily measurable flux difference in the double well basis, and requires a relatively low barrier to provide adequate coupling between the states. The single well mode, on the other hand, requires a relatively high barrier so that the basis states do not couple to the states in the other well, and it also requires microwave radiation to couple the basis states. This mode of operation is very close to that of qubits commonly referred to as "phase" qubits. Except around the symmetry point, changes in ϕ_x cause a much greater change (about 100×) in the level spacing for the flux basis than for the phase basis. Therefore there is a strong advantage to the phase basis in terms of coherence times.

1.3.3 A Superconductive Qubit: The rf SQUID vs the DiVincenzo Criteria

To understand the viability of a rf SQUID as a superconducting qubit it is helpful to refer to the DiVincenzo criteria and check how a rf SQUID satisfies them:

1. Qubits have to be well defined, and the physical system has to be scalable.

There is no problem regarding the identifiable nature of superconducting qubits. By its very nature the microfabricated devices contain qubits identifiable by their spatial location and addressable via external control lines and circuits. One potential advantage of condensed matter qubits in general, in comparison to those made from more fundamental systems (such as nuclear spins, atoms and ions) is their inclination for scalability. Once the specific lithographic and fabrication techniques to realize one or few qubits have been mastered, they should also offer the possibility of producing many qubits. Fabricated qubits however will rarely be identical in the same way that fundamental systems, like two identical ions, can be [38]. On the other hand, fabrication does offer great flexibility and circuits can be designed to minimize certain environment couplings and to couple qubits as desired.

2. Qubits can be initialized in a predefined certain state.

For a rf SQUID and superconducting qubits in general, state preparation is relatively straightforward, since these kind of qubits clearly require operation at temperatures low compared to the typical energy level separations which will guarantee a low level of impurity of prepared states.

3. Low decoherence.

There are several sources of decoherence associated with rf SQUID and superconductive qubit in general, a short list comprise: (i) quasiparticle effects in the actual superconducting circuits; (ii) magnetic fluctuations due to nuclear spins in the solid both in the bulk of superconductive and dielectric materials and at the surface interface between the various deposition layers in the circuit fabrication; (iii) fluctuations/noise in the external sources coupled to qubits; (iv) unwanted but unavoidable coupling to other flux qubits.

Some of these sources, such as effects of the external electronic, including the readout mechanism, and intrinsic flux noise, have been already discussed in previous works [39, 40], for other (effects of materials and fabrication) the work is underway and some *ab initio* results and consideration will be reported in chapter 3. An important point about a rf SQUID is that it is only an approximation that it possesses an electromagnetic degree of freedom (the flux) which lives in a two dimensional Hilbert space. In practice, small amplitudes of states outside the truncated Hilbert space can arise and contribute in the

evolution of the quantum circuit, contribution which could be viewed as a contribution to the decoherence, however, superconductors, with all electrons governed by a single macroscopic wavefunction, are a good compromise between the efficient control and scalability typical of integrated circuits and the robustness to decoherence displayed by smaller quantum systems with fewer degrees of freedom.

4. Possibility to implement quantum gates.

rf SQUIDs and superconducting qubits in general offer the possibility not only to couple strongly to each other, but also to implement electronic means to turn on and off their interaction.

Various schemes have been reported to couple rf SQUID qubits that use direct coupling [41, 42], or through flux transformers [43] which enable the interaction of the qubits to be mediated over longer distances and also to be tuned, or through superconducting resonators used to create a 'quantum bus' [44], and simple quantum gates have also been demonstrated [45].

5. Capability of measuring each qubit separately.

For the rf SQUID discussed here the readout issue is solved by the use of an on-chip hysteretic dc SQUID magnetometer to measure the state of the qubit. Later in this thesis the readout mechanism will be discussed in detail. At this stage it is important to report that to ensure a high level of fidelity, the qubit state is frozen through manipulation of the bias applied to it, prior the readout, and that for many qubit system, once again the scalability of superconductive circuit fabrication technique allows for the realization of an individual readout for each qubit.

Chapter 2

Experimental Setup

2.1 Introduction

On what it is considered the normal scale of quantum mechanical objects, the rf SQUID constitutes a macroscopic system. As such it constantly interacts with its surroundings, its environment. The need for millikelvin temperatures, an ultralow-noise environment, and very sensitive measurement techniques, makes experiments on superconducting qubits very challenging. In order to measure quantum phenomena in a rf SQUID qubit it is important to design an experimental setup that allows to minimize the effects of noise and coupling from the environment on the qubit.

The experimental setup described in this chapter is able to achieve these goals while still maintaining a high level of flexibility. Thanks to a careful design of filtering and device isolation several types of quantum measurements have been performed with excellent reproducibility.

2.2 Experimental Design and Setup

The experiment is realized using a dilution refrigerator with a vacuum tight copper sample cell thermally anchored to the mixing chamber. The copper cell contains both the last stage of noise filtering and a NbTi cell which houses two chips. One chip contains the qubit, its low frequency bias lines, and a dc SQUID magnetometer that detects the flux states of the qubit; the other chip contains high frequency pulse lines used to couple fast flux pulses and microwave pulses to the qubit. Figure 2.1 shows a block diagram of the experimental setup including the room temperature electronic, filtering and the low temperature assembly.

The room temperature circuits have been optimized to minimize the effect

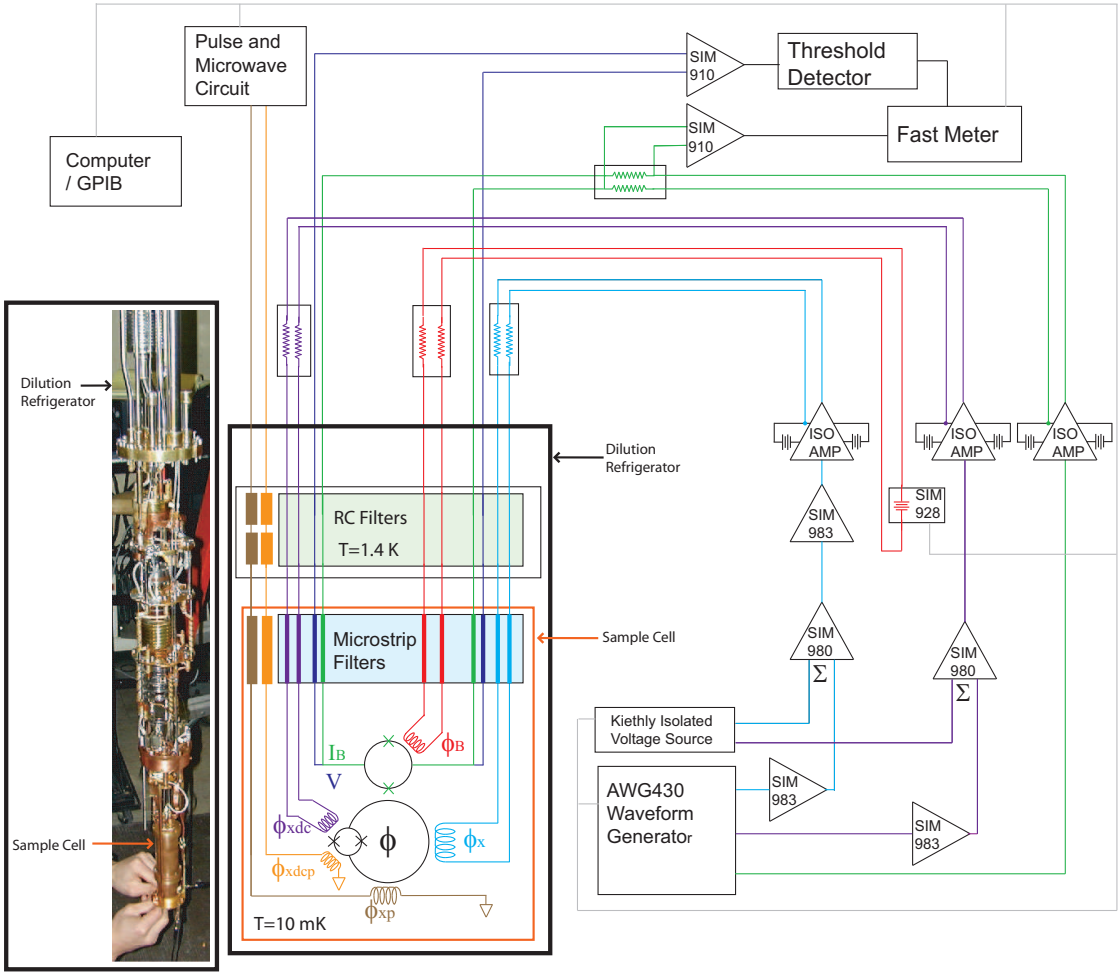

Figure 2.1: Schematic of measurement setup. The inset shows a photograph of the sample cell mounted on the dilution refrigerator

of unwanted noise on the qubit while performing control and measurements on the sample. Timing between the various sources is critical to the operation and readout of the qubit. The measurement and control lines consist of low frequency lines and high frequency transmission lines. The low frequency connections include the magnetometer current and voltage leads and three flux biases; one for the magnetometer (ϕ_B), and two for the qubit (ϕ_x and ϕ_{xdc}). The high frequency control lines are on a separate chip suspended over the qubit chip and supply further control of ϕ_x and ϕ_{xdc}.

2.2.1 Grounding, rf Shielding and Filtering

In order to avoid ground loops and noise pick up, the whole experiment is designed to have a single ground [46, 47]. All connections to the chip are floating and are only capacitively coupled to ground though the filters. All grounded signal sources pass through battery powered unity gain isolation amplifiers that effectively disconnects this signal from the earth ground. The current paths are all designed to be symmetric with respect to the chip to reduce the effect of common mode noise [47]. This allows for sufficient decoupling from the ground while keeping the amplifier from saturating due to charging by providing a return current path. The amplifiers are designed to have 100 $M\Omega$ of resistance between their inputs and the common of the battery circuit and use OPA111 [48] low noise Difet operational amplifiers and a INA105 output stage. All signals entering the fridge are isolated, shielded and filtered allowing the dilution refrigerator itself to act as an rf-shield for the cold portion of the experiment.

To further isolate the qubit from the effects of the environment all measurement and control lines must be heavily filtered to reduce the level of noise from room temperature electronics. The low frequency lines are filtered by EMI filters at room temperature, followed by cascaded RC filters anchored at 1 K, followed by specially designed microstrip filters at base temperature. The high frequency lines (both pulse and microwave) are filtered by a series of attenuators at 1.4 K (20 dB), 600 mK (10 dB) and at base temperature (10 dB) followed by microstrip filters that cutoff around 1 GHz.

Common RC filters only work up to some resonant frequency (usually less than 1 GHz) due to the parasitic inductance of the capacitor [49] therefore this type of filters do not work well against noise at frequencies in the GHz range and above. There are a number of distributed filters that can filter in this frequency range including copper powder filters, thermocoax and microstrip filters [50]. Copper powder filters work by using the skin effect in the individual copper grains to attenuate high frequencies [51]. Thermocoax uses the resistance of the cable to form a lossy transmission line [52].

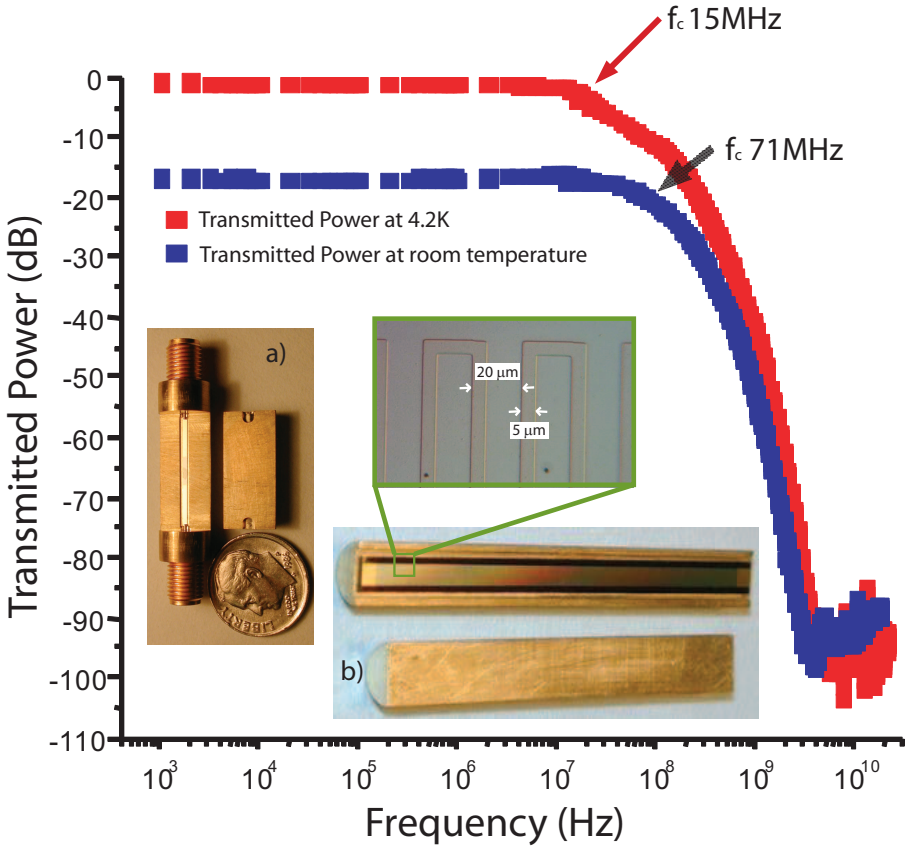

Figure 2.2: The Power transmitted through the lossy microstrip filter to a detector with a 50 Ω load at room temperature and at 4.2K. The insets are pictures of the lossy microstrip filter a) with and b) without the Nb meander line, inside their respective housings.

For the setup described in this thesis, lossy microstrip filters were developed that roll off faster than copper powder filters and do not require all the space that is necessary for thermocoax lines. The microstrips filters consist of a thin film of chromium deposited on a substrate and diced into long narrow chips. When the chips are placed in a brass housing, which acts as a ground plane, they form a lossy microstrip transmission line. Some of the bias controls for the qubit require currents of few milliamperes. Any non-negligible resistance on the lines passing such currents could cause joule heating of the filters and the sample. To avoid heating in the filters that need to pass dc currents, a superconducting shunt has been deposited on top of the chromium microstrip. The shunt is patterned as a meander line to give it a large enough inductance that it blocks high frequency signals while allowing dc currents to pass through without resistance. At high frequencies above the cutoff of the meander line, the current is filtered by the chromium microstrip.

Pictures of the filters in their housings are shown in Fig. 2.2 along with measurements of the transmitted power at room temperature and at 4.2K for a filter with a Nb meander line. At room temperature the Nb meander line is not superconducting and has a total resistance larger than the chromium therefore the current travels primarily through the chromium. This causes the 16 dB of attenuation shown by the data below 10 MHz. The cutoff, 71 MHz, is consistent with the designed cutoff of the lossy microstrip line. When the Nb goes superconducting the low frequency current is shunted through the meander line and the attenuation is that of the cables alone. The first cutoff at 15 MHz corresponds to the cutoff of the meander line while the second kink represents the cutoff of the microstrip.

The lossy microstrip filters are very flexible since the cutoff and attenuation level of the filters can be controlled using the dimensions and the resistivity of the microstrip and they may provide a way to effectively filter many signals over a wide ranges of frequencies.

2.2.2 Sample Cell

The millikelvin section of the experimental setup consists of a sample cell, shown in Fig. 2.3, housed in a sample can thermally grounded to the lowest temperature stage of a dilution refrigerator capable of reaching a base temperature of 5 mK. The sample can, shown in Fig. 2.4, has two chambers separated by an rf tight block which contains the microstrip filters and it is designed to be vacuum tight and it can be filled with a controlled amount of He^4 which provide thermalization of the qubit chips and microstrip filters similar to an exchange gas. To keep the can from leaking, all the twisted pairs and coaxial cables enter the cell through vacuum tight epoxy feedthroughs (Stycast 2850

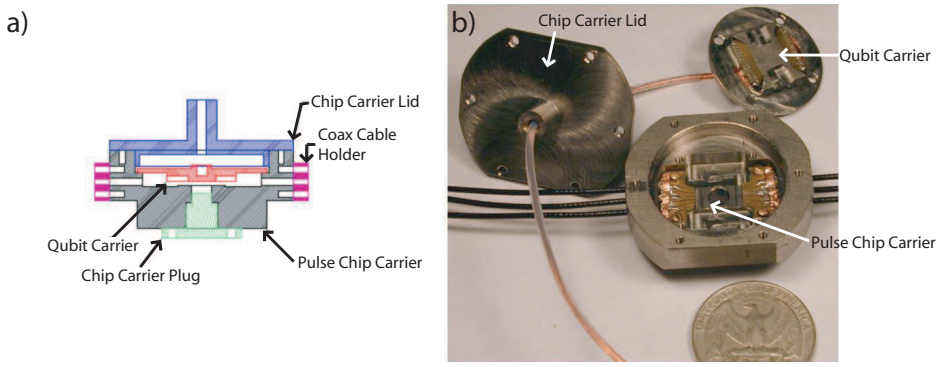

Figure 2.3: a) Drawings of the NbTi sample cell, b) a photograph of the cell before the devices where mounted.

FT) mounted on the top lid. The lid and bottom can are sealed to the center can using indium o-ring seals. Inside the bottom chamber of the sample can a sample cell can be mounted, designed to house the qubit chip and all the necessary wires and cables.

The sample cell is a superconducting NbTi can that acts as a magnetic shield below its transition temperature ($\approx 10K$). To prevent magnetic flux from trapping in the sample cell and to provide more protection from magnetic fields, a double layer Cryoperm shield is mounted to the mixing chamber of the dilution refrigerator outside the outer sample can. The Cryoperm shield is demagnetized below 77 K when its magnetic shielding is optimum but above the T_c of the sample cell.

The NbTi cell is shown in Fig. 2.3. The pulse chip is glued at the bottom of the cell using GE varnish while the qubit is mounted to a NbTi chip carrier. The electrical connections to the qubit and to the pulse chip are realized through two sets of specially designed bonding pads patterned on 1/32 inch thick PC boards made of FR-4. The qubit chip is wire bonded to its bonding pads which are soldered to copper wires that come through the back of the carrier and then exit the cell through a hole in the lid. The pulse chip is also bonded to its bonding pads that are then soldered to 0.047 inch flexible coaxial cables. The pulse chip is connected using three bonds for each line, this solution has been chosen since time domain reflectometry showed that it minimizes impedance mismatch.

The sample cell is designed so that the two chips can be aligned in a setup that allows them to be moved relative to each other while viewing the alignment with a microscope attached to a CCD camera from a hole in the bottom of the cell. There are two set of verniers and alignment marks patterned on each chip during fabrication that allow to control the alignment to within 1

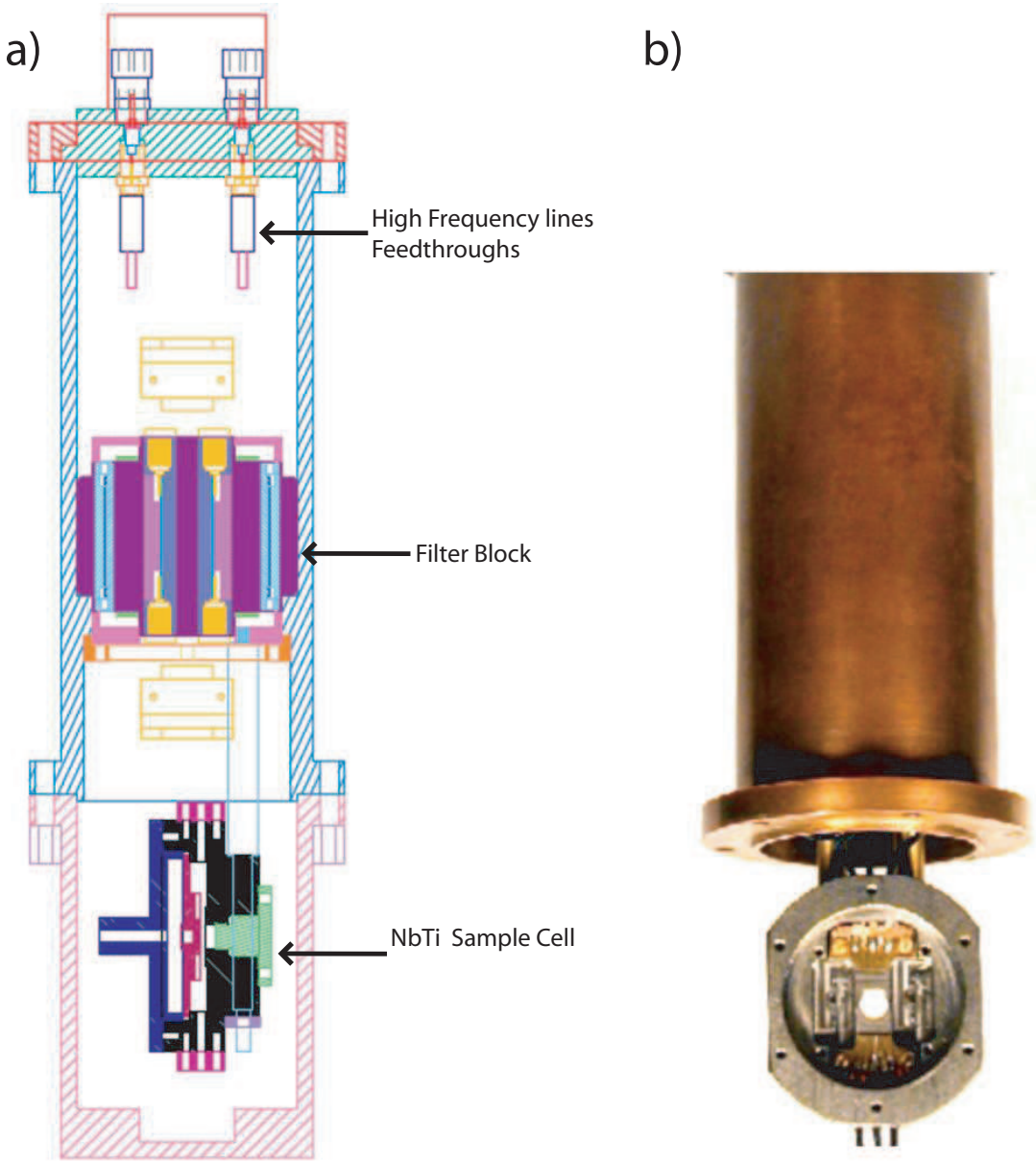

Figure 2.4: a) Drawing of a cross-sectional view of the assembled outer sample can and NbTi sample cell. b) a picture of the sample can with the bottom opened and part of the NbTi cell mounted

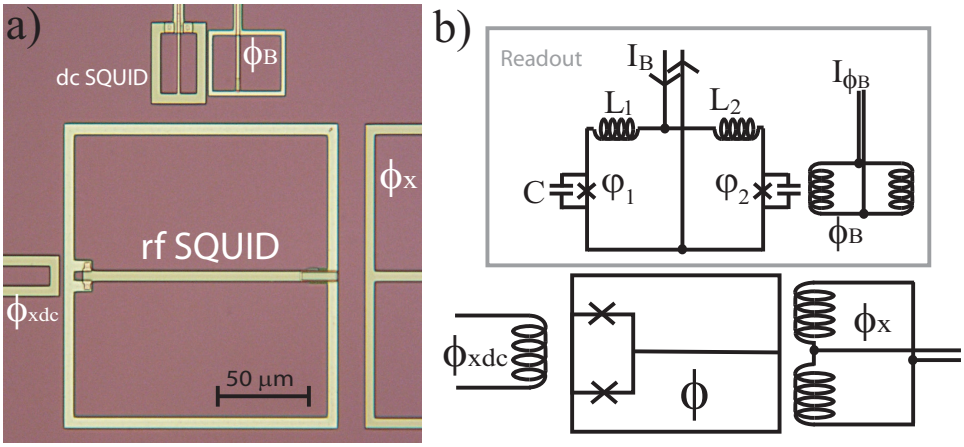

Figure 2.5: a) Photograph and b) schematic of the rf SQUID qubit and the readout dc SQUID magnetometer.

μm. Once aligned the two chips are locked into position using four precision screws and the cell can be assembled. The top lid slides into position down Teflon tubes that protect wiring from any kinking or sharp edges. All the necessary holes are designed so that the radius is more then ten times smaller then the length [31]. This stops flux changes from penetrating into the cell by attenuating the flux changes down to negligible levels.

2.2.3 Qubit Design

The qubit design shown in Fig. 2.5 consists of a rf-SQUID that uses a large gradiometric loop ϕ, of size $150\mu m \times 150\mu m$ with a 5 μm wide trace, in series with a small loop ϕ_{dc}, of size $5\mu m \times 5\mu m$ and containing the Josephson junctions [33]. The size of the junctions varies between samples depending on the desired parameters and it is $1.45\mu m \times 1.45\mu m$ for the majority of the data shown in this work. The current density for these devices was designed to be $J_c \approx 100\ A/cm^2$ and is estimated from measurements of diagnostic devices along with the junctions in the magnetometer. The inductances are calculated using the 3D-MLSI software package [53]. The result of such calculation gives $L \approx 215pH$ for the qubit loop and $\ell \approx 10pH$ for the small loop, and are consistent with the measurements from Chapter 3. The ϕ_x (ϕ_{xdc}) bias coil is shown on the right (left) of Fig. 2.5b. As explained in section 1.3, flux applied to the large loop using the ϕ_x bias coil tilts the potential while flux through the small loop modulates the effective critical current, lowering the barrier. The gradiometric configuration makes the sample insensitive to fluctuations in the background magnetic field and reduces the crosstalk from the ϕ_x bias

coil to the ϕ_{dc} loop. There is a small coupling between ϕ_{xdc} and the ϕ loop but this can be measured and compensated with a feedback circuit.

The source for the ϕ_{xdc} coil is one of the four channels of a Keithley 213. The voltage is sent into an isolation amplifier and then across a bias resistance of 1 $k\Omega$. In some measurements it is also necessary to vary the barrier height for a short time with accurate timing. To accomplish this one of the three channels of a Tektronix arbitrary waveform generator AWG 430 is used. The AWG430 supplies a programmable waveform of up to 16,200,000 points at clock frequency up to 200×10^6 samples per second with 16 bit voltage resolution corresponding to 75 μV steps. The voltages from these two sources are summed using Stanford Research System SIM 980. The signal from the AWG 430 is attenuated using a SIM 983 scaling amplifier in order to use the largest range, hence the most voltage steps of the AWG. Another SIM 983 scaling amplifier is used after the summer to provide an adjustable offset. Synchronization between the two voltage sources is accomplished using a pulse from a different channel of the Keithley while the Keithley is software triggered. The current is measured by recording the voltage through a sensing amplifier across the 250 Ω sense resistor. This voltage can also be used in a feedback circuit to the ϕ_x flux bias to compensate for the crosscoupling between ϕ_{xdc} and the main qubit loop.

The qubit flux bias, ϕ_x, requires the ability to accurately set and step the current while providing fast accurate pulses to measure the escape rate. The setup that allows to accomplish both these tasks is very similar to the one previously described and also uses a combination of signal from the Keithley 213 voltage source and the Tektronix AWG 430. The qubit initialization is programmed into the voltage output of the Keithley 213 since it does not require accurate timing. The composite signal is sent into an isolation amplifier and subsequently into a bias box before being connected to the inputs at the top of the dilution refrigerator.

The qubit flux state is measured using a hysteretic dc SQUID magnetometer shown at the top of Fig. 2.5b. The magnetometer is designed so that its bias current I_B does not couple to the qubit to first order [39] hence fluctuations in I_B do not reach the qubit. The measured mutual inductance between the qubit and the magnetometer is 5 pH, consistent with the design value of 4.3 pH. The junctions of the magnetometer are 2.15 x 2.15 μm and 2.85 x 2.85 μm giving a maximum critical current of $10.8\mu A$. A detailed description of the design and the operation of the magnetometer is given in section 2.2.4. Signals coming from both the ϕ_x and the ϕ_{xdc} coils couple to the magnetometer. These couplings do not affect the measurements presented in this thesis however they can be compensated through a feedback circuit connected to the

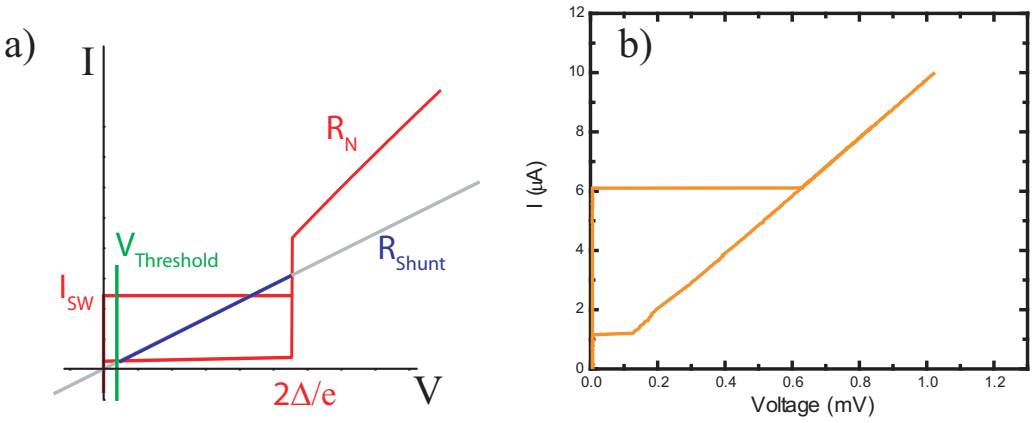

Figure 2.6: a) A schematic representation of a the bias current IV characteristic of a hysteretic dc SQUID magnetometer. The red line is the IV without the shunt resistor while the blue line shows the effect of the shunt resistor. b) a measured IV of the magnetometer with a shunt resistor.

magnetometer's bias coil, ϕ_B, which is designed not to couple to the qubit.

2.2.4 Magnetometer Design

The qubit readout is performed using an on-chip hysteretic dc SQUID magnetometer [54, 55] which, when appropriately biased with current and magnetic flux, can be used for single shot measurement of the flux state of the qubit by measuring the switching current of the magnetometer.

Any readout mechanism of a quantum system should be regarded as part of the external environment and hence a source of decoherence. therefore it is important to implement a low back action measurement of the state of the qubit and to design the coupling between the readout and the qubit to be strong enough to distinguish between the two macroscopic states while not causing significant decoherence of the qubit. A hysteretic dc SQUID magnetometer represents a reasonable compromise between low back action onto the qubit and accurate measurement of the flux state.

A dc SQUID consists of two Josephson junctions in parallel in a superconducting ring with leads to provide current bias. The top box of Fig. 2.5b shows a lumped model of the dc SQUID magnetometer. The junctions are modeled as ideal Josephson currents with phase differences across the junctions φ_1 and φ_2 in parallel with a capacitance C. The junctions are coupled by two ideal inductors L_1 and L_2. The SQUID maximum critical current $2I_{c0}$ is the sum of the critical currents I_{c1} and I_{c2} of the two junctions, while the junction

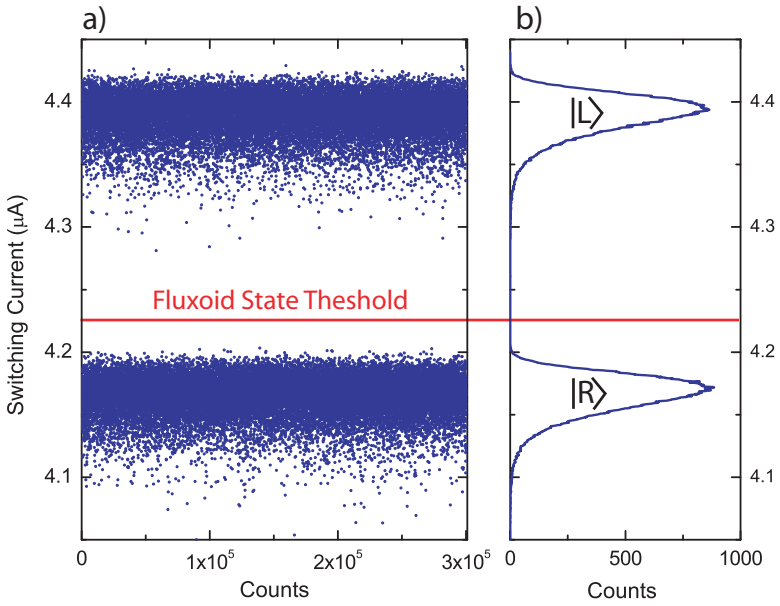

Figure 2.7: a) A switching current measurement at 10mK. b) A histogram of the data showing the separation of the distribution corresponding to the different fluxoid states.

asymmetry is defined as $\delta i = (I_{c1} - I_{c2})/2I_{c0}$.

The magnetometer biasing circuitry is specifically designed to minimize the level of external fluctuations that couples to the qubit. As it can be seen in Fig. 2.5, both the magnetometer and the flux bias loop are gradiometric to minimize direct coupling due to geometric inductances. A small asymmetry in the gradiometric flux bias loop compensates the direct coupling to the qubit by the coupling via the magnetometer. As a result of this design, the residual couplings to the bias leads can be less than 1 fH therefore the only significant coupling of the readout to the qubit is due to the circulating current. This indirect coupling of external biases to the qubit through the circulating current provides a path for external noise to couple to the qubit. By designing an asymmetry in the critical currents of the two Josephson junctions of the magnetometer, the dynamics of the dc SQUID can be manipulated in a way that the derivative of the circulating current vanishes at the required bias current. This effectively decouples, to first order, the qubit from fluctuations in the current bias [39].

A schematic of the IV characteristic for a typical hysteretic dc SQUID is shown in Fig. 2.6. The inset shows an actual measured IV. The difference between the two graphs is due to a shunt resistor inserted in parallel with the magnetometer. The net effect of adding a shunt resistor is that, when ramped

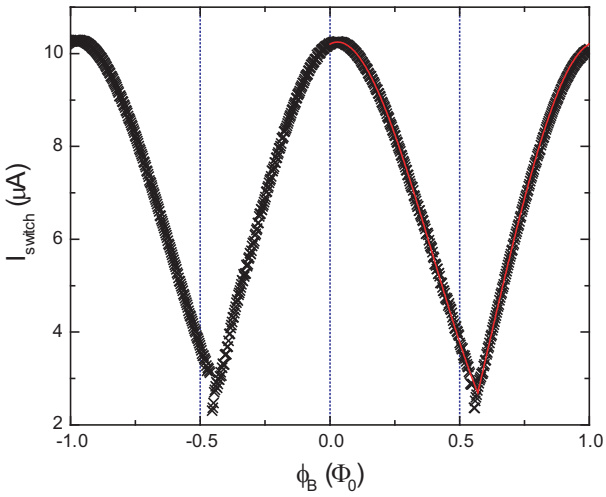

Figure 2.8: The measured switching current of the magnetometer as a function of flux applied from the ϕ_B coil at 10mK. The red line is a theoretical fit of the data.

to a certain switching current I_{sw} the magnetometer does not switch to the superconducting gap but to some finite value determined by the shunt resistance, therefore preventing the magnetometer from creating excess quasiparticles.

A measurement of the switching current of the dc SQUID requires the ability to bias the magnetometer with a linear ramp, reset the magnetometer by going to zero bias and be synchronized with the qubit operations. This is accomplished using an output channel of a Tektronix AWG430. The signal from the AWG goes through an isolation amplifier to a bias box consisting of biasing and monitoring resistors. The voltage across the monitoring resistor is sensed by a Stanford Research Systems SIM 910 JFET amplifier operated in differential mode. The voltage from the sensing amplifier is measured using a fast multimeter (HP 3458A). A threshold detectors measures the moment at which the magnetometer switches to the non-zero voltage state. A digital pulse from the threshold detector triggers the multimeter to measure the switching current. The I_{sw} is then recorded by a computer interfaced to the multimeter via a General Purpose Interface Bus (GPIB) and the measurements is repeated many times so to obtain sufficient statistics to extract the mean and first moment of the distribution. The value of the switching current depends on the fluxoid state the qubit is in. Figure 2.7a shows typical raw data for half a million switches at a ϕ_x value such that the qubit has equal probability of being in either of the potential wells.

The magnetometer's switching current can be modulated by passing cur-

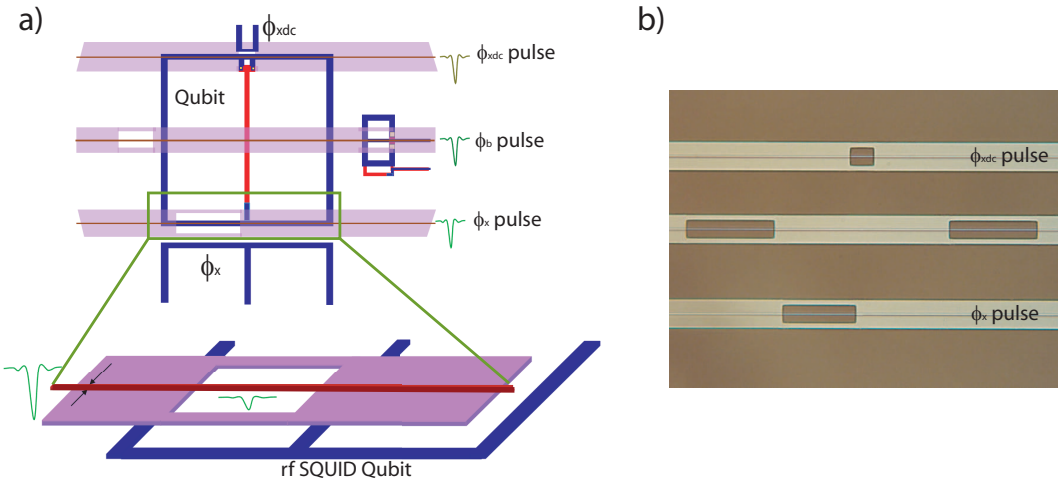

Figure 2.9: a) A drawing of the pulse chip superimposed to the qubit chip and b) a picture of the pulse chip.

rent through the magnetometer's flux bias (ϕ_B). The bias circuit in this case consists of a programmable battery powered isolated voltage source, Stanford Research System SIM 928, and bias resistors. A measurement of switching current of the magnetometer as a function of flux applied from ϕ_B is also known as a transfer function and it is shown in Fig. 2.8. The transfer function has a one flux quantum periodicity therefore this data can be used to convert switching current measurements to flux through the SQUID loop. When the magnetometer is operated in a linear section of the transfer function, the switching current of the magnetometer is proportional to the flux through the magnetometer loop and therefore proportional to the flux change in the qubit.

2.2.5 Pulse Chip

Microwaves and fast flux pulses are coupled to the qubit using high frequency transmission lines housed on a separate chip suspended overtop the qubit chip. A picture and drawing of the pulse chip are shown in Fig. 2.9. As explained in section 2.2.2 the pulse chip and the qubit chip are aligned using precision translation stages while viewing on chip alignment marks and verniers under a microscope. The signals are transmitted from room temperature to the cell using semi-rigid coaxial cables. The cables are soldered to a PC board and then connected to the chip using three wire bonds at each connection to minimize impedance mismatch. The coupling of fast flux pulses and microwave pulses is localized to a specific region of the qubit through a hole in the ground plane of superconducting microstrip transmission lines. The

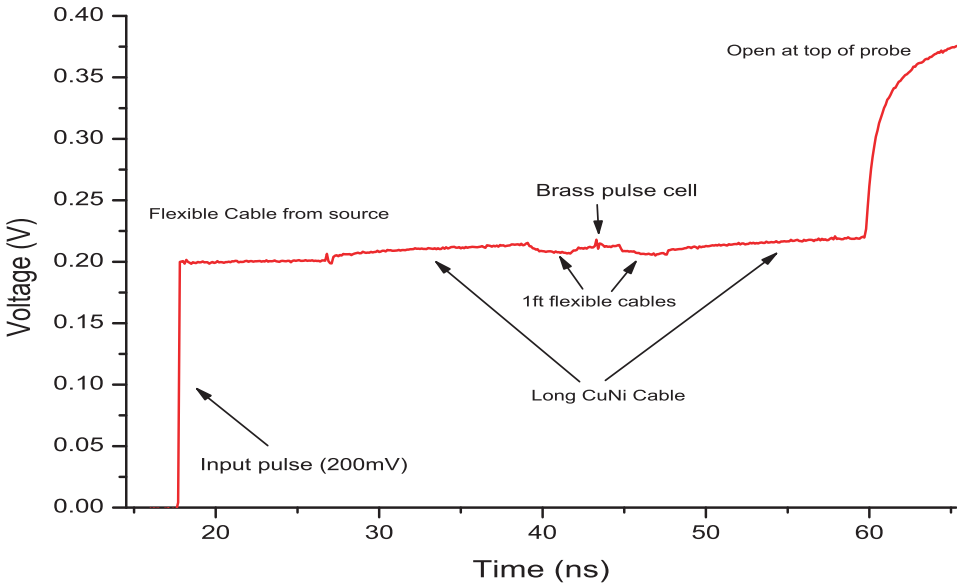

Figure 2.10: Time Domain Reflectometry measurement of the pulse chip mounted in sample cell. The sample cell is mounted in a dip probe immersed in liquid He at 4.2 K

mutual inductances between the various transmission lines and the qubit chip measured at 1.2 K using measurements of the qubit magnetic flux as function of DC signal in the transmission lines, as it will be explained in chapter 4. Other 1.2K tests of the pulse chip included measurements of the transmitted microwave power through the pulse chip as a function of frequency up to 20 GHz and time domain reflectometry shown in Fig. 2.10. One advantage of realizing the high frequency lines on a separate chip is that these lines have to be carefully characterized just once, allowing for using the same pulse chip with different qubit chips thus reducing the experimental setup time.

For the experiments described in this thesis the pulse chip is used to couple microwave signals and fast flux pulses to the qubit's large gradiometric loop and to the small loop. The flux pulses are produced by a Tektronix Data Timing Generator (DTG 5274) which can produce very short pulses with rise times as short as 200 ps and voltages as large as 2.7 V. The DTG is also used to create microwave pulses in combination with a HP Synthesized Signal Generator 83731B. The microwave signal is generated by the HP 83731B, while the DTG 5274 is used to produce the pulse envelope. The two signals are combined using a double balanced mixers setup [56] as shown in Fig. 2.11. The two mixers configuration increases the ratio of the "off" to "on" state of the mixer. The microwave pulses are observed at room temperature using a

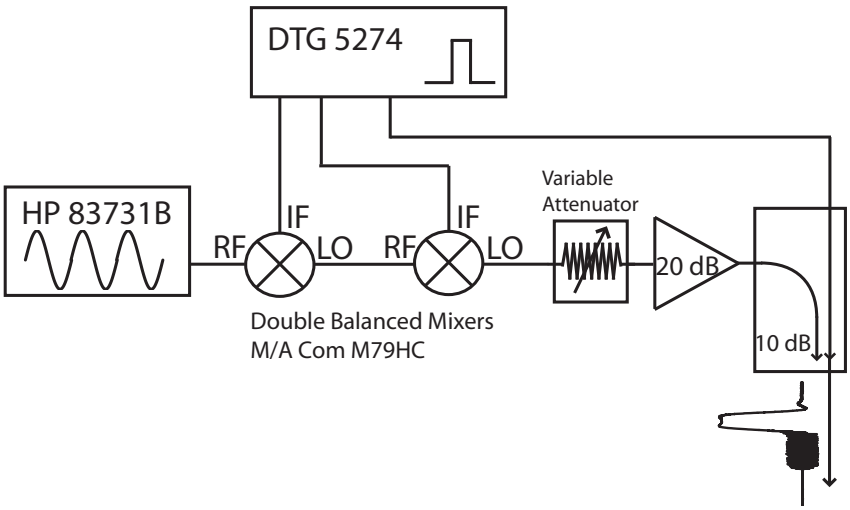

Figure 2.11: Schematic of the microwave components used to create the microwave pulses and combine them with the fast flux pulses.

Agilent Infinium DCA-J 86100C sampling scope. This setup allows to optimize the delay between the pulse sent to the second mixer with respect to the pulse sent to the first mixer, and to adjust the voltage of the envelope pulses until the cleanest microwave signal is achieved.

In some of the measurements, flux pulses and microwaves need to be used on the same bias line at the same time. A directional coupler, Agilent 8730C, is used to combine the microwave pulses with the fast flux pulses. The fast flux pulses are input through the directly coupled port, known as the output port. The microwaves are coupled through the -10 dB indirectly coupled port. This port only couples to the other ports when the signal is between 1 and 26 GHz. The directivity of the coupler allows the signals to be combined without reflections distorting the pulses. The combined signal is output through the final port, usual called the input port.

2.3 Niobium Circuits Fabrication

2.3.1 Qubit Fabrication

The rf SQUID qubit realized at Stony Brook University is based on Josephson junctions fabricated using $Nb/AlO_x/Nb$ trilayer technologies capable of producing large-scale superconducting circuit applications [57, 58].

The trilayer process developed for the samples presented in this thesis [59, 60] is designed to minimize the number of fabrication steps shortening the

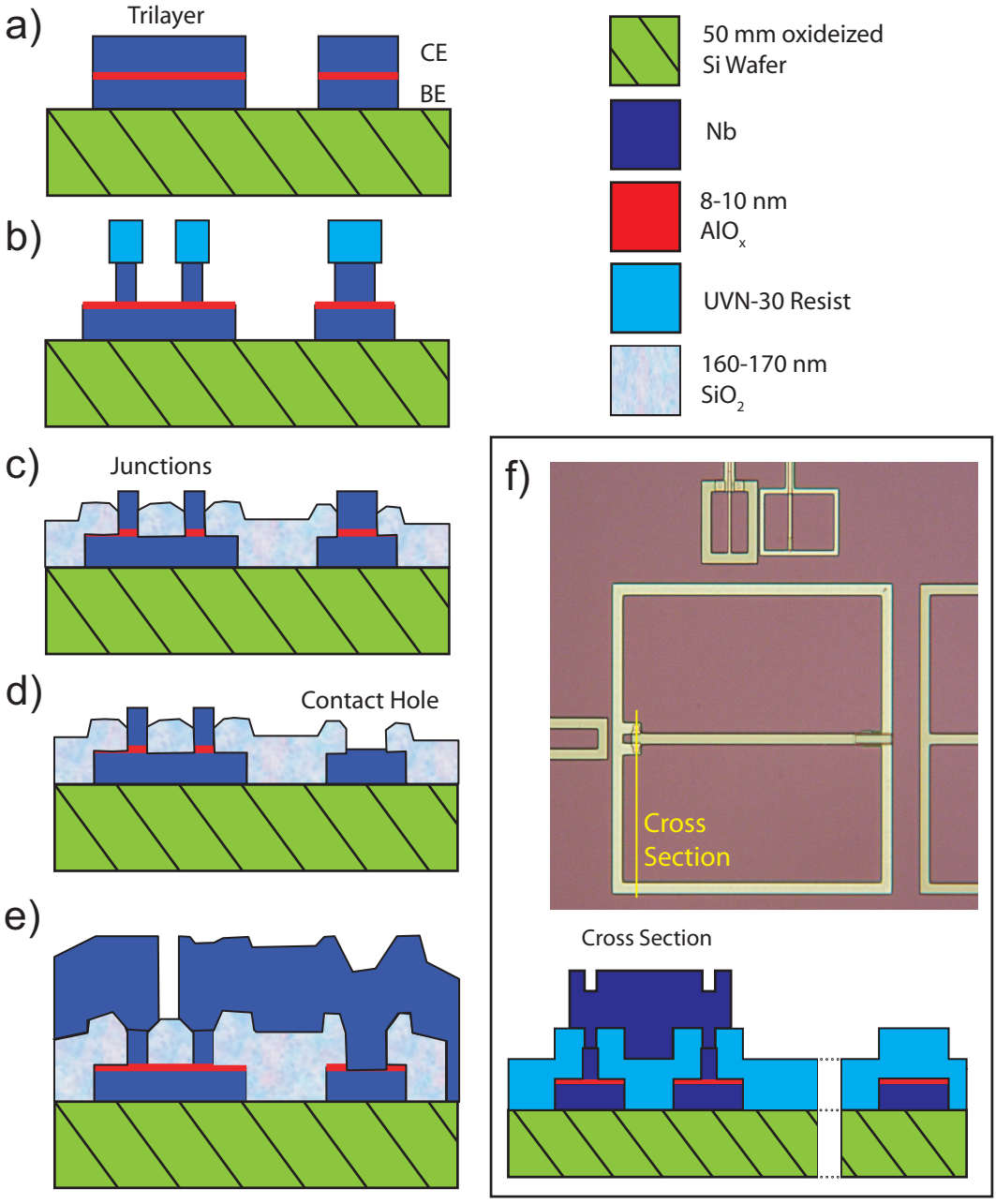

Figure 2.12: Process flow for the SAL-EBL fabrication shown at various stages a) after trilayer liftoff, b) after RIE of the counter electrode, c) after deposition of SiO_2 and stripping of resist, d) after RIE and wet etch to define contact holes e) after liftoff of wiring layer and f) a photograph and cross section of the qubit.

turn around time and simplifying characterization of qubit performaces due to the process and the materials. The process is based on self-aligned lift-off (SAL) of the dielectric and uses both UV and electron beam lithography (EBL) which allows for junction sizes as small as 0.15 μm x 0.15 μm.

The photolithographic masks specifically designed for the realization of the qubit and pulse chips are used to define the large electronic structures via UV lithography and also to provide alignment marks as reference for electron beam lithography (EBL). The parts of the design realized by UV lithography comprise the electronic connection to the qubit, the magnetometer and their bias and control lines. These latter components are patterned using the EBL part of the process, allowing for a great flexibility in the design, since the same set of masks can be used to implement devices with different circuit parameters. The SAL process is outlined in Fig. 2.12. The first step consists of patterning of the $Nb/AlO_x/Nb$ trilayer. This is achieved using a lift-off technique to minimize the number of reactive ion etches (RIE) of Nb. The substrate, a 50 mm oxidized Si wafer, is coated with a PMMA/P(MMA/MAA) bilayer resist. The resist is then patterned by a combination of UV and electron beam lithography.

The trilayer is deposited at base pressures around 1×10^{-7} Torr in a cryopumped vacuum system. The Nb base (BE) and counter electrode (CE) are both 150 nm thick and deposited using DC magnetron sputtering. The 8-10 nm thick Al interlayer is also sputtered using a DC and the oxide barrier is formed by thermal oxidation using dry O_2 at $10^3 - 10^4$ Torr-min which gives current densities (J_c) of 50-150 A/cm^2. After the trilayer lift-off, the CE is patterned by EBL using a UVN-30 resist with resist resolution better than 100 nm. The junctions are then defined by RIE in SF_6 plasma. The etch endpoint is detected by monitoring the Fluorine optical emission spectra during the RIE. The RIE is followed by the deposition of a 160-170 nm SiO_2 dielectric using a RF sputtering system. The UVN-30 resist is then stripped exposing the Nb CE. The contact holes are also formed by a SF_6 RIE of the CE with the oxide barrier removed by an Al wet etch. The last step of the process consists of the formation by lift-off of a 250 nm thick Nb wiring layer.

2.3.2 Pulse Chip Fabrication

The pulse chip shown in Fig. 2.13a is fabricated on 2" fused quartz wafers also using a combination of deep-UV and electron beam lithography. The coplanar waveguides and microstrip lines are formed by dc-sputtering 200 nm Nb films and are designed to have a 50Ω impendence [61].

Figure 2.13b shows a cross section of the chips. After the Nb deposition a 350 nm thick SiO_2 film is deposited in a RF sputtering system. Contact vias

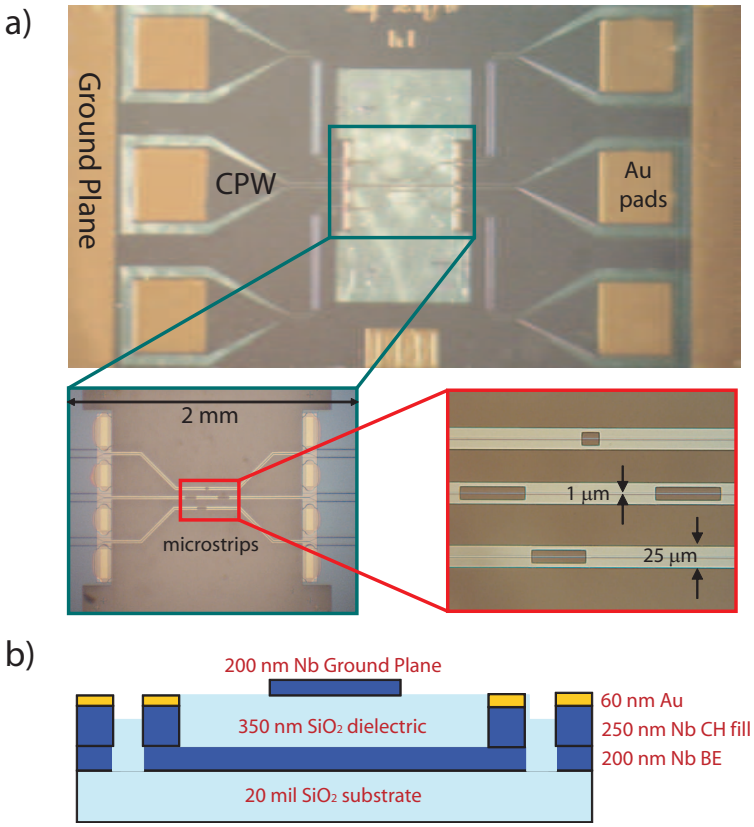

Figure 2.13: a) Pictures of the pulse chip and b) a cross section of the fabrication process.

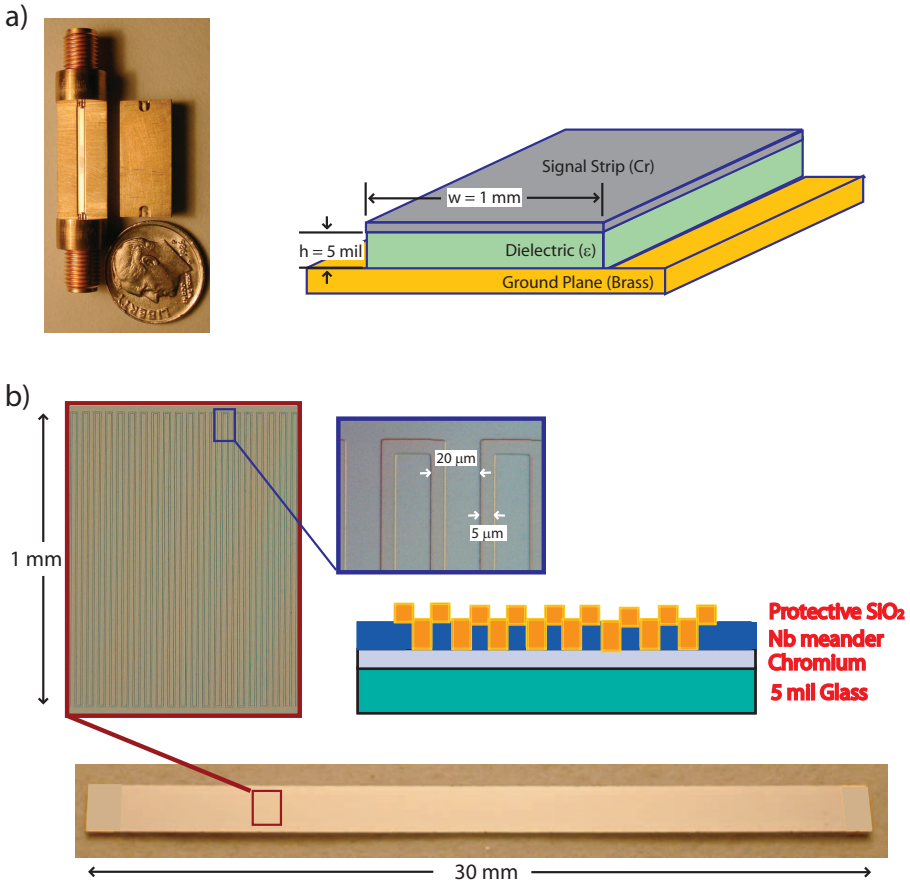

Figure 2.14: Pictures and cross section of the lossy microstrip filter a) without and b) with the Nb meander line.

are then etched and subsequently filled with 250 nm of Nb. The next step is the formation of the microstrip ground planes by the deposition of a 200 nm Nb film. Finally the contact pads are realized using 60 nm of evaporated gold. The pulse chip design most commonly used for the experiments presented in this thesis has a 1 μm wide signal conductor of the microstrip while the ground plane is 25 μm wide.

2.3.3 Microstrip Filters Fabrication

A cross section of the microstrip filters is shown in Fig. 2.14. The fabrication process is rather straightforward. The chromium is evaporated on 5 mil glass or sapphire wafers. The chromium thickness can be varied to change the resistance per square of the film depending on the desired filter parame-

ters. The Nb meander is patterned using electron beam lithography and then etched using the standard process previously described (section 2.3.1) [60]. The meander line has a thickness of 5 μm and a pitch of 20 μm to obtain an inductance of approximately 1.3 μH. A 250 nm layer of SiO_2 is deposited on top of the niobium to protect it from scratching and breaking. The filters are diced to the necessary length and width to reach the desired response and glued to the housings using GE varnish.

Chapter 3

Experimental Results and Data Analysis

3.1 Introduction

The magnetic flux of a rf SQUID acts as a macroscopic quantum variable whose dynamics are described by a double well potential. When studying quantum transitions of this macroscopic variable, two major categories of phenomena can be identified: interwell and intrawell transitions.

The latter includes a large variety of effects involving energy levels within the same potential well. In this work we report measurements of phenomena involving only the two lowest energy levels within a single potential well, including a direct measurement of the lifetime of the first excited state, energy level spectroscopy and Rabi Oscillation. All these measurement are made possible through the application of microwave pulses that allow to achieve a significant population of the first excited energy level even at the base temperature of a dilution refrigerator (10 mK).

Under the category of interwell phenomena are included measurements of incoherent transitions between levels in opposite potential wells. In this chapter we report measurements of macroscopic resonant tunneling (MRT) when energy levels in each well are aligned, and photon assisted tunneling (PAT) obtained when photon pumping population to a higher level within a well. We also report measurements of thermal equilibrium transitions obtained while changing the potential barrier height at a fixed tilt.

Theoretical models for all the various phenomena are also presented in this chapter. These models provide good qualitative agreement with the data and in some cases allow for an estimate of the type and level of intrinsic flux noise that affects the decoherence of our qubit. In particular we analyze the pos-

sibility of using the MRT as a tool for future studies of effects of materials and fabrication process in the realization of improved qubits, and we suggest possible design changes to allow implementing measurements of quantum phenomena that involve fast pulsing of the ϕ_{xdc} bias line (and therefore of the potential barrier height).

3.2 Macroscopic Resonant Tunneling

The observation of resonances in the tunneling rate of the flux between two distinct wells of the qubit potential, when the ground state of the upper well is aligned with an excited state of the lower well, is referred to as Macroscopic Resonant Tunneling (MRT) [33]. For a particular condition of potential tilt and barrier height the ground state in the upper well is effectively a metastable state, whose lifetime depends on the size of the tunneling barrier, and could in principle be much longer than any time scale of the experiments presented in this thesis.

3.2.1 Measuring the Escape Rate

The rate of escape from the metastable state can be measured by pulsing the flux to the value of ϕ_x at which the tunneling escape rate is going to be measured and leaving it there for a time t_m, chosen to allow for a reasonable probability of tunneling. In the experiments presented here the system tunnels into an excited state of the lower well, and the experiment is performed in an incoherent regime in which the relaxation rate within a same well is much faster than the tunneling rate, therefore after tunneling the system is trapped in the new flux state.

Figure 3.1a shows the waveforms involved in the measurement process along with a cartoon representing the potential at that point. Figure 3.1b shows a measurement of a typical probability of transition and its conversion to escape rate. The measurement starts with the potential near symmetry with a sufficiently high barrier to ensure that the tunneling probability is negligible and the flux state is frozen in either of the potential wells. An initialization pulse is then applied to tilt the potential and set the qubit in a predetermined flux state. The potential is then tilted in a direction opposite to the one set by the initialization pulse, to a configuration such that there is now a finite probability of tunneling through the barrier. This system configuration is then maintained for a fixed, predetermined time t_m before being tilted back to symmetry. The barrier height is now again such that the system is trapped in one of the fluxoid states and it can be read-out by ramping the bias current of the

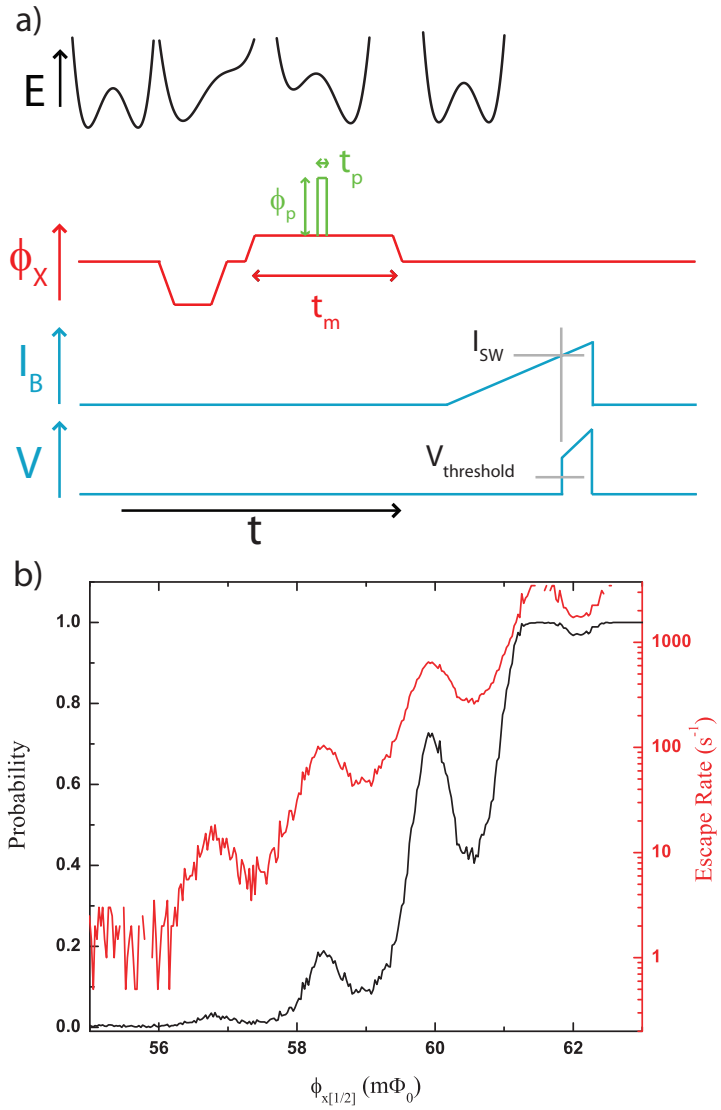

Figure 3.1: a) Outline of the measurement signal sequence, including also a fast ϕ_x pulse from the high frequency line. The fluxoid state is determined by measuring the value of bias current (I_B) at which the magnetometer switches to the voltage state. b)A typical measurement of the transition probability as a function of the applied ϕ_x (black), along with its conversion to escape rate (red) obtained using equation (3.1)

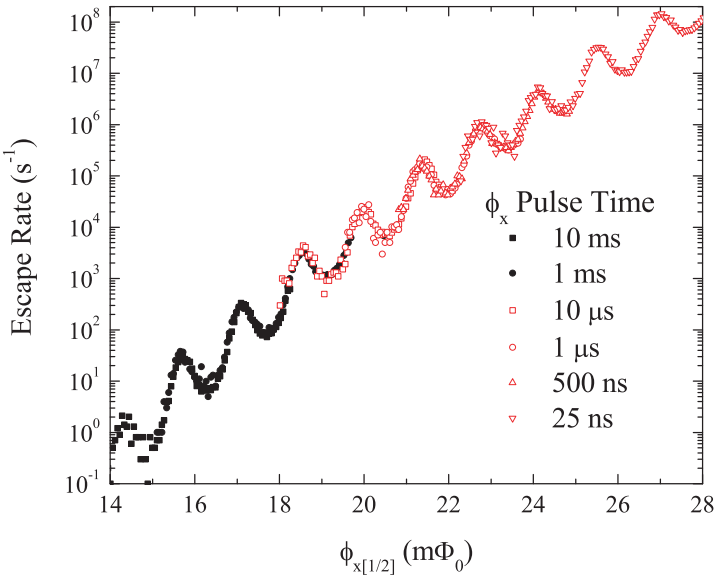

Figure 3.2: Measured escape rate as a function of qubit flux bias obtained, for different lengths of the flux pulses, with a flux pulse from the high frequency transmission line (red open symbols) or from the on chip bias coil (black filled symbols).

magnetometer. This procedure is then repeated a few thousand times, until enough statistics is achieved to determined the probability of tunneling. As it was shown in Fig. 2.7, the magnetometer switching current distributions corresponding to the different fluxoid states are well separated and easy to identify. In order to extract a probability from a measurement of switching current, all that is needed is to set a threshold between the switching distributions and take the ratio between the counts on either side of the threshold (depending on which one is the flux state of interest) and the total number of counts. A complete measurement also involves stepping the value of ϕ_x across the transition region.

The escape rate Γ_{escape} is determined from the probability of a transition, $P(\phi_x)$, for a given t_m, as a function of the tilt of the potential by

$$\Gamma_{escape}(\phi_x) = \frac{1}{t_m} \ln\left(\frac{1}{1 - P(\phi_x)}\right) \tag{3.1}$$

The low frequency ϕ_x bias line can support pulses with a width as small as 0.5 ms, which limits the maximum detectable escape rate to about $10^4 s^{-1}$, however it is still possible to couple faster ϕ_x pulses using the high frequency line located on the pulse chip. In the experiment the two lines are generally

used together since the low frequency voltage source (Tektronix AWG430) has the capability to create signals with finer voltage steps than the pulse generator. The result of adding signals from the two sources is displayed in Fig. 3.2 which shows typical data for the escape rate as a function of ϕ_x using pulses with a width ranging from 25 ns to 10 ms for a $\beta_L = 1.4$. The black filled points are measured just using the Tektronix AWG430 to bias the on chip ϕ_x coil while the red open points are obtained using a combination of both high and low frequency sources.

It is also worth noting that by varying the amplitude of the fast pulses the ϕ_x signal from the two sources can be calibrated with respect to each other.

3.2.2 Extracting Flux Noise from the MRT Data

The measurement of escape rates represents the most important basic tool not only for the experimental observation of Macroscopic Resonant Tunneling, but also for detecting more complex intrawell quantum phenomena, such has measurement of the decay time from an excited state, intrawell spectroscopy, and Rabi oscillations, that will be reported in section 3.3. These measurements have proven themselves a really valuable tool to determine the level of flux noise that couples to the qubit limiting its coherence time [39, 40]. It should be noted, however, that it is also possible to fit the amplitude and shape of the MRT peaks to obtain an estimate of the amount of flux noise coupled to the qubit. The basic theory for this fit has been developed by Averin et al. [62]:

$$\Gamma_{esc} = \frac{\Delta^2(\phi_x)\Gamma_n}{2\Delta^2(\phi_x) + \Gamma_n^2 + 4(\omega_2/\pi \cdot sin(\varepsilon\pi/\omega_2))^2} \tag{3.2}$$

Under the assumption that the flux noise that couples to the qubit can be considered static when compared to the relaxation rate, equation (3.2) can be modified to account for this noise by a simple convolution with a gaussian broadening.

This gives the measurement of resonant tunneling peaks great diagnostic value since their measurement does not require the use of microwave signals, it is a much easier experiment than the measurement of any of the intrawell phenomena, and it can be used as a basic tool to compare the properties of qubits fabricated in different run to test the effect of substrate, materials and fabrication process.

The escape rates as a function of ϕ_x shown in Fig. 3.3 have been measured at a $\beta_L = 1.4$. As previously explained, this is an incoherent phenomena due to the short lifetime of the excited state in the lower well compared to the frequency of oscillation between coupled states in different wells. The solid

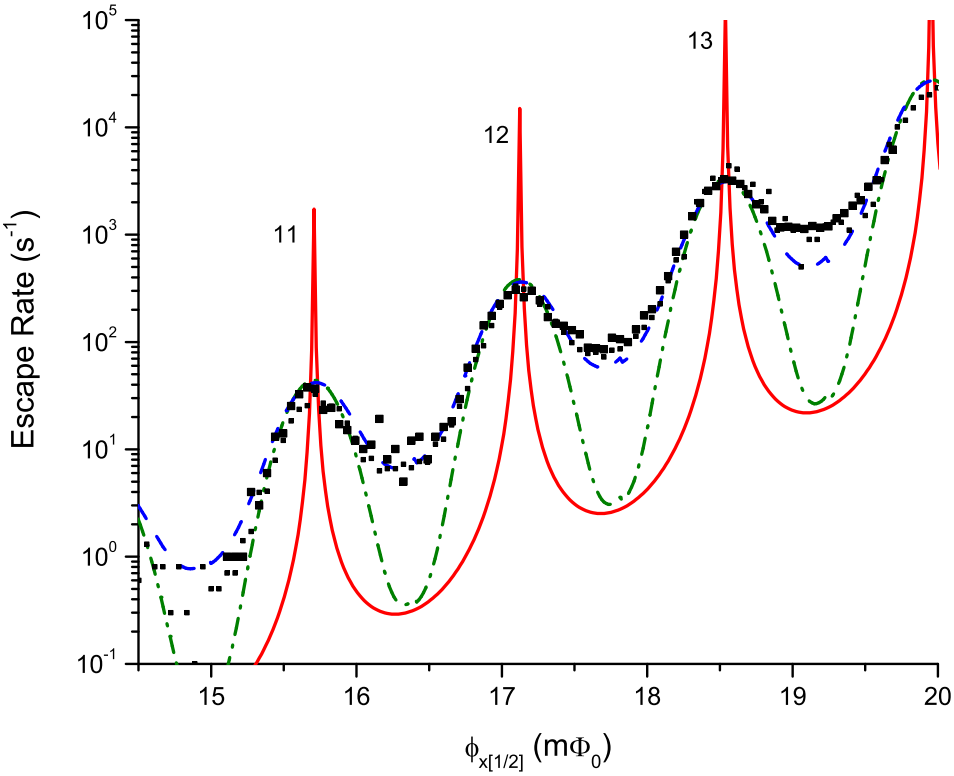

Figure 3.3: Measured escape rates from the ground state in the left well as a function of ϕ_x at a $\beta = 1.412$, the resonant tunneling peaks are labeled with an index which indicate which level in the right well is aligned with the ground state in the left well. The solid red line is a calculation for $\Gamma_{12} = 6.8 \times 10^8 s^{-1}$. The green dash dot line corresponds to the solid line with the addition of static Gaussian noise with $\sigma = .23 \times 10^9 s^{-1}$. The blue dashed line has the same level of Gaussian noise but with $\Gamma_{12} = 1.05 \times 10^{10} s^{-1}$.

line is a calculation of the escape rate using the qubit parameters determined in Chapter 4 and equation (3.2) for the line shape of the resonant tunneling peaks.

As a first approximation the only extra parameter used in the fit was the decay rate, $\Gamma_{12} = 6.8 \times 10^8 s^{-1}$ obtained as the product of the a directly measured rate (see section 3.3.1) and the level number ($n = 12$) [63]. The result of the calculation does not reproduce the data, resulting in much narrower peaks with respect to the measured ones. By convoluting these same peaks with Gaussian flux noise with an rms value ($0.14\ m\Phi_0$) corresponding to the level of detuning noise that will be used to fit the spectroscopy in section 3.3.2. These parameters fit the peaks of the resonant tunneling peak, but do not reproduce the valleys between them. In order to make both the peaks and valleys fit, the relaxation rate must be increased to $\Gamma_{12} = 1.05 \times 10^{10} s^{-1}$. It is still unclear why the combination of low frequency flux noise and relaxation rate used to fit the data involving intrawell dynamics does not fit the valleys between the macroscopic resonant tunneling peaks. It could be the result of a noise source not included in the analysis, a different scaling of relaxation rates to higher levels or related to an incomplete knowledge of the tunneling process.

3.2.3 Using MRT to Diagnose Fabrication Process and Materials

Various sources of decoherence have been predicted to affect the performance of a superconductive qubit both due to external noise and to the local on chip environment. Several tests have been carried to rule out the various sources of decoherence in the qubits presented in this thesis. Careful studies by Patel et al. [60] and Pottorf et al. [64] on Josephson junctions cofabricated with the qubit samples have shown excellent junction quality, based on measured subgap resistance, and ruled out low frequency critical current fluctuations as the main contributor of decoherence in our qubit.

As explained in the previous section the shape of the MRT peaks can be linked to the intrinsic qubit flux noise, and therefore a measurement of resonant tunneling can be used as a diagnostic tool in the studies of sources of decoherence. As a matter of fact MRT measurements have been used to rule out detrimental effects due to noise originated by the room temperature electronics, or the effect of external noise in the ϕ_x bias coil [65], or due to the back action from the magnetometer [39]. However the MRT peaks have really proven themselves as a useful tool when comparing qubits realized in different fabrication runs to compare the level of flux noise due to substrates, materials

and photoresists. These type of studies have been recently reinforced by the measurement of spectroscopic data showing that a dominant source of decoherence in superconducting qubits are microscopic two-level system (TLS) defects [28] in the amorphous materials that are used for the physical realization of the qubit circuit [29, 66]. These defects can be linked to intrinsic low frequency noise [26, 67, 68] and ultimately affect the coherence times. For instance, the SiO_2 layer between the junction layer and wiring layer has been considered a potential source of the observed decoherence. Most of the superconducting qubits with longer decoherence times are realized using $Al/AlO_x/Al$ junctions [69, 70] using a two angle shadow evaporation process that has a thin layer of AlO_x for insulation. A group at NIST Boulder use a process for Al junctions that includes a deposited insulation layer. They experimented with different insulating material and they observed a significant increase in the decay time for their Rabi oscillations when they switched from SiO_2 to SiN_x [29].

These results suggested that the most likely candidates to host TLS in our qubits could be the substrate and/or the insulation under the wiring layer. To test these hypothesis various qubit chips have been realized on different substrates, with the superconductive loop in different electrodes and using two kind of photoresists for the patterning. MRT measurements of these devices are shown in Fig. 3.4.

It is also worth reporting that in an effort toward understanding the effects of the insulating layer on the decoherence, qubit samples have been realized with a modified process that did not require depositing the majority of the SiO_2 in the proximity of the qubit's superconductive loop. A photograph of one particular sample is shown in Fig. 3.5a). Unfortunately other unknown problems arose while fabricating these samples yielding to a $\beta_L < 1$ for all the qubits contained on the wafer, making it impossible to perform MRT measurements.

The data in Fig. 3.4 show very little difference in the results obtained for qubits fabricated using different photoresists, or changing the loop electrode, meanwhile a big difference is detected when changing the substrate.
From Fig. 3.5b it is easy to see that the major difference between qubits with the superconductive loop in the base electrode or wiring layer resides on the fact that the base electrode is in direct contact with the substrate and it is always topped by a layer of AlO_x meanwhile for the counter electrode there is no excess AlO_x, however the superconductive layer is deposited on top of sputtered SiO_2 dielectric. If the AlO_x was responsible for hosting excess TLS, the MRT peaks measured on qubits with the loop in the base electrode should have been broader than the analog result for qubits with the loop in the counter electrode, due to a higher noise level.

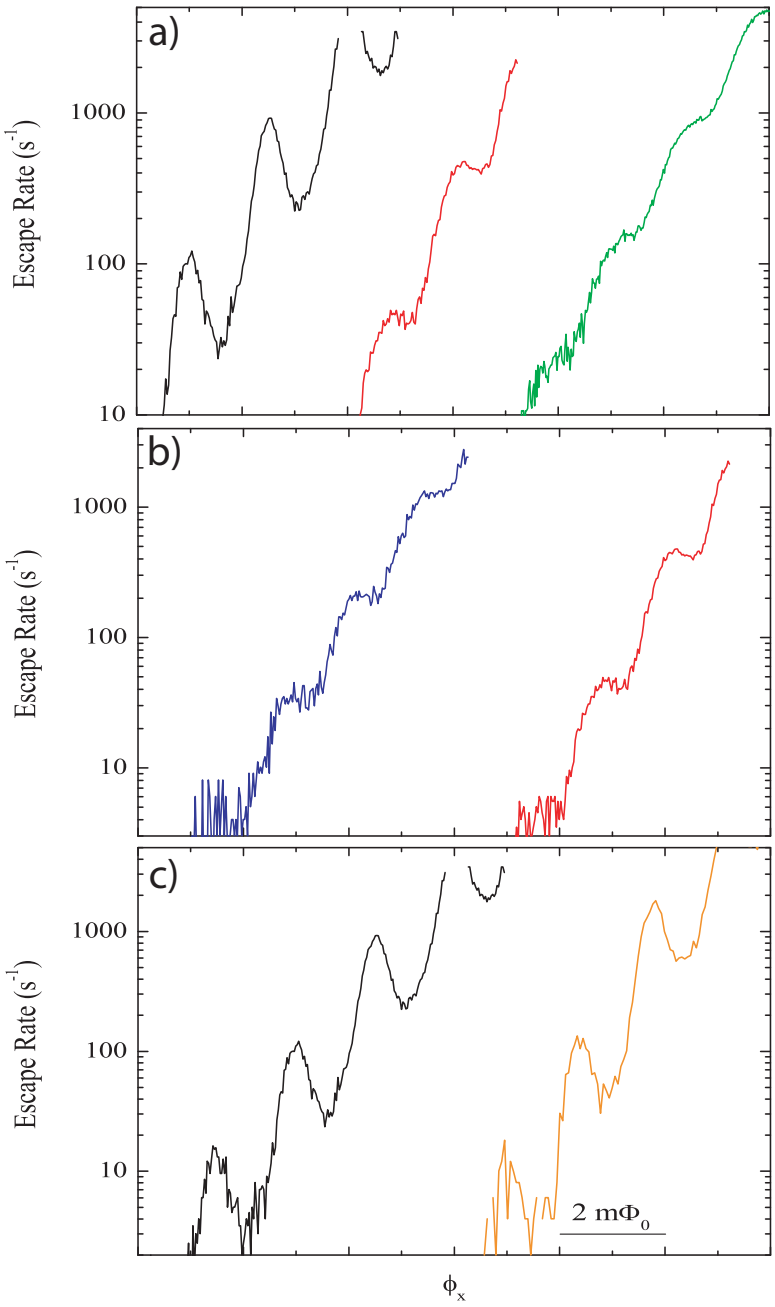

Figure 3.4: Measured escape rates as a function of ϕ_x for different qubit chips. A comparison between: a) different substrates: the qubit had been patterned with the same photoresist and the qubit superconductive loop was fabricated in the base electrode; b) two different photoresists for Nb lift-off, the qubits were fabricated on the same type of substrate and the superconductive loop was patterned in the base electrode; c) qubits with superconductive loops fabricated in the base electrode and in the wiring layer, the substrate and photoresist was the same among the samples. The color code for these data is reported in table 3.1

Table 3.1: Color code for the data shown in Fig. 3.4

Color	Substrate	Photoresist	Superconductive loop layer
Black	20 Ωcm silicon	PMMA	Base Electrode
Red	15 $K\Omega cm$ silicon	PMMA	Base Electrode
Green	Sapphire	PMMA	Base Electrode
Blue	15 $K\Omega cm$ silicon	ZEP	Base Electrode
Orange	20 Ωcm silicon	PMMA	Wiring Layer

It should be noted that the data presented in Fig. 3.4 correspond each to just a single fabrication run and are therefore not statistically relevant. The effect observed when changing the device substrate may be due to the substrate itself, or might be due to non-reproducible lab conditions peculiar of the particular fabrication run, or, as suggested by recent studies from Gao et al. [71, 72], it could be caused by some unforeseen surface effect at the interface between materials.

Gao and colleagues have performed various experiments with superconductive microwave resonators to confirm the TLS hypothesis and to investigate the most likely location for the two level fluctuators. In a first experiment, they deposited 1 micron thick silicon nitride on the surface of Al on sapphire coplanar waveguides (CPW) resonators and found that the temperature dependence of resonance frequency and quality factor agrees well with the TLS theory. They also observed an increase by a factor of 20 in the frequency noise after the deposition of silicon nitride, which constitutes a demonstration that a surface layer of TLS loaded material is able to produce excess low frequency noise. In a second experiment, they measured the temperature-dependent frequency shift of five Nb on sapphire CPW resonators, with center strip widths w ranging from 3 micron to 50 micron. It was again found that the frequency shift can be well explained with the TLS theory. The amplitude of the frequency shift displayed a strong geometry dependence scaling roughly as $1/w^{1.6}$, where w is the width of the superconductive microstrip. This result seems to imply that the TLS are not distributed in the bulk substrate but on the surface of the CPW.

3.2.4 Temperature Dependence of MRT

Another diagnostic strength of the MRT measurement is that the peaks are still detectable at temperatures well above the crossover temperature (T_x - which is about 125mK for the sample mostly discussed in this thesis) be-

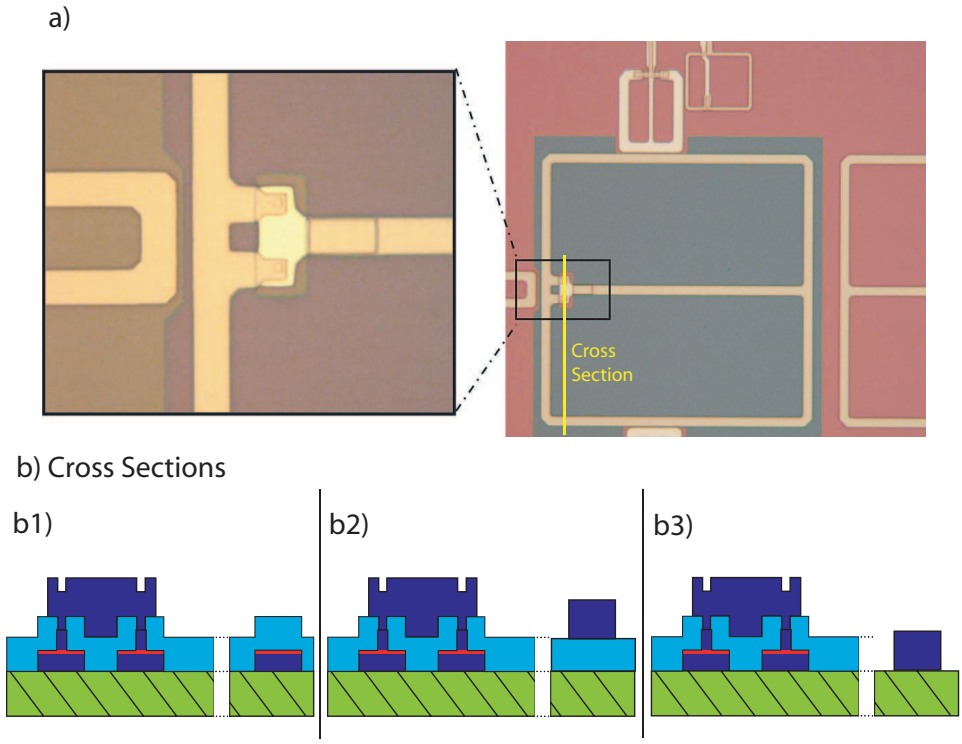

Figure 3.5: a) A photograph of a qubit sample without most of the SiO_2 insulating layer in the proximity of the superconductive loop. The region without the dielectric displays a color tone closer to blue, while the regions with the SiO_2 are closer to red. A magnification of the small dc SQUID loop shows that the dielectric had only been deposited around the Josephson junctions to avoid the creation of electrical shorts between the base and the counter electrode. b) Cross sections of qubits realized with 3 different processes. Cross section b1) shows a qubit with the superconductive loop in the Base Electrode, for cross section b2) the loop is in the wiring layer, b3) corresponds to the cross section for the picture a). The loop is in the wiring layer but there is no SiO_2 dielectric, therefore the loop is in direct contact with the substrate.

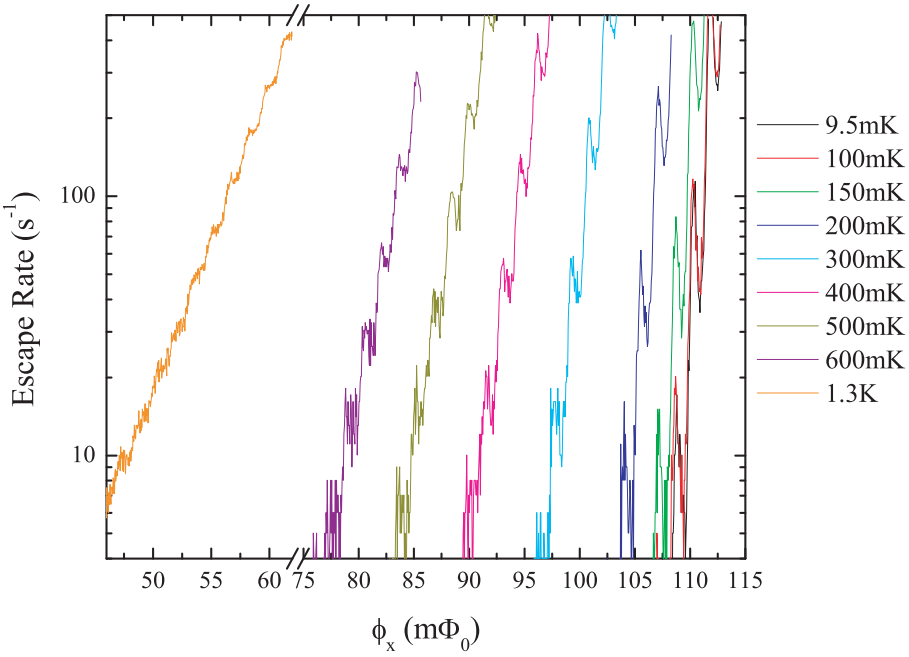

Figure 3.6: Measurements of Macroscopic Resonant Tunneling peaks as a function of temperature. The data corresponding to temperatures from 9.5mk up to 600mK have been collected in a single dilution refrigerator run. The data at 400mK, 500mK and 600mK have been confirmed using the same sample cell and electronics in a He3 Cryostat run. In the same run the data at 1.3K have also been collected

tween the quantum and the thermal regime. This is an advantageous property since it allows us to perform the measurement in a He3 cryostat instead of a dilution refrigerator. A He3 cryostat has a higher base temperature (about 400mK for the thermal load provided by the sample cell used in this experiment) than a dilution refrigerator, however it has the advantage of requiring considerably fewer operational resources and of being easier to use, leading to a shorter experimental turn around time and allowing for faster testing of different samples.

A temperature dependence of the MRT has been measured in the dilution refrigerator up to 600mK. These data, for the same sample, have been confirmed in the He3 cryostat in the temperature interval between 400 to 600mK, and the measurement was further extended to include a data point at 1.3K. The results of these two measurements are reported in Fig. 3.6. Even at the highest experimental temperature the MRT are still clearly detectable. It should be noted that the width of the magnetometer switching distributions broaden as the temperature increases and, at temperatures above 600mK, the

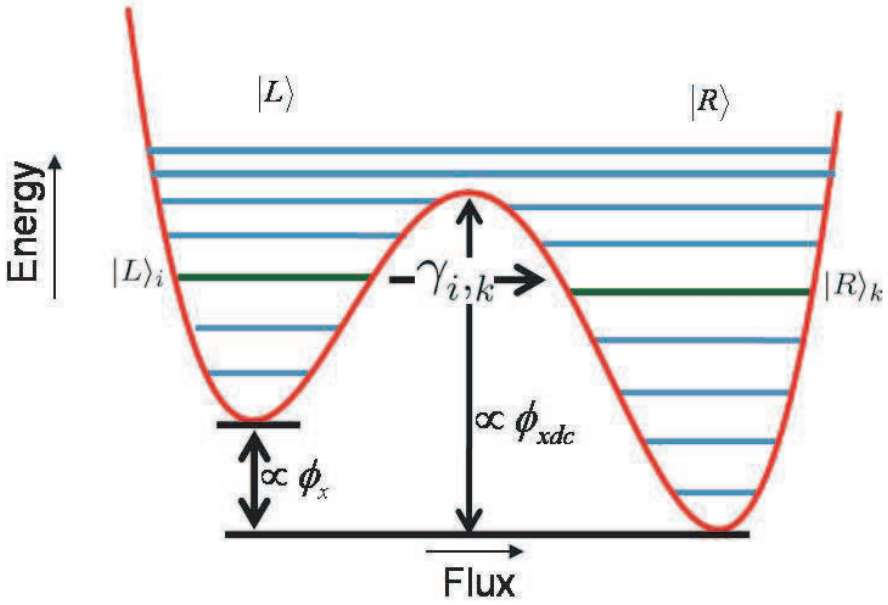

Figure 3.7: A cartoon of the qubit potential and its energy levels. The left and right fluxoid states have been labeled using the kets $|L\rangle$ and $|R\rangle$. Energy levels in the different fluxoid states are identified by mean of the suffix $|L\rangle_i$ for levels in the left well and $|R\rangle_k$ for levels in the right well. $\gamma_{i,k}$ represents the transition probability from the i-th level in the left well to the k-th level in the right well.

distributions corresponding to the two fluxoid states begin to partially overlap. Therefore the method for measuring the escape rate described in section 3.2.1 cannot be reliably used above 600mK. For the higher temperature data a deconvolution algorithm, that allows to clearly distinguish between the two fluxoid states, has been implemented and tested [73].

In order to theoretically discuss Macroscopic Resonant Tunneling at temperatures higher than T_x it is useful to refer to the quantum picture reported in Fig. 3.7. In this figure $\gamma_{i,k}$ refers to the transition probability from the i-th level in the upper well to the k-th level in the lower well.

The tunnel probabilities from one well to the other, as calculated by Kopietz and Chakravarty [74], can be expressed according to the following equation:

$$\gamma_{i,k} = \frac{2\pi \left(E_{|L\rangle_i} - E_{|R\rangle_k}\right)}{\hbar} \frac{R_Q}{R} \left[1 + \coth\left(\frac{E_{|L\rangle_i} - E_{|R\rangle_k}}{2k_B T}\right)\right] |{}_i\langle L\,|\Phi|\,R\rangle_k|^2 \quad (3.3)$$

It is worth noting that, once all the parameters that characterize a rf

SQUID qubit device have been determined, it is possible to fully evaluate numerically all the values for the energy levels and for the matrix elements contained in equation (3.3), leaving only the ratio R_Q/R as a fit parameter, where $R_Q = h/4e^2$ and R is an equivalent shunt resistor across the qubit's junction representing the dissipation associated with the system. It is safe to assume that at the base temperature of the dilution refrigerator only the lowest energy level in the upper well is significantly populated and may contribute to the tunneling. Furthermore only transitions between nearest levels are relevant, therefore we will limit the discussion to the tunneling probabilities $\gamma_{i,k}$ and $\gamma_{i,k+1}$, where the energy levels have been chosen so that $E_{|R\rangle_k} < E_{|L\rangle_i} < E_{|R\rangle_{k+1}}$. Therefore the escape rate for very low temperature can be calculated according to

$$\Gamma = \gamma_{0,k} + \gamma_{0,k+1} \tag{3.4}$$

As the temperature increases also excited levels in the upper well may contribute to the escape process. In this more general case the total escape rate can be obtained by considering the tunneling probabilities of all the energy levels that can contribute to the tunneling process, weighted by their relative population, thus yielding the following equation:

$$\Gamma = \sum_{i,k} \left(\gamma_{i,k} \frac{\rho_i}{\rho} \right) \tag{3.5}$$

Where ρ_i/ρ represents the population of the i-th energy level, expressed using the Boltzmann distribution, and the sum is taken over energy levels $E_{|R\rangle_k}$ and $E_{|L\rangle_i}$ such that $E_{|R\rangle_k} < E_{|L\rangle_i} < E_{|R\rangle_{k+1}}$.

Figure 3.8 shows measurements of Macroscopic Resonant Tunneling peaks at 3 different temperatures (200mK, 400mK, and 600mK) fitted using equation (3.5) with $R_Q/R = 1$. All the other qubit parameters have been determined independently according to the measurements that will be described in chapter 4. The fit show a very good qualitative agreement with the data when compared to the overall slope of the escape rate and to the position of the peaks themselves. The dashed and the dotted lines are calculated using Kramers theory for the escape rate of a metastable state subject to thermal fluctuations [75]. According to this theory the escape rate is given by:

$$\Gamma = a_t \frac{\omega_p}{2\pi} \exp\left(\frac{-\Delta U}{k_B T} \right) \tag{3.6}$$

where ΔU is the barrier height. The expression for the prefactor a_t has been

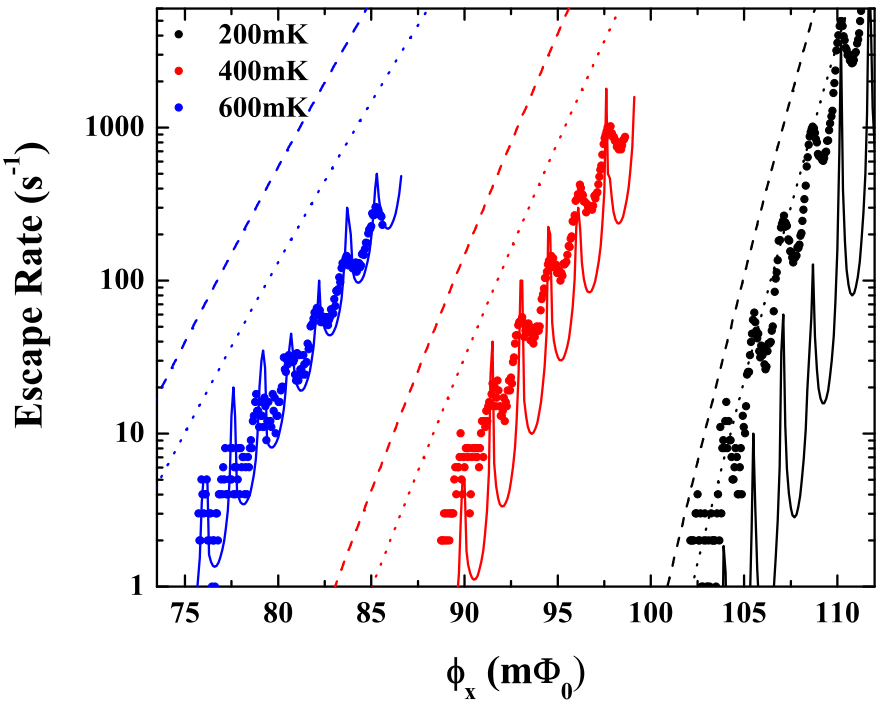

Figure 3.8: Measurements of Macroscopic Resonant Tunneling peaks at 3 different temperatures (dots), along with the theoretical fit using the quantum theory 3.5 with an $R_Q/R = 1$ (solid lines), and using the thermal Kramers formula with a_t given by equation 3.7 (dashed lines) and by equation 3.8 (dotted lines). The fitting parameters are β_L =2.21 C=216.6fF and L=188.5. These parameters have been determined from independent measurements as discussed in chapter 4.

subject of many studies and depends from the level of the damping $\eta = 1/RC$. For these calculations we considered C=216.6 hfF (see chapter 4) and $R = R_Q$, which falls under the condition for low damping $\eta < (\omega_p k_B T/\Delta U)$. In this case, following Kramers theory, the prefactor can be expressed as [76]

$$a_t = \frac{2\pi\eta}{\omega_p}\left(\frac{\Delta U}{k_B T}\right) \tag{3.7}$$

This expression is the one used to obtain the dashed lines in Fig. 3.8. However many other versions of the low damping prefactor have been subsequently obtained. As a comparison we have also reported a calculation (dotted lines in Fig. 3.8) using the following expression of the prefactor calculated by Hänggi [77]:

$$a_t = \frac{\sqrt{1+4/z}-1}{\sqrt{1+4/z}+1}z \qquad where \qquad z = \frac{2\pi\eta}{\omega_p}\left(\frac{\Delta U}{k_B T}\right) \tag{3.8}$$

It is still unclear what the best expression for a_t is although many possible derivation have been suggested [77].

3.3 Measurements of Intrawell Quantum Phenomena

In this section a series of intrawell quantum phenomena will be presented. The effects discussed in this thesis usually involve the ground state and the first excited energy level within a specific well of the quantum potential, therefore the measurement of intrawell phenomena requires the capability to discern between the ground state and the first excited state within the same well, and to determine the population of the first excited state. As it has extensively described in previous sections, the readout mechanism provided by the dc SQUID magnetometer can only discriminate between the two flux states of the qubit, however a readout mechanism that allows measurements of the occupancy of the excited state can be engineered using a fast flux pulse to tilt the potential to a point where the qubit would have high probability to tunnel into the other flux state during the pulse from its excited state and a low probability to tunnel out of the ground state. Then the occupation of the excited state can be extracted from a measurement of escape rate.

The way this technique works can be more easily understood by referring to the cartoon potential reported in Fig. 3.9. The flux pulse needs to be short enough to prevent the qubit form relaxing into the ground state before the measurement is completed. For instance a reasonable potential tilt for a 5 ns

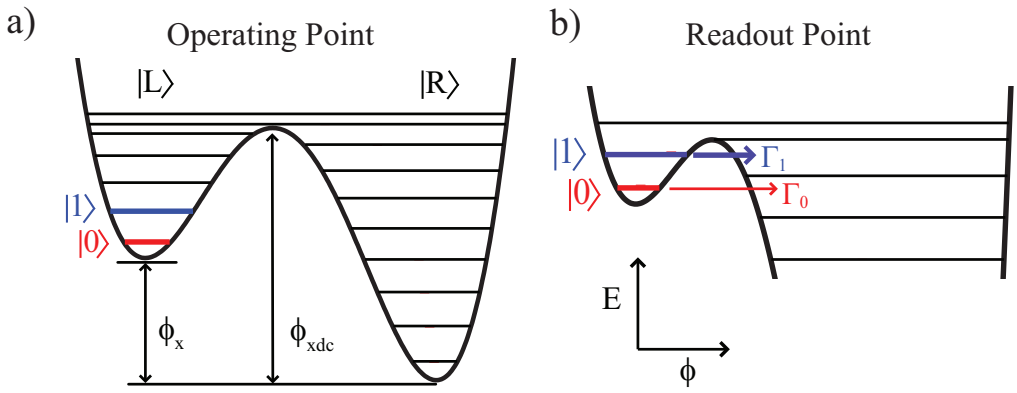

Figure 3.9: The potential and energy levels of a rf-SQUID qubit as a function of flux at a) the qubit operating point and b) during the measurement pulse at the readout point.

pulses, corresponds to a configuration at which the barrier height is ~ 1.1 K. At this point, the ratio between the escape rates from the excited state and the ground state is about $\Gamma_1/\Gamma_0 \approx 460$. However if the lifetime of the excited state is long enough so that the readout pulse can be increased to 10 ns, this ratio of escape rates increases to 950 therefore improving the fidelity of the measurement.

The readout here described is analogous to that implemented for other superconductive qubit, for instance it is closely related to the use of the current pulses to readout phase qubits [66, 78] and to flux pulses used in current biased dc-SQUID qubits [79] in which the pulse tilts the potential and causes a transition to the voltage state for the excited state and not for the ground state.

3.3.1 Lifetime of the Excited State

The first intra-well effect here reported is a measurement of the lifetime of the first excited state in the same potential well. The decay rate (Γ_1) between the first excited state and the ground state in the same well provides an upper limit on the coherence time of the qubit and can be directly extracted by a measurement of the occupation of the excited state, ρ_{11}, as a function of time. For this experiment, the qubit is pumped into the first excited state using a long microwave pulse in order to assure a consistent mixture of the ground and excited state followed by a fast flux pulse to readout the occupation of this state as a function of the delay time between the microwave and the flux pulse τ_{delay}.

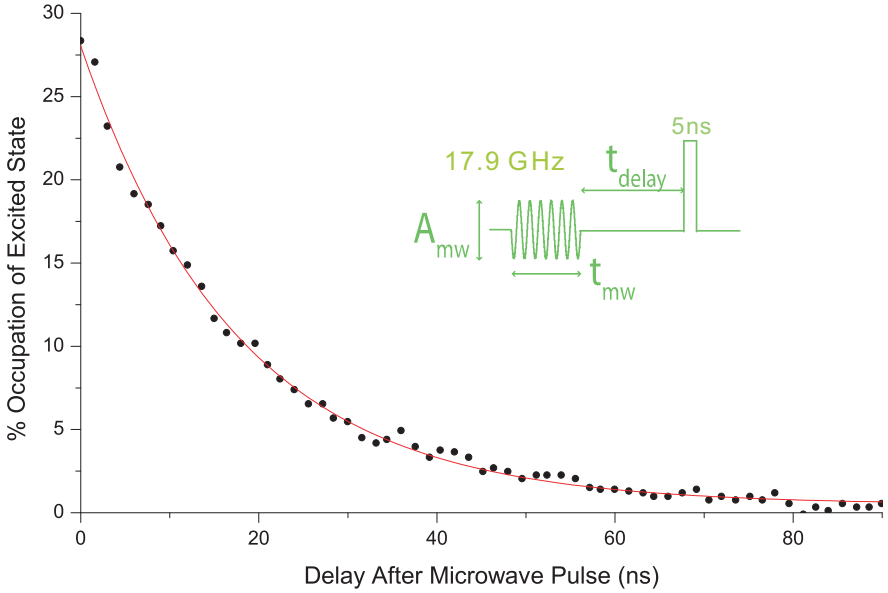

Figure 3.10: The measured occupation of the excited state as a function of delay between the long microwave pulse and the readout pulse. The line is a fit to the exponential decay used to extract T_1

Figure 3.10 shows the occupation of the excited state as a function of delay between the end of the microwave pulse and the readout pulse. For this data the qubit was biased at a $\phi_x = 0.05\ m\Phi_0$. At this bias point the energy difference between the ground and excited state is in resonance with the microwave frequency of 17.9 GHz used for the measurement. The solid line is a fit to the data for an exponential decay with a lifetime of $T_1 = 20ns$. The fit shows good agreement with the data at this bias position.

3.3.2 Level Spectroscopy

The lineshape of the microwave spectroscopy between the ground and excited states in the same well is dependent on the intrinsic lifetime of the excited state and the detuning noise in general, therefore a measurement of the lineshape of the resonant peak at equilibrium with the microwave driving field represents a reliable test for the intrinsic noise affecting the qubit coherence time. The measurement consists of detecting the equilibrium occupation of the excited state near resonance as a function of detuning, δ, from the resonance frequency, and it is made using a readout pulse immediately following a 100 ns microwave pulse, which is much longer than the lifetime of the ex-

cited state as measured in Fig. 3.10, thus ensuring that the qubit has reached an equilibrium mixture of the ground and excited state. For small variation in the driving frequency, the relationship between resonance frequency and ϕ_x bias point can be approximated to be linear. This is of relevance for this experiment, since the power level transmitted to the qubit also depends on the applied microwave driving frequency. To assure a constant level of power transmitted to the qubit, the detuning around the resonance is accomplished by changing ϕ_x , rather than the frequency. For the specific range of bias point used for the data here presented the conversion to frequency detuning is $\delta = 1.70 \times 10^9 s^{-1}/m\Phi_0$, this conversion has been obtained from a measurement of spectroscopy as a function of both frequency and ϕ_x that is reported in Fig. 3.14 from section 3.3.4.

The occupation of the excited state as a function of detuning is shown in Fig. 3.11a for 3 different power settings. The powers used for these measurements were chosen to be in a range where the width is not dominated by power broadening, and it was varied experimentally by mean of room temperature variable attenuators. The attenuators settings corresponding to the shown data were 33, 36 and 39 dB. The power levels were spaced by 3dB, thus giving a factor of two total variation in the microwave amplitude between measurements. For these settings, the linewidth is nearly independent of microwave amplitude. So, one would expect the data to be in the low power limit with a linewidth given by Γ_1. However, the actual linewidth is about an order of magnitude greater, which indicates a broadening due to additional noise.

The effects of extra noise on this resonance between the ground and excited states within one well as well can be described by a set of evolution equations for the density matrix. In describing the resonant transitions between two levels, one needs to separate two types of interactions with the environmental noise. The first one is the decay, with the rate Γ, of the excited state to the lower-energy states within the same well induced by the noise components at frequencies approximately equal to the plasma frequency. The other interaction is due to the noise components at frequencies below the plasma frequency, which induce fluctuations of the energy difference, $\nu(t)$, between the resonant levels. The temperature T of the environment can be assumed to be sufficiently large so that the fluctuations $\nu(t)$ induced by the low-frequency part of the noise can be treated classically. In this case, evolution equations for the elements ρ_{ij} of the density matrix in the basis of the two resonant states that account for both relaxation and the low-frequency noise can be written as [62]

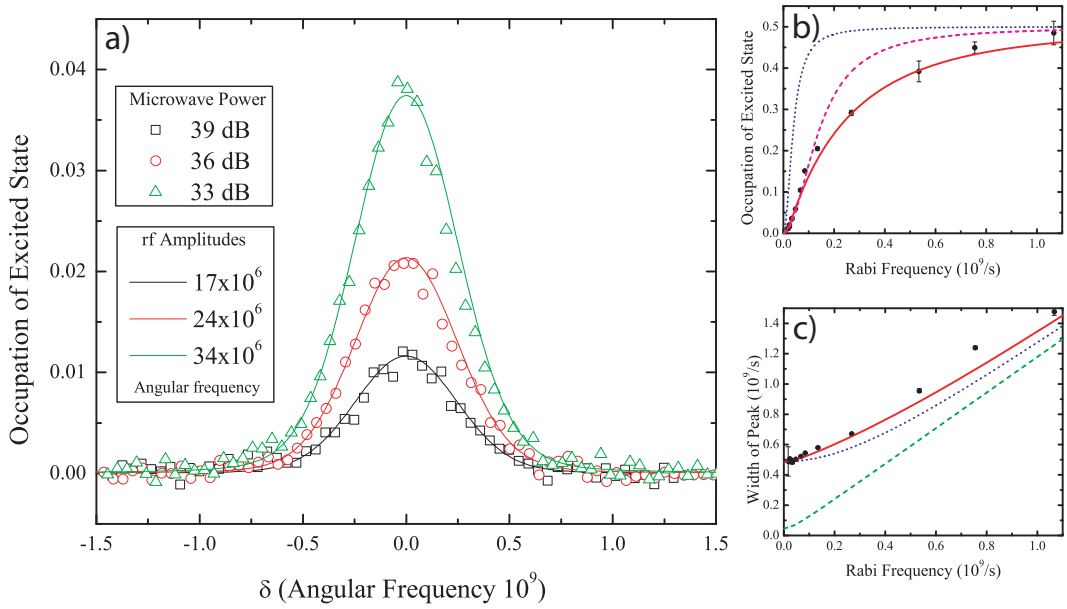

Figure 3.11: a) The occupation of the excited state as a function of detuning for microwave powers corresponding to attenuator settings of 39, 36, 33 dB. Lines are fits using equation (3.11) for microwave amplitudes corresponding to the measured Rabi frequency for each attenuator setting with $\Gamma = 5.5 \times 10^7 s^{-1}$ convoluted with static Gaussian noise with $\sigma = 2.35 \times 10^8 s^{-1}$ at the angular frequencies of the Rabi oscillations that correspond to these microwave powers. b) The occupation of the excited state on resonance versus microwave amplitude in units of the corresponding Rabi frequency. The lines are calculations for the following parameters: red solid $\Gamma = 5.5 \times 10^7 s^{-1}$ and $\sigma = 2.35 \times 10^8 s^{-1}$, blue dotted line $\sigma = 0$ with $\Gamma = 5.5 \times 10^7 s^{-1}$, purple dashed line $\sigma = 0$ and $\Gamma = 2.0 \times 10^8 s^{-1}$. c) The width of the spectroscopic peak from the Gaussian fits as a function of microwave amplitude in units of Rabi frequency. The lines are calculations for the following parameters: red solid $\Gamma = 5.5 \times 10^7 s^{-1}$ and $\sigma = 2.35 \times 10^8 s^{-1}$, green dashed line $\sigma = 0$ with $\Gamma = 5.5 \times 10^7 s^{-1}$, blue dotted line $\sigma = 0$ and $\Gamma = 5.85 \times 10^8 s^{-1}$.

$$
\begin{aligned}
\dot{\rho}_{11} &= i\frac{a}{2}(\rho_{10} - \rho_{01}) - \Gamma\rho_{11}\,, \\
\dot{\rho}_{00} &= i\frac{a}{2}(\rho_{01} - \rho_{10}) + \Gamma\rho_{11}\,, \\
\dot{\rho}_{01} &= -i\nu(t)\rho_{01} - i\frac{a}{2}(\rho_{00} - \rho_{11}) - \frac{\Gamma}{2}\rho_{01}\,, \\
\dot{\rho}_{10} &= i\nu(t)\rho_{10} + i\frac{a}{2}(\rho_{00} - \rho_{11}) - \frac{\Gamma}{2}\rho_{10}\,.
\end{aligned}
\tag{3.9}
$$

This set of equations can describe the effects of extra noise both on the resonance between the ground and excited states within one well and on the resonant flux tunneling rate between levels in different wells (MRT) . The coupling amplitude a of the two states can then be substituted for the tunnel amplitude Δ in the case of flux tunneling between the two wells, or for the microwave amplitude ϕ_{xrf}, expressed as the Rabi frequency Ω on resonance, in the case of the resonance between the two lowest energy levels within the same energy well.

For microwave excitation of the first excited state in the well, Γ is equal to the relaxation rate Γ_1 of this first excited state, and $\nu(t)$ in Eqs. (3.9) is the detuning between the excitation energy of this state and microwave frequency. If the low-frequency noise is negligible, $\nu(t)$ reduces to the average detuning δ, and the steady-state occupation of the excited states is obtained from the stationary solution of the Eqs. (3.9) and assumes the typical Lorentzian shape as a function of δ:

$$
\rho_{11}(\delta) = \frac{\Omega_{Rabi}^2}{4\delta^2 + 2\Omega_{Rabi}^2 + \Gamma^2} \tag{3.10}
$$

in this equation Ω_{Rabi} is the Rabi frequency, Γ is the decay rate from the excited state to the ground state and δ is the detuning from resonance.

The lines in Fig. 3.11a are fits to the data for the equilibrium values of the occupation state, assuming the presence of extra noise at frequencies negligible with respect to either Γ or Ω_{Rabi}. For this analysis the intrinsic Lorentzian lineshape has been convoluted with Gaussian detuning noise.

$$
\langle\rho_{11}(t=\infty)\rangle = \frac{1}{4\sqrt{2\pi}\sigma}\int_{-\infty}^{\infty} e^{-(\nu-\delta)^2/(2\sigma^2)}\rho_{11}(\nu)d\nu \tag{3.11}
$$

where σ is the root mean square value of the low frequency noise and the amplitude of the microwaves is in terms of Ω_{Rabi}. The best fit to the data for all the powers simultaneously, occurs for $\sigma = 2.35 \pm 0.1 \times 10^8 s^{-1}$ and $\Gamma = 5.5 \pm 0.5 \times 10^7 s^{-1}$.

These fit can be extended to higher rf amplitudes where power broadening is important. This analysis is shown in Fig. 3.11b and Fig. 3.11c, which display, respectively, the occupation of the excited state, and the width of the peaks for a wide range of microwave amplitude. Also these data show that the best fit is achieved by including the effect of a gaussian noise into the analysis, using $\sigma = 2.35 \pm 0.1 \times 10^8 s^{-1}$ and $\Gamma = 5.5 \pm 0.5 \times 10^7 s^{-1}$ as fitting parameters.

The static Gaussian noise is required in order to obtain a reasonable fit to the overall lineshape of the data. This seems to confirm that the detuning noise can be considered static and characterized entirely by its rms value when compared to the relaxation rate. However, as a test to the degree to which this fit are really frequency independent, the data in Fig. 3.11a have been fit also assuming Lorentzian noise with an arbitrary frequency cutoff ω_c. A more detailed explanation of this approach is provided in reference [40], here it is worth noting that this approach is only valid in the low power limit, therefore the analysis was limited to only the lowest peak in Fig. 3.11a. As a result it was found that the data can be fit almost as well for values of ω_c up to $2 \times 10^9 s^{-1}$ by increasing rms noise to $\sigma = 2.8 \pm 0.1 \times 10^8 s^{-1}$, thus confirming that the fit provides very little information on the frequency dependence of the noise but gives a rather firm estimate of its amplitude.

3.3.3 Rabi Oscillations

For the experiments so far described a microwave pulse of fixed duration was used. However it is important to turn to experiment in the time domain (variable duration of the microwave excitation) to demonstrate quantum coherence in a qubit. Before discussing the result of the experiment, it should be noted that an analytic solution to the Bloch equations for the population of the excited state in the presence of continuous wave microwave, assuming no decoherence and that the system starts in the ground state at time zero, is given by

$$\rho_{11}(t, \delta) = \frac{\Omega^2}{\Omega^2 + \delta^2} \sin^2(\Omega_{Rabi}(\delta)t/2), \tag{3.12}$$

where

$$\Omega_{Rabi}(\delta) = \sqrt{\delta^2 + \Omega^2}. \tag{3.13}$$

This solution, shows that when driven with microwaves, the population of the excited states oscillates in time (Rabi oscillations), and Ω, the frequency of the oscillations for $\delta = 0$, is ideally proportional to the amplitude of the microwaves excitation ϕ_{xrf}. Both these effects have been observed in a number of different superconducting qubits [80–84] including the rf SQUID qubit

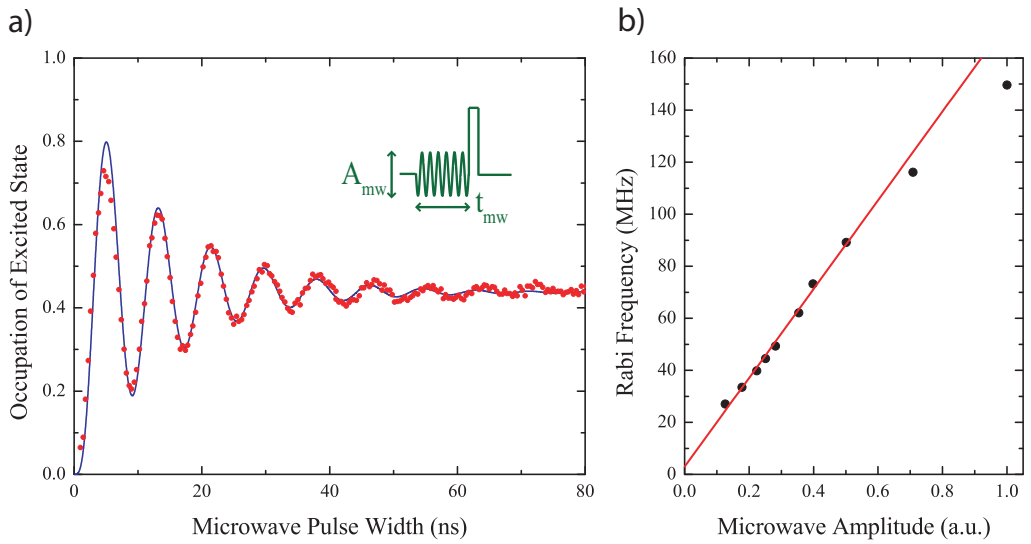

Figure 3.12: a) The occupation of the excited state as a function of the length of the microwave pulse demonstrating Rabi oscillations. The line is a fit to equation (3.24) for $\delta = 0$ averaged over quasi-static noise with $\sigma_\nu = 0.22$ ns^{-1}. This gives $f_{rabi} = 119$ MHz and decay time $\widetilde{T2} = 24$ ns^{-1}. b) The measured Rabi frequency as a function of amplitude of applied microwaves in arbitrary units. The line is a linear fit to the lower microwave amplitude data.

described in this thesis, which also closely follows the linear relationship between the applied power and the Rabi frequency, which provides a convenient means to calibrate the amplitude of the microwaves incident on the qubit. At higher powers the Rabi frequency begins to saturate. There is evidence that at these power levels there is a small probability of excitation to the second excited state. Since the second excited state has orders of magnitude higher escape rate, this small probability can be significant.

The measurement sequence for coherent oscillations consists of a microwave pulse of variable duration immediately followed by the readout flux pulse. This signal, on the high frequency line, is illustrated in the inset in Fig. 3.12a which also shows an example of the Rabi oscillations measured at resonance ($\delta = 0$). For these data each point corresponds to the average of several thousand measurements for a given pulse length and the microwave driving frequency was $f_{xrf} = 17.9$GHz. This frequency lies in a range of the energy spectrum where the effect of spurious two level system is minimum (as it will be clear in section 3.3.4), making it the region with the best response when observing coherent oscillations between the ground and excited states.

In order to simulate the time dependent dynamics of the Rabi oscillations

in the presence of the low-frequency noise, it is convenient to separate this noise in two parts. One, the quasi-static part, consists of the noise components with frequencies smaller than the linewidth W of the corresponding resonance. Under the conditions of the Rabi oscillations, W is smaller than the strength Ω of coherent rf coupling between the two levels, which on resonance ($\delta = 0$) is equal to the Rabi oscillation frequency. This part of the noise can be taken into account by simple averaging over the static distribution of detuning δ. The second, "dynamic" part of the low-frequency noise has components with frequencies extending beyond W. This noise is here treated making the assumption that the temperature T is larger not only than W, but also the Rabi frequency Ω. In this case, it is possible to characterize this part of the noise as the classical noise with the same constant spectral density S extending above Ω and equal to the spectral density at frequency Ω. With this modification of the decoherence rate, Eqs. (3.9) for the evolution of the density matrix of the two rf-coupled states can be written as

$$\begin{aligned} \dot{p} &= \Omega v - \Gamma p - \Gamma/2\,, \\ \dot{u} &= \delta v - \gamma u\,, \\ \dot{v} &= -\delta u - \Omega p - \gamma v\,, \end{aligned} \tag{3.14}$$

where $p = (\rho_{11} - \rho_{00})/2$ is the imbalance of the occupation probabilities ρ_{00}, ρ_{11} of the ground and excited state, and the real/imaginary parts u, v of the off-diagonal element $\rho_{01} = u + iv$ of the density matrix.

Decaying Rabi oscillations described by the Bloch equations (3.14) lead to some stationary values of the occupation imbalance p and coherences u, v that are established after the decay of the oscillations. The analytic solution of Eqs. (3.14) that corresponds to this process can be written as:

$$A(t) = A_{st} + e^{-\gamma t} \sum_j e^{\lambda_j t} A_j\,, \tag{3.15}$$

where the vectors $A = \{p, u, v\}$ are composed of the elements (3.14) of the density matrix and A_{st} represents the stationary part of the solution:

$$A_{st} = \frac{-1/2}{\delta^2 + \gamma^2 + \Omega^2\gamma/\Gamma} \{\delta^2 + \gamma^2, \Omega\gamma, \Omega\delta\}\,. \tag{3.16}$$

The sum in Eq. (3.15) is taken over the three eigenvalues λ_j of the evolution matrix S:

$$S = \begin{pmatrix} \gamma - \Gamma & 0 & \Omega \\ 0 & 0 & \delta \\ -\Omega & -\delta & 0 \end{pmatrix}, \tag{3.17}$$

which are determined by solving the equation $\det(S-\lambda)=0$. In the range of parameters relevant for the present discussion one root is real:

$$\lambda_1 \equiv \lambda = s_+ - s_- + (\gamma - \Gamma)/3\,, \tag{3.18}$$

and the other two are complex conjugated:

$$\lambda_2 = \lambda_3^* \equiv \kappa + i\omega\,, \quad \omega = \frac{\sqrt{3}}{2}(s_+ + s_-)\,, \tag{3.19}$$

with

$$\kappa = \frac{1}{2}(s_- - s_+) + \frac{1}{3}(\gamma - \Gamma)\,, \tag{3.20}$$

where

$$s_\pm = \left[(q^3 + r^2)^{1/2} \pm r\right]^{1/3}, \tag{3.21}$$

and

$$\begin{aligned} q &= \frac{1}{3}(\Omega^2 + \delta^2) - \frac{1}{9}(\Gamma - \gamma)^2, \\ r &= \frac{\Gamma - \gamma}{3}\left(\frac{1}{2}\Omega^2 - \delta^2 - \frac{1}{9}(\Gamma - \gamma)^2\right) \end{aligned} \tag{3.22}$$

The vectors A_j in equation (3.15) are the projections of the vector $A(0) - A_{st}$ of the deviations of the initial elements of the density matrix from their stationary values, onto the eigenvectors of the evolution matrix (3.17) that correspond to the eigenvalues λ_j. These projections can be found conveniently from the following expression:

$$A_j = \frac{(S - \lambda_k)(S - \lambda_l)}{(\lambda_j - \lambda_k)(\lambda_j - \lambda_l)}[A(0) - A_{st}]\,, \tag{3.23}$$

which for each j, directly cancels out components of the two other eigenvector $k, l \neq j$ in the initial vector $A(0) - A_{st}$.

If the system starts its dynamics in the ground state at $t = 0$, then $A(0) = \{-1/2, 0, 0\}$. In this case, collecting all the known quantities [A_{st} from equation (3.16), the matrix S from equation (3.17), and the eigenvalues λ_j] yields the time dependence of the occupation probability ρ_{11} of the excited

state as

$$\rho_{11} = \frac{\gamma}{2\Gamma}\frac{\Omega^2}{\delta^2+\gamma^2+\Omega^2\gamma/\Gamma}\Bigg[1-\frac{e^{-\gamma t}}{(\lambda-\kappa)^2+\omega^2} \Big\{e^{\lambda t}(\kappa^2+\omega^2-2\kappa\gamma+\gamma(\gamma-\Gamma)-\Omega^2-\delta^2\Gamma/\gamma)+ e^{\kappa t}\big[(\lambda(\lambda-2\kappa)+2\kappa\gamma-\gamma(\gamma-\Gamma)+\Omega^2+\delta^2\Gamma/\gamma)\times \cos\omega t+[\omega^2(\gamma-\lambda)+(\kappa-\lambda)(\kappa\lambda-\gamma(\kappa+\lambda)+ \gamma(\gamma-\Gamma)-\Omega^2-\delta^2\Gamma/\gamma)]\frac{\sin\omega t}{\omega}\big]\Big\}\Bigg]. \tag{3.24}$$

Equation (3.24) gives the decay rate of the Rabi oscillations as $\eta = \gamma - \kappa$. If the decay/relaxation rates in Eqs. (3.14) are small in comparison to Ω, the rate η reduces to the Rabi oscillations decay rate $\widetilde{\Gamma 2}$ obtained previously by Ithier et al. [70], who expressed it in terms of the noise-induced decay rate at the Rabi frequency Γ_ν and the decoherence rate Γ_ϕ as

$$\widetilde{\Gamma 2} = \frac{1}{\delta^2+\Omega^2}\left[\frac{\Gamma}{4}\left(3\Omega^2+2\delta^2\right)+\delta^2\Gamma_\phi+\frac{\Gamma_\nu\Omega^2}{2}\right]. \tag{3.25}$$

As discussed above, at large temperature T, the noise is classical at the Rabi frequency, and one can take $\Gamma_\nu = \Gamma_\phi$. In this case, $\gamma = \Gamma/2 + \Gamma_\nu$, and for weak relaxation/dephasing, the two Rabi decay rates agree, $\eta(\delta) = \widetilde{\Gamma 2}(\delta)$.

The solid line in Fig. 3.12a has been obtained using equation (3.24), including a 0.5 ns time delay for the rise time for the microwave pulse and averaged over a value of quasi-static Gaussian noise in ϕ_x equal to that obtained from the fits to the level spectroscopy data in Fig. 3.11. The fit gives a Rabi frequency $f_{rabi} = 119$MHz and decay rate, $\eta = 0.042$ ns^{-1}, for the oscillations. Equation (3.25), with $\delta = 0$, together with the previously measured value for the decay rate of the first excited state Γ_1 (which is used as the rate Γ in the equations above), and the observed Rabi decay rate η, imply $\Gamma_\nu = 0.01$ ns^{-1}. Even though Ω_{Rabi} is not affected by flux noise to first order for $\delta = 0$, the amplitude of the flux noise in our qubit is large enough to cause a measurable effect. If the flux noise were neglected, it would be necessary to increase η to 0.058 ns^{-1} in order to account for the observed decay. In addition to increasing the decay rate, the low frequency noise also reduces the steady state occupation of the excited state, i.e. its value for long pulses.

The effects of flux noise on the decay of the Rabi oscillation becomes much more pronounced off resonance, for $\delta \neq 0$. Figure 3.13 shows such Rabi oscillations at various detunings over a range of $0 \leq \delta \lesssim 10^9$ s^{-1}. At long microwave pulse times the occupation of the excited state reaches the equilibrium val-

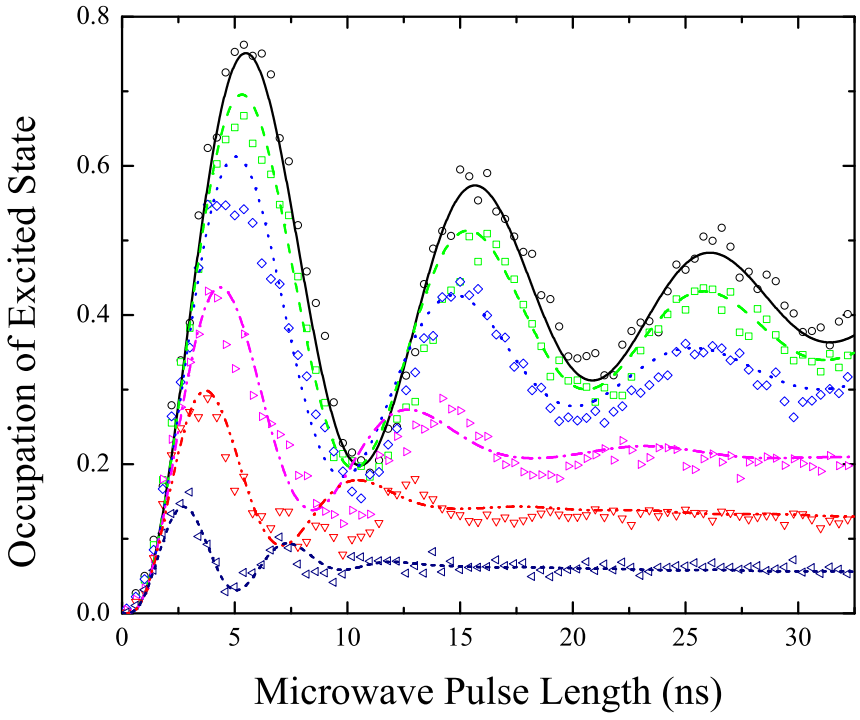

Figure 3.13: Rabi oscillations for frequency detunings going from top to bottom of 0.094, 0.211, 0.328, 0.562, 0.796 and 1.269 ns^{-1} with the corresponding fits using $\Gamma = 0.075\ \mathrm{ns}^{-1}$ and $\sigma_\nu = 0.22\,\mathrm{ns}^{-1}$

ues discussed in section 3.3.2. Near resonance, the value of ρ_{11} for long pulse lengths is determined mainly by the noise amplitude, while for large δ it is set by δ. Also in this case, static Gaussian detuning noise must be included to fit the data over the whole range of detuning. The lines in Figure 3.13 correspond to calculations with an initial Rabi frequency of 0.59 ns^{-1}, $\Gamma = 0.075$ ns^{-1} and $\sigma_\nu = 0.22$ ns^{-1}. For these parameters there is good agreement between the measurement and the calculations further supporting the idea of low frequency noise affecting the data.

3.3.4 Intrawell Phenomena as a function of frequency and ϕ_x

The data for intrawell phenomena so far discussed has been acquired at a fixed frequency over a narrow range of ϕ_x. Contour plots of all these type of measurements over larger ranges of ϕ_x bias points are shown in Fig. 3.14. For all the data displayed in the figure the occupation of the excited state is proportional to the color scale with blue being lower occupation and red being the highest occupation.

Figure 3.14a) shows the occupation of the excited state as function of both frequency and ϕ_x The curving ridge running diagonally from the top left to the bottom right corresponds the resonance between the ground and excited states. The solid lines correspond to a calculation of the energy difference between the nearest eigenstates of the qubit in the same potential well (a more thorough discussion of this calculation will be reported in chapter 4)

There are a few prominent features in the spectroscopy that deserve to be discussed. The most obvious is the horizontal line, which corresponds to a large cavity resonance at a frequency of 17.25 GHz. The second peak of the cavity resonance, not along the resonance between the ground and excited state, has been calculated to correspond to a two photon transition to the second excited state.

The gaps in the spectroscopy most likely correspond to the effect of spurious two level fluctuators in the dielectrics [85]. This effect has also been observed by other groups investigating superconducting phase qubits [28, 29, 86]. Johnson et al. [87] suggested that some of the splittings could be caused by macroscopic resonant tunneling into states in the other well. For the calculation presented along with our data the avoided crossing of the eigenstates show where the MRT peaks would occur. It is possible that some of the splittings are affected by these peaks but there are others that are certainly not related to the MRT. As previously mentioned, the observed two level systems seem to be a likely source of low frequency flux noise that has proven to be

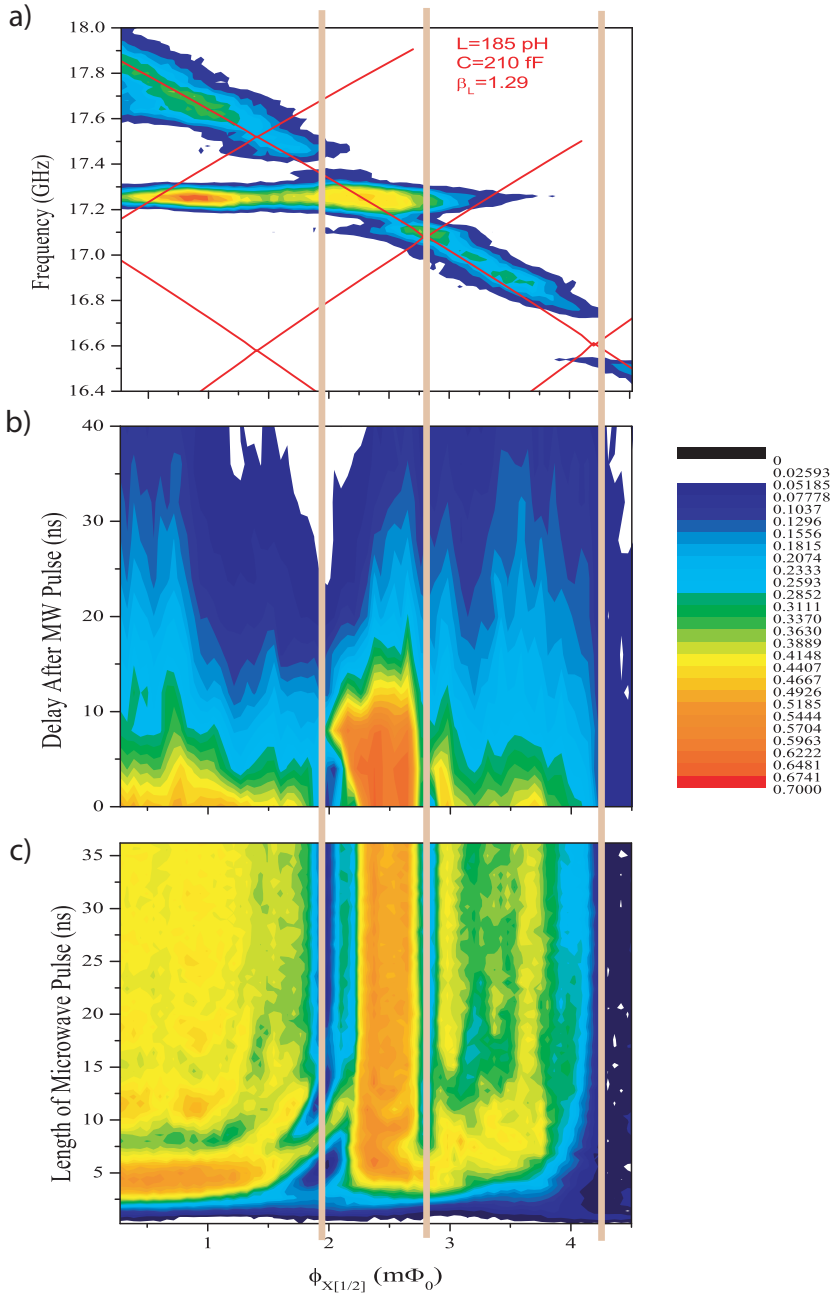

Figure 3.14: a) The measured occupation of the excited state after a long microwave pulse as function of both frequency and ϕ_x. The solid lines are calculations of the energy level spitting between consecutive eigenstates states in the same well. b) The measured occupation of the excited state after a long microwave pulse as function ϕ_x and of the delay between the end of the microwave pulse and the beginning of the readout pulse. c) The measured occupation of the excited state after microwave pulse as function ϕ_x and the length of the microwave pulse.

highly detrimental for quantum coherence. Koch et al. [26] have suggested a model for 1/f flux noise in SQUIDS and qubits where the noise is generated by magnet moments of electrons in the defects of the insulating materials. Due to thermal effects, unpaired electrons hop on and off defect centers in which the electron orientation is locked while in one of the two Kramers-degenerate ground state. The orientation is random from trap to trap and the time an electron resides in a given trap varies over orders of magnitude. The uncorrelated spin orientations sum up to give a $1/f$ power spectrum. When applied to qubits loop, this model results in scaling of the noise amplitude as the fourth root of the area. An alternative source for the decoherence has been proposed due to the non-exponential spin-lattice relaxation of paramagnetic dangling-bonds at the amorphous semiconductor-oxide interface [27]. The scaling of the flux noise with size is similar to the previous theory but since it is an effect of the interface the flux noise is not a function of defects in the substrate, but rather an surface effect. Therefore this latter theory points in the same direction as the recent funding of Gao et al. [71, 72] discussed in section 3.2.3.

The effects of the two level fluctuators can be readily observed on the lifetime of the excited states and on the Rabi oscillations. These measurements are also displayed as contour plots in Fig. 3.14b and 3.14c. Figure 3.14b shows the occupation of the excited state as a function of delay between the microwave pulse and the flux readout pulse and as a function of ϕ_x. Figure 3.14c shows a contour plot of the Rabi oscillations as a function of tilt. For all dataset the microwave frequency was compensated to stay on resonance with the energy spacing between the ground and excited state in the same fluxoid state. In the latter graph the Rabi oscillations manifest themselves as bright spots (peaks) and dark spots (valleys). They are most obvious in the left portion of the plot at ϕ_x values less then 1.25 $m\Phi_0$.

As it is obvious by the guide-lines inserted in the figure, many of the splittings observed in the spectroscopy affect the result of the lifetime of the excited state and of the Rabi oscillations to the point that they clearly manifest themselves as valleys when moving horizontally across the plots. It is also worth pointing out that at a number of bias points, the decay of the excited states is not exponential. In the region near the gaps in the spectroscopy it is possible to observe regions where the decay of the excited states is clearly not exponential. In those regions the occupation of the excited state actually increases with time and reaches a local maximum. It is not possible to observe this effect in an isolated two level system, however it can be explained as caused by two level fluctuators if these are strongly coupled to the qubit [66].

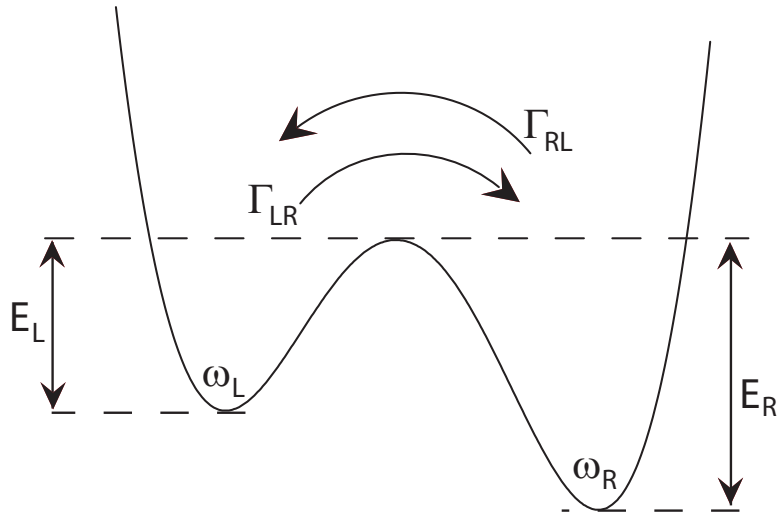

Figure 3.15: A diagram of the qubit potential. Thermal escape occurs forward via the rate Γ_{LR} and backward via the rate Γ_{LR}, the corresponding activation energies are respectively given by E_L and E_R. Here the subscripts L and R stand for Left well and Right well.

3.4 Feasibility of Qubit Control via Barrier Pulsing

In all the experiments so far described the qubit was operated at a constant ϕ_{xdc} value. However the full potential of our qubit design lies in the fact that the barrier height, and thus the tunnel splitting of the flux states, can be manipulated with more complex ϕ_{xdc} signal sequences such as ramping, stepping and fast pulsing, making it possible for instance to realize a measurement of macroscopic resonant tunneling among the rf SQUID lowest lying states [88].

The capability to fast pulse the barrier height can also lead to qubit operation without the use of microwave signals [89–91] which would greatly simplify the large scale implementation of a quantum processor which consists of many qubits. In a highly integrated quantum circuit, spurious cross-talk of the high frequency signal between qubits may become a serious problem meanwhile manipulating the qubit by modifying its energy potential profile, for instance using digital logic signal control, requires a much simpler experimental technique.

To test the feasibility of barrier manipulation with our experimental setup, we used a He3 refrigerator with a base temperature of 395mK to measure the probability for the qubit to be in a specific potential well when thermal equilibrium is reached between the fluxoid states associated with the two wells.

Under the assumption of thermal equilibrium the probability of the system being in a potential well is a time independent function of the potential tilt, and therefore of ϕ_x. There are various ways of calculating this probability. For simplicity, since the base temperature of the He3 refrigerator is well above the temperature of crossover between the thermal and quantum regime, let us begin by considering the classical case represented in Fig. 3.15, in which the forward and backward rates Γ_{LR} and Γ_{RL} are calculated using Kramers theory [75]. Under stationary conditions:

$$\dot{P}_L = -\Gamma_{LR} P_L + \Gamma_{RL} P_R = 0 \tag{3.26}$$

solving this equation together with the condition $P_L + P_R = 1$ yields:

$$P_R = \frac{\Gamma_{LR}}{\Gamma_{LR} + \Gamma_{RL}} \qquad and \qquad P_L = \frac{\Gamma_{RL}}{\Gamma_{LR} + \Gamma_{RL}} \tag{3.27}$$

Where P_R (P_L) is the probability of the qubit state to be in the right (left) well.

The experimental signal sequence, as well as some representative experimental results are shown in Fig. 3.16. Initially the potential is at symmetry with a barrier high enough to forbid transitions between the two wells. Subsequently the ϕ_x signal is modified so that the potential is tilted toward the right well while still keeping the barrier high enough to suppress transitions between the wells. Thereafter, by modifying ϕ_{xdc}, the barrier height is lowered for a time τ long enough to allow for the system to reach thermal equilibrium, i.e. $\tau \gg max(1/\Gamma_{LR}, 1/\Gamma_{RL})$. Finally the system is brought back to its initial potential configuration and is ready to for readout.

The data are compared with both the classical calculation of P_R that lead to equation (3.27), and with another calculation that accounts for the quantum nature of the double well potential. The latter was obtained using the following canonical probability distribution for a system in thermal equilibrium with a heat bath:

$$P_i = \frac{e^{(-E_i/k_B T)}}{\sum_j e^{(-E_j/k_B T)}} \tag{3.28}$$

summing the probability P_i over all the energy levels in the right well, it follows that:

$$P_R = \sum_i P_i \tag{3.29}$$

The data with relative fit are reported in Fig. 3.16b. All the fitting pa-

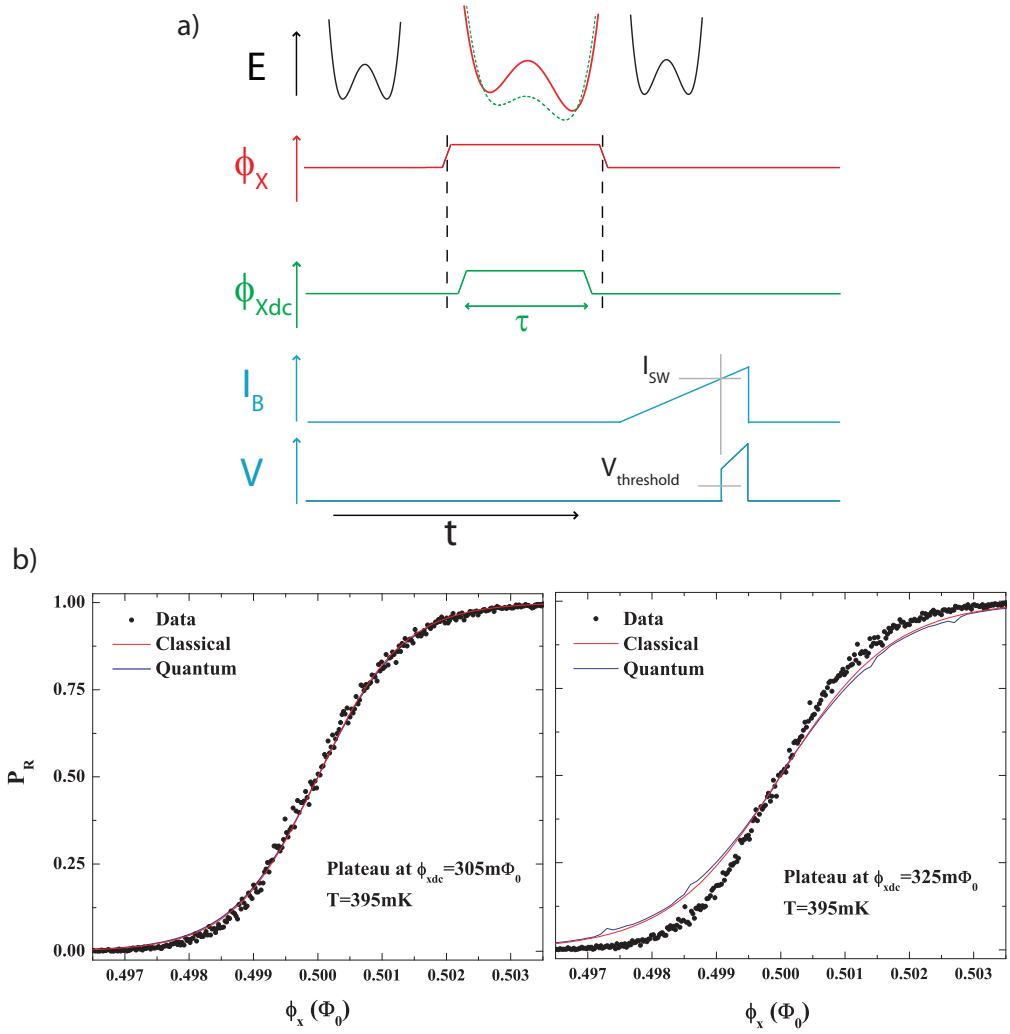

Figure 3.16: a) Outline of the measurement signal sequence, including also barrier manipulation through the ϕ_{xdc} line. The fluxoid state is determined by measuring the value of bias current (I_B) at which the magnetometer switches to the voltage state. b)Measurements of the equilibrium transition probability as a function of the applied ϕ_x at T=395mK along with theoretical fits. On the left data and fits for a ϕ_{xdc} plateau at 305 $m\Phi_0$, on the right data and fits for a ϕ_{xdc} plateau at 325 $m\Phi_0$.

rameters have been independently determined through a set of measurements as it will be explained in chapter 4, therefore no free parameters have been used for these fit. The calculation seem to fit rather well at higher barrier (i.e. lower ϕ_{xdc}) but it starts to fail in the case of lower barrier.

There are two possible explanation for the discrepancy between the theoretical calculations and the data obtained with a plateau at $\phi_{xdc} = 325m\Phi_0$, both related to the possibility that the fluxoid state might undergo unwanted transitions and change when varying the barrier height:

1. The ϕ_{xdc} signal might need optimization.

2. There is a crosstalk between flux lines that causes the potential to also tilt while changing the barrier height.

Let's start by analyzing the first requirement. One problem when pulsing the barrier height is that some unwanted transitions may occur during the ramp between the initial and final configuration of the potential. For a set value of ϕ_x, the probability, ρ, of the system staying in the initial potential well, while raising the barrier height is given by:

$$\frac{d\rho}{dt} = -\Gamma(t)\rho(t) \Rightarrow \rho(t) = exp\left(-\int_{t_0}^{t} \Gamma(t')dt'\right) \tag{3.30}$$

where Γ is the escape rate from a potential well. To simplify the calculation we have used Kramers formula 4.5 for the escape rate in the thermal regime. This is a reasonable assumption considering that the crossover temperature (T_x) between the quantum and the thermal regime for our sample is about 125mK, and the experimental temperature of 395mK under consideration here is well above T_x.

In the case of a monotonic time dependence for ϕ_{xdc} the previous equation can be written as:

$$\rho(\phi_{xdc}) = exp\left(-\int_{0}^{\phi_{xdc}} \Gamma(\phi'_{xdc})\left(\frac{d\phi'_{xdc}}{dt}\right)^{-1} d\phi'_{xdc}\right) \tag{3.31}$$

The results of this calculation for $\phi_x = 503m\Phi_0$ are shown in Fig. 3.17, from which one can see that unwanted transitions can be minimized by trying to implement pulses with a shorter rise time or by further cooling the sample. In our experimental setup we are allowed extra flexibility on the pulses rise time by the presence of the high frequency line that couples from the pulse chip to the qubit ϕ_{xdc} loop, however the He3 cryostat is not equipped with the necessary high frequency lines, therefore the data shown in Fig. 3.16 have been obtained using the ϕ_{xdc} low frequency line and a ϕ_{xdc} signal with a ramp

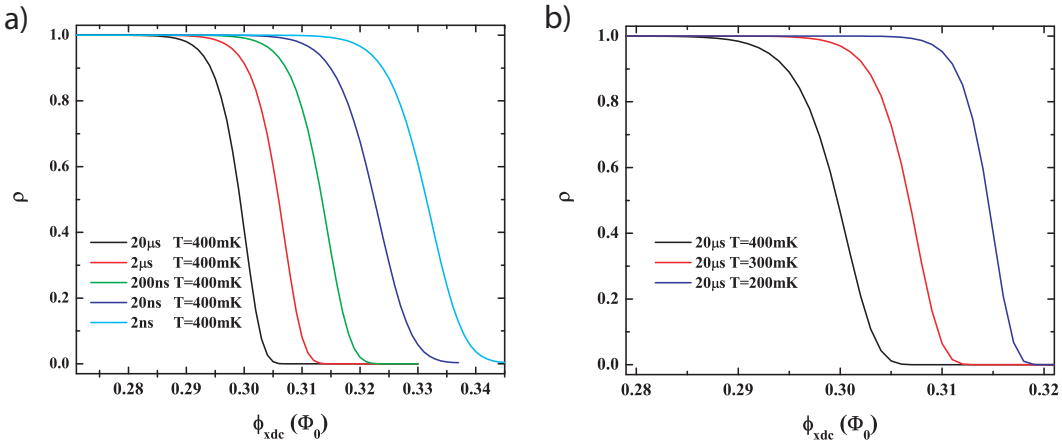

Figure 3.17: Calculation of the probability of the system staying in a potential well while ramping ϕ_{xdc} a) for different ramp rates and b)for different temperatures. All the calculations were performed at a potential tilt corresponding to $\phi_x = 503m\Phi_0$.

between barrier height of $20\mu s$, which is the faster rise time allowed by the RC filter anchored at the 4.2K stage of the refrigerator.

These considerations point into the direction that the ϕ_{xdc} signal may already be optimized with the available setup in our dilution refrigerator which allows for lower temperatures and is equipped with high frequency lines. However, it should be noted again that the calculations are only valid in the thermal regime and to reliably simulate the system below the crossover temperature, it is necessary to modify the model to also account for the quantum nature of the qubit potential.

Let's now discuss the issue of the crosstalk between the ϕ_{xdc} and the ϕ_x lines.

Ideally the gradiometric design of our qubit is such that the effects of the two bias coil, ϕ_x and ϕ_{xdc}, do not interfere with each other. Unfortunately, when characterizing the devices, we have realized that changes in the barrier height via ϕ_{xdc}, also caused an unwanted change on the tilt of the double well potential. Measurements of mutual inductances between the ϕ_{xdc} lines and the qubit have shown the presence of a crosscoupling to the main qubit loop quantifiable in about 30.4fH for the low frequency line and 254.1fH for the high frequency ϕ_{xdc} line. These levels of mutual inductance are such that variations in the ϕ_{xdc} level produce also a significant change in ϕ_x. Figure 3.18 shows the effect of a crosscoupling of 30.4fH on the energy potential. It is obvious from this cartoon that most of the transitions observed while sending a ϕ_{xdc} signal, can be linked to the unwanted tilting of the potential over an actual

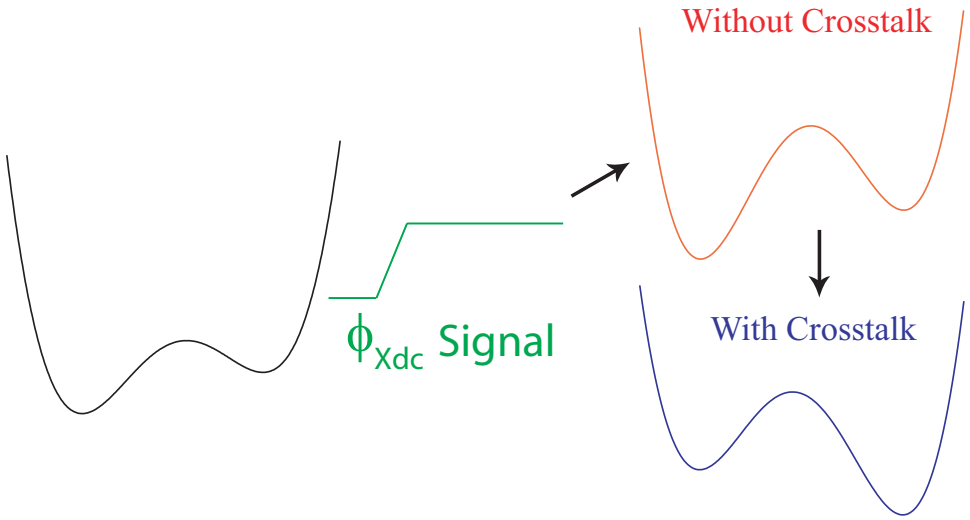

Figure 3.18: Effect of the bias lines crosstalk on the qubit potential.

change of the barrier height. Although the crosstalk could in principle be minimized by using a feedback circuit for an experiment that involves the low frequency lines, realistically the situation is more complicated when designing an experiment in the most interesting case that involves pulses with fast rise times.

At the present stage the only way to pursue experiments involving fast modifications of the potential barrier height is through a redesign of the qubit chip to minimize unwanted signal crosstalk and to optimize coupling between the qubit and both high and low frequency signals.

Chapter 4

Determining System Parameters

4.1 Introduction

The 1D potential and energy spectrum of a rf SQUID can be fully characterized by three parameters: the capacitance C which sets the mass of the particle, the inductance L which sets the energy scale, and β_L which defines the geometry of the potential. All these parameters can be determined in various ways with good accuracy, making the rf SQUID an ideal system for quantitative comparison to theory. It should be noted that the sample used in the experiments contains a dc SQUID loop in lieu of a single Josephson junction, therefore the potential is actually 2D. This requires having to determine also two extra parameters, the ratio of the inductances of the main rf SQUID loop and of the small dc SQUID loop ($\gamma \equiv L/l$), and the asymmetry of the qubit junctions ($\delta\beta \equiv 2\pi L(I_{c2} - I_{c1})/\Phi_0$). In this chapter measurements for the determination of all these parameters are presented along with the mutual inductance calibrations between the qubit and the various bias controls.

4.2 Measurements of the Device Mutual Inductances

The first step toward measuring the various mutual inductances is to measure the qubit magnetic flux. For an rf SQUID, the dependence of the total flux in the loop ϕ on the applied flux ϕ_x is given by [54].

$$\phi = \phi_x - \beta_L \sin(\phi) \tag{4.1}$$

where ϕ and ϕ_x are referenced to zero flux quantum. For $\beta_L = 2.0$, which is close to the experimentally determined value for the qubit sample most widely

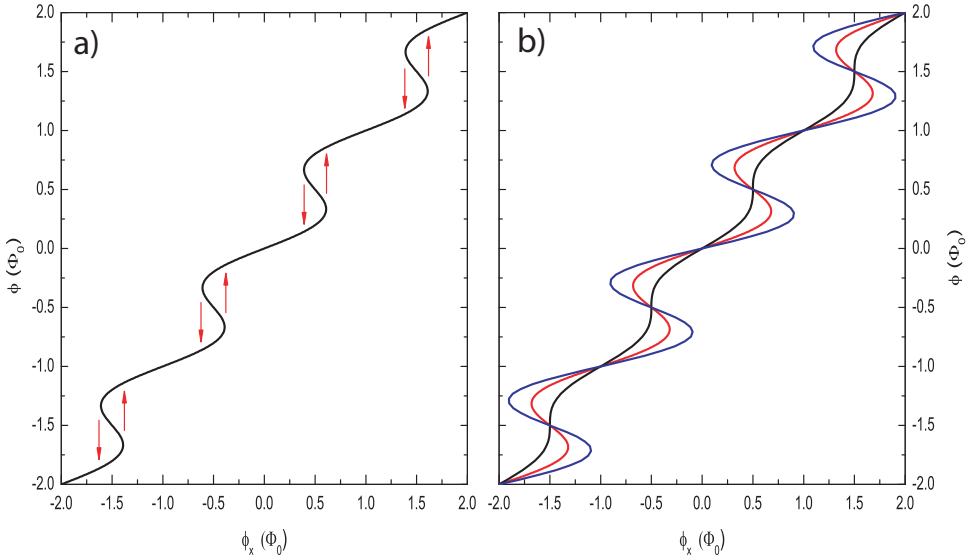

Figure 4.1: a) A calculation of $\langle\phi\rangle$ as a function ϕ_x for $\beta_L = 2.0$. b) To illustrate the dependence of the hysteresis loop on β_L and therefore on ϕ_{xdc}, the same calculation for $\beta_L = 1.0$ (black), $\beta_L = 2.5$ (red), and $\beta_L = 4.0$ (blue)

used for this thesis, the total flux ϕ is plotted in Fig. 4.1a as a function of the external flux ϕ_x applied to the qubit. The periodicity of the curve both in ϕ and ϕ_x can be used to calibrate the applied signals in flux. Another feature of the theoretical curve is that for some values of the external flux, there are three possible values for the total flux. The branch with the negative slope is unstable, but the other two branches are both possible. In this area the qubit has actually two possible flux states and the value of flux measured depends on the previous history. The jump to the other state occurs then roughly at the point and in the direction the arrows indicate in the figure. An experimental measurement of this curve will reproduce either an average between the two flux states or, if an initialization signal is provided to maintain the history consistent over several averages, a hysteresis loop the size of which is a function of β_L and therefore ϕ_{xdc}, as it can be inferred from Fig. 4.1b.

A measurement of the mean switching current I_{sw} in the magnetometer is shown in Fig. 4.2a. The measured average switching current is proportional to the flux in the qubit since the magnetometer was operated in the linear part of the transfer function. For this measurement, the bias flux for the ϕ_{xdc} coil was kept constant. The loops are measured by pulsing ϕ_x in one direction outside the loop for 1 ms to initialize the state of the qubit. The polarity of the initialization pulse determines which branch of the hysteresis loop is being measured. For the case of no initialization (black line), a superposition of the

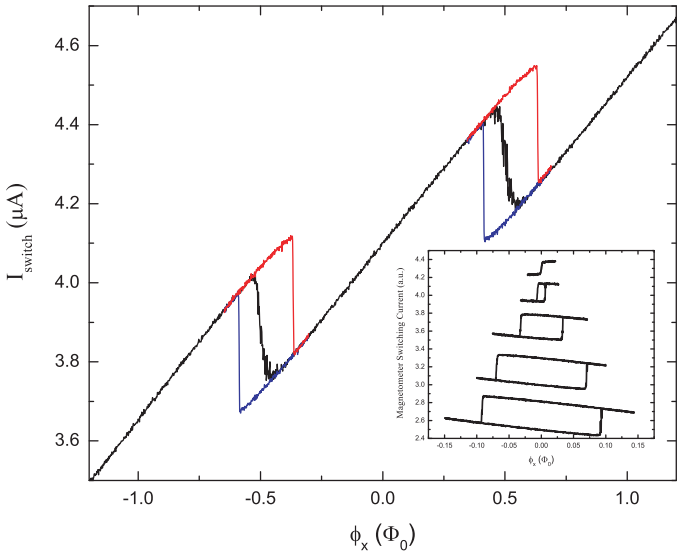

Figure 4.2: A measurement of the mean switching current (I_{switch}) of the magnetometer as a function ϕ_x. I_{switch} is proportional to the mean flux $\langle\phi\rangle$. The black line is for no initialization while the red (blue) lines are for an initialization pulse to left (right) to a point outside the loop. The inset shows measurements of the hysteresis loop at different values of applied ϕ_{xdc}.

two states is obtained.
The distance between two loops corresponds to one flux quantum in ϕ_x. This property is used to calibrate the current sent in the ϕ_x line and to experimentally determine the mutual inductance between the qubit and the ϕ_x bias coil.

As a next step, the same measurement is repeated for different ϕ_{xdc} biases. A typical measurement is shown in Fig. 4.3. These data allows one to calibrate the mutual inductance between the ϕ_{xdc} bias line and the small qubit loop, since one period equals one flux quantum.

The fit used for this data led to $\beta_{L0} = 2.29 \pm 0.09$. This value was obtained under the assumption that the timing between the qubit bias and the magnetometer current bias ramp does not change during the measurement of the different widths, and that the fluxoid state of the qubit switches on average from the metastable state to the other state at the same barrier height that corresponds to a escape rate that would give a significant probability of switching and that has been estimated to be $\Delta U = 5.4\ K$.

In this analysis the inductance only enters as a scale factor and does not have a noticeable effect on the determination of β_{L0}. This value is consistent

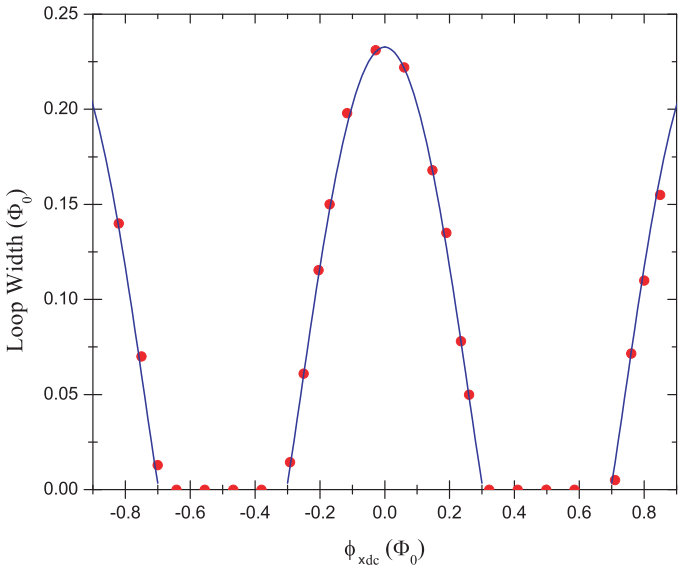

Figure 4.3: The measured width (red circles) of the hysteresis loop of the qubit as a function of flux applied from the ϕ_{xdc} bias coil along with the theoretical (blue line) calculated from the qubit potential for $\beta_L = 2.29$ and $\Delta U = 5.4K$.

with the value calculated using the design size and the critical current of cofabricated junctions. Additionally, the measurements of the hysteresis loop can be used to obtain information about the cross coupling between the flux bias coils.

Ideally the various couplings could be measured and calibrated using the described methods while working at the base temperature of the dilution refrigerator (5 to 10mK), however the small coupling between the ϕ_{xdc} loop and its bias coil requires approximately 8 mA of current to detect a full period of modulation in the measurement of loop width vs applied ϕ_{xdc}. This is enough current in the filter resistors and the bias lines to cause heating and a rise in the base temperature of the dilution refrigerator. This is one of the reason why the mutual inductances are usually tested using a dedicated setup in direct contact with a liquid helium bath whose vapor has been constantly pumped to reach a temperature of 1.5K and a much higher cooling power than the one allowed by the dilution refrigerator. There are two other main reasons to work with this setup. The first one is to have a short experimental turn-around time to check and verify that the chosen qubit sample is fully working and that there are no known problems with the sample cell before investing the time and resources to setup a fridge run. The second reason is that this setup also allows one to test the coupling between the qubit and the ϕ_x and ϕ_{xdc}

high frequency lines located on the pulse chip. This is achieved by temporarily removing the 50Ω terminations from the pulse lines and replacing it with a return path for the bias current, thus allowing us to apply and measure DC currents on the pulse lines. The measurement of the mutual inductances then proceeds in the same way as for the low frequency lines. Once the tests are completed the 50Ω terminations are put back in place, and the sample cell is ready to be mounted in the dilution refrigerator.

4.3 Qubit Parameters

As has already been pointed out, three fundamental parameters (L, C and β_L) characterize the qubit 1D potential, while 2 extra parameters (γ and δ_{Ic}) need to be determined to include corrections due to the fact that the modified rf SQUID is actually fully described by a 2D potential which introduces small corrections to the data analysis calculations. Unfortunately there is no single method to carefully determine all these parameters but a sequence of measurements, both classical and quantum, are needed for determination and verification of the parameters values. A first method to derive one of the parameters (β_L) has already been introduced in the previous section by mean of the best fit to the measurement of the width of the hysteresis loop as a function of flux applied from the ϕ_{xdc} bias coil. The remainder of this section will deal with the other experimental methods that lead to the characterization of the sample.

4.3.1 Mean Flux

A first method to determine the potential parameters is to measure the mean $\phi(\phi_x)$ curve over a flux quantum for different β_L [37] and to fit it with calculations of the equilibrium value of ϕ. This method also allows for an estimate of the extra parameters $\delta\beta$ and γ, whose effects are most clearly seen at values of $\beta_L < 1$ where the complication of having to consider for metastable states has been removed.

To include $\delta\beta$ and γ in the analysis, the mean flux has to be calculated by finding the minimum in the full two dimensional potential of the modified rf SQUID. In terms of flux through the two loops such potential is given by [35]

$$\begin{aligned} U(\phi,\phi_{dc}) &= U_0[\frac{1}{2}(\phi-\phi_x)^2+\frac{1}{2}\gamma(\phi_{dc}-\phi_{xdc})^2 \\ &\quad +\beta_{L0}\cos(\phi_{dc}/2)\cos(\phi)-\delta_{Ic}\beta_{L0}\sin(\phi_{dc}/2)\sin(\phi)] \end{aligned} \quad (4.2)$$

where $\delta_{Ic} \equiv (I_{c2}-I_{c1})/(I_{c2}+I_{c1})$ is the junction asymmetry, $\gamma \equiv L/\ell$ is the

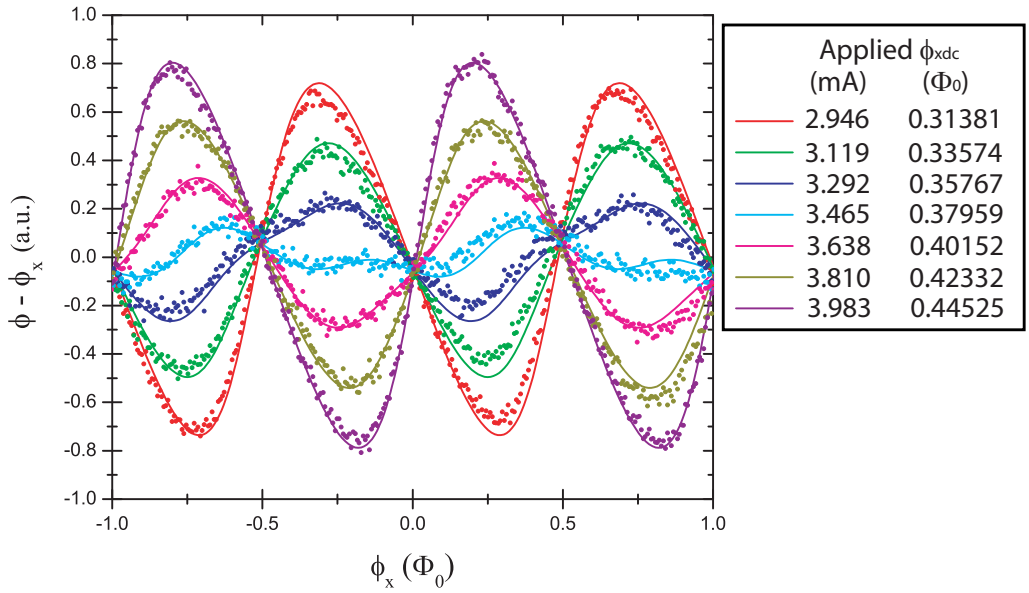

Figure 4.4: A measurement of $\langle\phi\rangle - \phi_x$ as a function ϕ_x at 7 different ϕ_{xdc} values (dots) and a fit to the data (lines) bcalculated by finding the minimum of equation (4.2) with fit parameters $\beta_{L0} = 2.2$, $\gamma = 19$ and $\delta\beta = 0.016$.

ratio of the inductances of the rf and dc SQUID loops and ϕ_{dc} is the flux in the dc SQUID loop. This equation would reduce itself to that of the one dimensional potential with $\phi_{dc} = \phi_{xdc}$ in the case of a small β_l for the small dc loop ($\beta_L \ll 1$) and large γ.

Figure 4.4 shows a measurement of $\phi - \phi_x$ as a function of ϕ_x for various values of ϕ_{xdc}. The lines are the calculations using the minima of equation (4.2) with $\beta_{L0} = 2.2$, $\gamma = 19$ and $\delta_{Ic} = 0.016$. These parameters give the best fit of all the curves simultaneously over multiple periods of ϕ_x.

Generally the largest sources of error arise from the subtraction of the linear portion of the curve and imperfect compensation for the switching current of the magnetometer due to direct coupling between ϕ_x and the magnetometer, however a good determination of the parameters can be achieved since changes in each of the different parameters have different effects on the fit.

The effect of δ_{Ic} is most obvious when observing the shift of the crossings of $\phi(\phi_x)$ for the different β_L away from zero in one direction for integer values of ϕ_x and the opposite direction for half integer values. On the other hand γ provides the tilt of the curves away from a sinusoidal behavior and as it is increased the potential becomes closer to be described by a one dimensional model, therefore the effect of γ becomes less relevant. It is worth noting that the $\beta_{L0} = 2.2 \pm 0.1$ is chosen to simultaneously fit all of the data and that

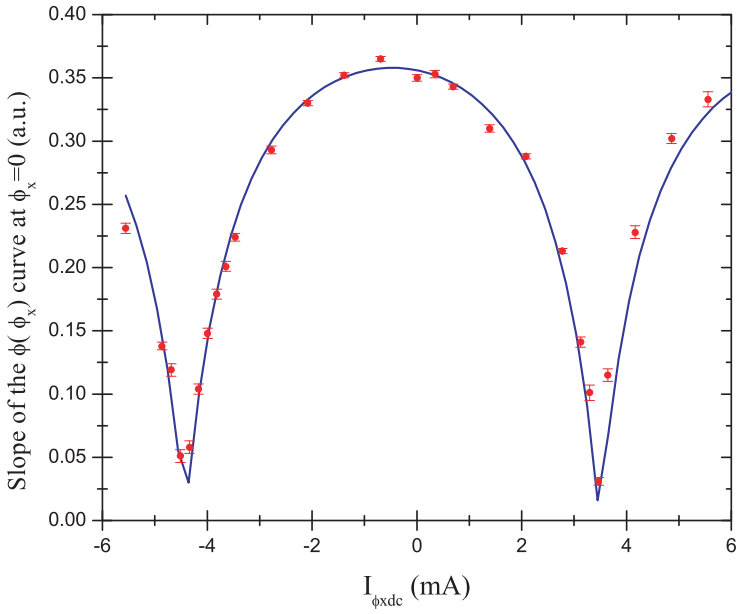

Figure 4.5: The slope of ϕ with respect to ϕ_x at $\phi_x = 0$ as a function of current in the ϕ_{xdc} bias coil. The fit is obtained using a modified version of equation (4.3.1) with $\beta_{L0} \approx 2.3$.

the $\delta_{Ic} = 0.016 \pm .005$ is consistent with the spread in junction size due to the fabrication process [60].

Further information can be obtained from the $\phi(\phi_x)$ curve by repeating the measurement over larger values of ϕ_{xdc} and by extracting its slope around $\phi_x = 0$. equation (4.1) gives the relationship between ϕ, ϕ_x and β_L. Around $\phi_x = 0$, the small angle approximation is valid and equatuin (4.1) becomes

$$\phi = \left(\frac{1}{1+\beta_L}\right)\phi_x \tag{4.3}$$

The relationship between β_L and ϕ_{xdc} is known from equation (1.8). Inserting this into equation (4.3) and reorganizing we than obtain

$$\phi - \phi_x = \left(\frac{1}{1+\beta_{L0}\cos(\phi_{xdc})} - 1\right)\phi_x \tag{4.4}$$

The slope, term in parentheses, of this function at $\phi_x = 0$ is compared with the measured value to obtain the ϕ_{xdc} calibration.

The slope of the measured ϕ as a function of ϕ_x at $\phi_x = 0$ as a function of current in the ϕ_{xdc} bias coil is shown in Fig. 4.5. The fit to the data is done using the slope of equation (4.4) (solid line) using extra parameters to account

for a shift in ϕ_x that was caused by trapped flux and an amplitude to account for the conversion from switching current to flux. The scatter in the data is likely caused by errors in the subtraction of the linear portion in the curve.

This type of analysis allows one to confirm the ϕ_{xdc} calibration and to have yet another way to extract the values of β_{L0}. The period of the modulation is found to be 7.89 ± 0.04 mA/Φ_0 with and offset of -0.47 ± 0.02 mA. The fit to the data gives a $\beta_{L0} \approx 2.3$, however there is a quite large uncertainty in this value because the fit depends strongly also on another free parameter, the amplitude.

4.3.2 Macroscopic Resonant Tunneling

As previously explained in explained in section 3.2, the dynamics of the qubit between flux states in different wells of the double well potential are probed by measuring the escape rate out of a metastable state of one potential well into the other. A measurement of the escape rates for the ground state in the left well as a function of ϕ_x is shown in Fig. 4.6. The peaks in the data correspond to Macroscopic Resonant Tunneling (MRT) between the ground state in the left well and successive energy levels in the right well as the double well potential gets tilted. The red circles correspond to the level splitting squared at each crossing (displayed on the right axis) calculated by finding the successive local minimums of the energy difference between the anti-crossing eigenstates.

The ϕ_x values at which the resonant tunneling peaks are observed depend strongly on β_L and $Z = \sqrt{L/C}$ and can be theoretically calculated, as it has been previously explained in section 1.3. Using the previously determined value of β_{L0} and the experimental value for the applied ϕ_{xdc}, one can use these data to evaluate a Z that best matches the level spacing. For this analysis a $\beta_L = 1.412$ had been used, which is consistent with both the value calculated from the known ϕ_{xdc} and β_{L0} and with the anharmonicity of the data. Using this value of β_L, the best fit to the level crossing is obtained for $Z = 29.5 \pm 0.4$ Ω.

Further information can be obtained from measurements of the Macroscopic Resonant Tunneling data at temperature above the crossover from the quantum to the thermal regime. Specifically in this regime the slope of the escape rates as a function of ϕ_x depends on both the temperature and the height of the barrier between flux states.

Using Kramers theory for the thermal activation over a 1 dimensional potential barrier the qubit inductance (L) can be estimated and β_{L0} can be further refined. According to this theory (see section 3.2.4) the thermal activation

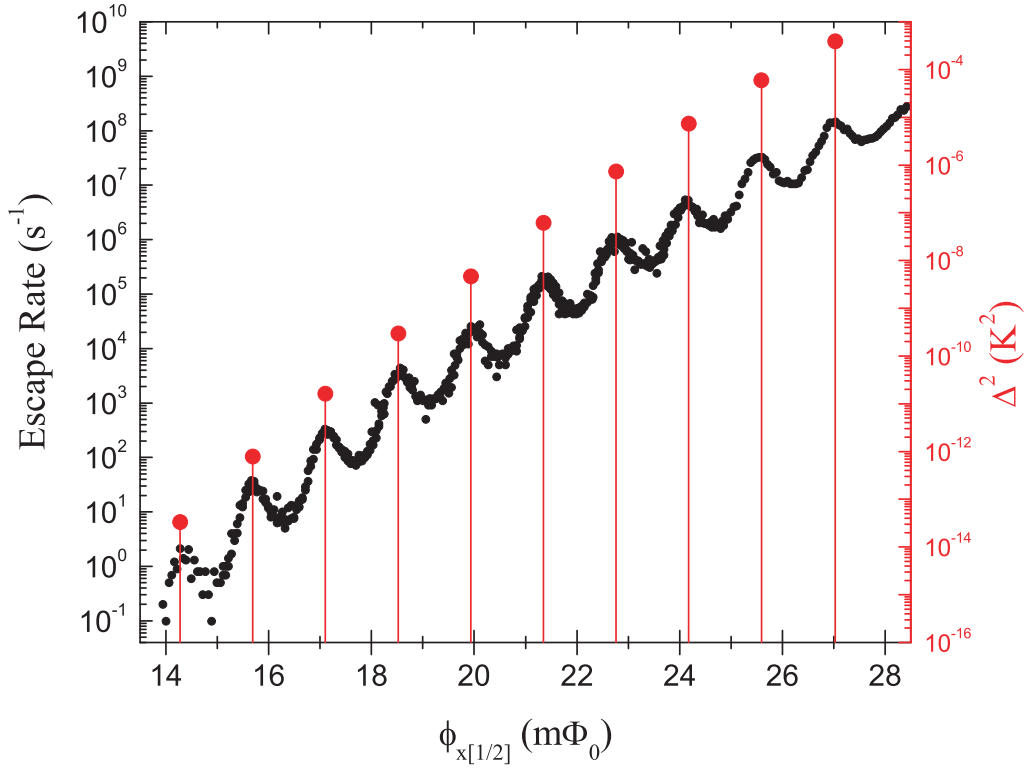

Figure 4.6: The black points, referred to the left axis, are the measured escape rates as a function of ϕ_x. The peaks correspond to the ground state in the left well crossing successive excited states in the right well starting at the 10th and going through the 19th energy level. The red circles with the vertical lines (right axis) are the squared amplitudes of the calculated anticrossings between the ground state in the left well and successive excited states in the right well for values of the parameters $\beta_L = 1.412$ and $Z = 29.5$.

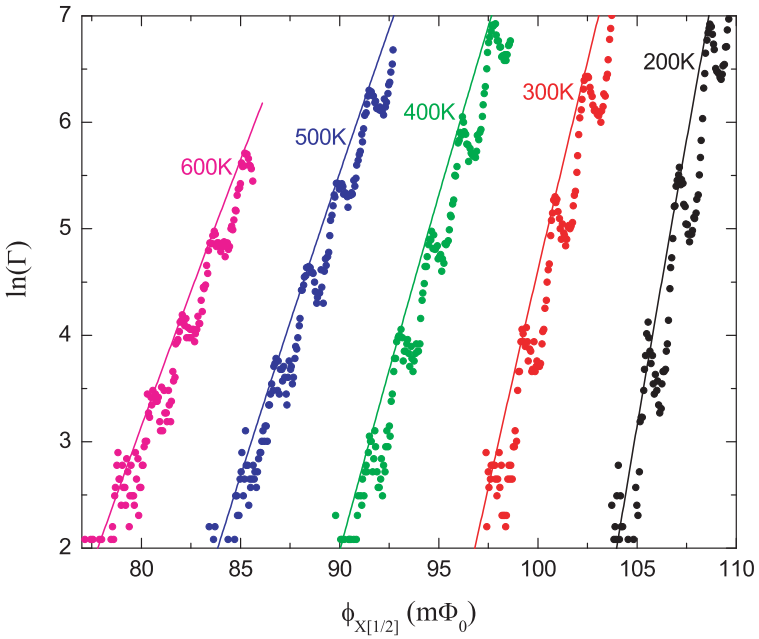

Figure 4.7: The natural log of the measured escape rates as a function of ϕ_x (points) at 5 different temperatures. The lines are the calculated rates using the Kramers formula with parameters $L = 188.5$ pH and $\beta_{L0} = 2.21$.

over a potential barrier has the form of Arrhenius law [75]:

$$\Gamma = a_t \frac{\omega_p}{2\pi} \exp\left(\frac{-\Delta U}{k_B T}\right) \tag{4.5}$$

where ΔU is the barrier height and can be calculated as a function of ϕ_x using equation (4.2), the prefactor a_t contains information about the dampening and k_B is the Boltzmann constant.

The natural logarithm of the measured escape rates rates as a function of ϕ_x is shown in Fig. 4.7 for 5 different temperatures: 200, 300, 400, 500, 600 mK. The temperatures are measured using a calibrated RuO_x thermometer thermally anchored to the mixing chamber of the dilution refrigerator. The figure shows also the calculated thermal escape rates over the barrier at the various temperatures using Kramers formula with parameters $L = 189$ pH and $\beta_{L0} = 2.21$. Since in this analysis the natural logarithm of the escaper rate is considered, the prefactor a_t mostly contributes with a vertical shift and does not affect the slope of the fit. It is worth noting that the data show evidence level crossings, and therefore Macroscopic Resonant Tunneling well above the crossover temperature between the quantum and thermal regime [31], however

for the peaks are not really relevant for this analysis and their presence does not seem to affect the overall slope of the data. The obtained fits to the data give values of β_{L0} that are consistent with what previously measured and and allows us to extract $L = 189 \pm 15$ pH.

4.3.3 Photon Assisted Tunneling

The phenomena of Photon Assisted Tunneling (PAT) can be viewed as a two step process that arises in presence of a continuous microwave radiation that generates photon pumping to higher levels within a well, followed by a tunneling from such excited level in one well to another excited level in the other well. The rate of tunneling into the other well is enhanced at resonance, when both the levels are aligned and the microwave frequency matches the level spacing between the ground and excited state in the left well. For the range of microwave frequency and power amplitude at which the experiments are conducted the pumping can be assumed to happen between the ground state and the first excited level in the left well, whose level spacing strongly depends on $\omega_Q = (LC)^{-1/2}$ and β_L.

A color contours plot of the PAT peaks as a function of both ϕ_x and frequency is shown in Fig. 4.8. The colors represent the experimental tunneling probability with blue corresponding to the lowest value and red to the highest. The theoretical calculation had been carried out using the values and uncertainties previously determined for the parameters other than ω_Q. The best fit to the data is obtained with $\omega_Q = 1.57 \pm 0.1 \times 10^{11} s^{-1}$. The calculation (dashed lines) represents the energy difference between consecutive eigenstates localized in a same well for $\beta_L = 1.412$, $Z = 29.5$ and $\omega_Q = 1.57 \times 10^{11} s^{-1}$.

As the external qubit flux bias (ϕ_x) increases, the potential gets tilted, and the energy difference between consecutive eigenstates in the left well decreases. With reference to Fig. 4.8, for $\phi_x = 12m\Phi_0$ the 11th level and the 9th level are both in the left well and the difference between their energies decreases as function of ϕ_x until there is a crossing with a level in the right well, at which point these levels cross to the right well and their energy difference starts increasing again. This behavior is also observed for several additional levels as displayed in Fig. 4.8b. More generally, the lines with positive slope correspond to the difference between energy levels in the right well while the line with negative slope are associated to the left well. The photon assisted tunneling peaks are then expected to occur at the intersection between the top most negative sloping line and consecutive positive sloping lines. The calculation shows good agreement with the data therefore the fit parameters well describe the qubit Hamiltonian. The non perfect shape of the peak around 18.05 GHz is due to the operational frequency constraints of some of the components in

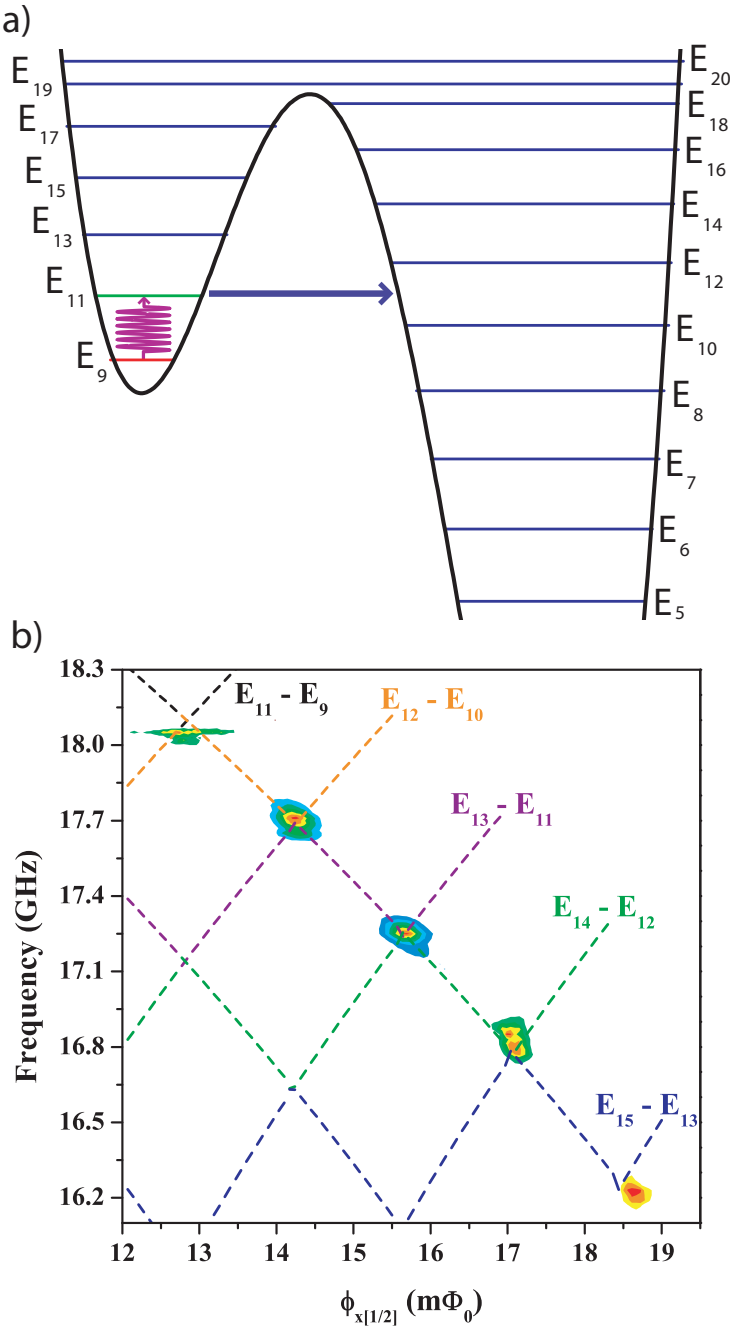

Figure 4.8: a) An energy level diagram at $\phi_x = 12m\Phi_0$ showing the levels involved in photon assisted tunneling. b)The measured escape rates of the PAT peaks shown as color contours (blue the lowest and red the largest) as a function of both ϕ_x and microwave frequency. The dashed lines are the calculated energy differences between consecutive eigenstates localized in the same well for $\beta_L = 1.412$, $Z = 29.5\ \Omega$ and $\omega_Q = 1.57 \times 10^{11} s^{-1}$.

Table 4.1: Qubit Parameters

Parameter	Value	Error	Primary Measurements
β_{L0}	2.21	$\pm.08$	section 4.3.1
L	189 pH	± 9 pH	section 4.3.2
C	217 fF	± 8 fF	section 4.3.3 and 4.3.2
γ	19	$-2, +4$	section 4.3.1
$\delta\beta$	0.016	± 0.005	section 4.3.1

the microwave circuit.

4.4 Conclusion

The final parameters are shown in Table 4.1. These values are generally consistent with all the various measurements, it is however worth noting that different measurements are more sensitive to different parameters. Therefore measurements were analyzed iteratively until a consistent set was found displaying the best overall agreement. The many different types of measurement and the iterative process make it hard to exactly evaluate the error associated with each parameter. The uncertainties displayed in Table 4.1 should be considered as conservative estimates and could be eventually further refined with more measurements over a larger range of flux bias.

phantomsection

Bibliography

[1] Rolf Landauer. Is quantum mechanics useful? *Philosophical Transactions: Physical Sciences and Engineering*, 353(1703):367–376, 1995.

[2] Michael Nielsen and Isaac Chuang. *Quantum Computation and Quantum Information*. Cambridge Press, 2000.

[3] N. David Mermin. *Quantum Computer Science. An Introduction*. Cambridge Press, 2007.

[4] R. Cleve, A. Ekert, C. Macchiavello, and M. Mosca. Quantum algorithms revisited. *Proceedings of the Royal Society of London Sseies A*, 454:339, 1998.

[5] R. P. Feynman. Simulating physics with computers. *Ineternatoional Journal of Theoretical Physics*, 21:467, 1982.

[6] D. Deutsch. Quantum-theory, the church-turing principle and the universal quantum computer. *Proceedings of the Royal Society of London Sseies A*, 400:97, 1985.

[7] P. W. Shor. Algorithms for quantum computation: Discrete logarithms and factoring. In S. Godwasse, editor, *Proc. 35th Annual Symposium on Foundations of Computer Science*, pages 124–134, Los Alamitos, CA, 1994. IEEE Computer Society Press.

[8] Peter W. Shor. Polynomial-time algorithms for prime factorization and discrete logarithms on a quantum computer. *SIAM Journal on Computing*, 26(5):1484–1509, 1997.

[9] Lov K. Grover. Quantum mechanics helps in searching for a needle in a haystack. *Physical Review Letters*, 79(2):325–328, Jul 1997.

[10] David P. DiVincenzo. The physical implementation of quantum computation. *Fortschritte der Physik*, 48:9, 2000.

[11] W.S. Warren. The usefulness of NMR quantum computing. *Science*, 277:1688, 1997.

[12] B. E. Kane. A silicon-based nuclear spin quantum computer. *Nature*, 393:1331, 1998.

[13] J. I. Cirac and P. Zoller. Quantum computations with cold trapped ions. *Physical Review Letters*, 74(20):4091–4094, May 1995.

[14] C. Monroe, D. M. Meekhof, B. E. King, W. M. Itano, and D. J. Wineland. Demonstration of a fundamental quantum logic gate. *Physical Review Letters*, 75(25):4714–4717, Dec 1995.

[15] C. Monroe. Quantum information processing with atoms and photons. *Nature*, 416:238, 2002.

[16] Daniel Loss and David P. DiVincenzo. Quantum computation with quantum dots. *Physical Review A (Atomic, Molecular, and Optical Physics)*, 57(1):120–126, Jan 1998.

[17] M. H. Devoret and J. M. Martinis. Implementing qubits with superconducting integrated circuits. *Quantum Inf Process*, 3(1-5):163–203, October 2004.

[18] J. Clarke and F. K. Wilhelm. Superconducting quantum bits. *Nature*, 453:1031, 2008.

[19] B. D. Josephson. Possible new effects in superconductive tunnelling. *Physics Letters*, 1(7):251 – 253, 1962.

[20] Michael Tinkham. *Introduction to Superconductivity*. Dover Publications, 2004.

[21] John M. Martinis, Michel H. Devoret, and John Clarke. Energy-level quantization in the zero-voltage state of a current-biased josephson junction. *Physical Review Letters*, 55(15):1543–1546, Oct 1985.

[22] Michel H. Devoret, John M. Martinis, and John Clarke. Measurements of macroscopic quantum tunneling out of the zero-voltage state of a current-biased Josephson junction. *Physical Review Letters*, 55(18):1908–1911, Oct 1985.

[23] A. 0. Caldeira and A. J. Leggett. Quantum tunnelling in a dissapative system. *Annals of Physcis*, 149:374–456, 1983.

[24] P. Dutta and P. M. Horn. Low-frequency fluctuations in solids: $1/f$ noise. *Reviews of Modern Physics*, 53(3):497–516, Jul 1981.

[25] D. J. Van Harlingen, T. L. Robertson, B. L. T. Plourde, P. A. Reichardt, T. A. Crane, and John Clarke. Decoherence in Josephson-junction qubits due to critical-current fluctuations. *Physical Review B (Condensed Matter and Materials Physics)*, 70(6):064517, 2004.

[26] Roger H. Koch, David P. DiVincenzo, and John Clarke. Model for 1/f flux noise in squids and qubits. *Physical Review Letters*, 98(26):267003, 2007.

[27] Rogerio de Sousa. Dangling-bond spin relaxation and magnetic 1/f noise from the amorphous semiconductor/oxide interface:theory. *Physical Review B (Condensed Matter and Materials Physics)*, 76(24):245306, Aug 2007.

[28] R. W. Simmonds, K. M. Lang, D. A. Hite, S. Nam, D. P. Pappas, and John M. Martinis. Decoherence in Josephson phase qubits from junction resonators. *Physical Review Letters*, 93(7):077003, 2004.

[29] John M. Martinis, K. B. Cooper, R. McDermott, Matthias Steffen, Markus Ansmann, K. D. Osborn, K. Cicak, Seongshik Oh, D. P. Pappas, R. W. Simmonds, and Clare C. Yu. Decoherence in Josephson qubits from dielectric loss. *Physical Review Letters*, 95(21):210503, 2005.

[30] Konstantin Likharev. *Dynamics of Josephson Junctions and Circuits*. Gordon Breach Science Publishers, 1986.

[31] Richard P. Rouse. *Macroscopic Quantum Phenomenia in an rf SQUID*. PhD dissertation, Stony Brook University, Department of Physics and Astronomy, August 1996.

[32] Jonathan R Friedman, Vijay Patel, Wei Chen, S. K Tolpygo, and James E. Lukens. Quantum superposition of distinct macroscopic states. *Nature*, 406:43–46, 2000.

[33] R. Rouse, Siyuan Han, and J. E. Lukens. Observation of resonant tunneling between macroscopically distinct quantum levels. *Physical Review Letters*, 75(8):1614–1617, Aug 1995.

[34] J. Lapointe, R. P. Rouse, S. Y. Han, and J. E. Lukens. Energy-levels for an rf SQUID potential and their effect on the mean flux. *Physica B*, 194:1645, 1994.

[35] Siyuan Han, J. Lapointe, and J. E. Lukens. Effect of a two-dimensional potential on the rate of thermally induced escape over the potential barrier. *Physical Review B (Condensed Matter and Materials Physics)*, 46(10):6338–6345, Sep 1992.

[36] S. Han, J. Lapointe, and J. E. Lukens. Thermal activation in a two-dimensional potential. *Physical Review Letters*, 63(16):1712–1715, Oct 1989.

[37] Jean Lapointe. *Study of barrier crossing in a macroscopic double-well potetnial*. PhD dissertation, Stony Brook University, Department of Physics and Astronomy, May 1993.

[38] Timothy P. Spiller. Superconducting circuits for quantum computing. *Fortschritte der Physik*, 48:1075–1094, 2000.

[39] Douglas A. Bennett. *Studies of Decoherence in rf SQUID Qubits*. PhD dissertation, Stony Brook University, Department of Physics and Astronomy, December 2007.

[40] D. A. Bennett, L. Longobardi, Vijay Patel, Wei Chen, D. V. Averin, and J. E. Lukens. Decoherence in rf squid qubits. *Quantum Inf Process*, 8 (2-3):217–243, June 2009.

[41] J. B. Majer, F. G. Paauw, A. C. J. ter Haar, C. J. P. M. Harmans, and J. E. Mooij. Spectroscopy on two coupled superconducting flux qubits. *Physical Review Letters*, 94(9):090501, Mar 2005.

[42] R. McDermott, R. W. Simmonds, M. Steffen, K. B. Cooper, K. Cicak, K. D. Osborn, Seongshik Oh, D. P. Pappas, and J. M. Martinis. Simultaneous state measurement of coupled josephson phase qubits. *Science*, 307:1299, 2005.

[43] T. V. Filippov, S. K. Tolpygo, J. Mannik, and J. E. Lukens. Tunable transformer for qubits based on flux states. *IEEE Transactions Applied Superconductivity*, 13:1005–1008, 2003.

[44] M. A. Sillanpaa, J. I. Park, and R. W. Simmonds. Coherent quantum state storage and transfer between two phase qubits via a resonant cavity. *Nature*, 449:438–442, 2007.

[45] J. H. Plantenberg, P. C. de Groot, C. J. P. M. Harmans, and J. E. Mooij. Demonstration od controlled-not quantum gates on a pair of superconducting quantum bits. *Nature*, 447:836–839, 2007.

[46] Henry W. Ott. *Noise Reduction Techniques in Electronic Systems*. Wiley Interscience, 1988.

[47] Ralph Morrison. *Grounding and Shielding Techniques*. Wiley Interscience, 1998.

[48] Low noise precision difet operational amplifier. Technical report, Burr-Brown, 1984.

[49] Jeffery Cain. Parasitic inductance of multilayer ceramic capacitors. Technical report, AVX Corporation.

[50] K. Bladh, D. Gunnarsson, E. Hürfeld, S. Devi, C. Kristoffersson, B. Smålander, S. Pehrson, T. Claeson, P. Delsing, and M. Taslakov. Comparison of cryogenic filters for use in single electronics experiments. *Review of Scientific Instruments*, 74(3):1323–1327, 2003.

[51] A. Fukushima, A. Sato, A. Iwasa, Y. Nakamura, T. Komatsuzaki, and Y. Sakamoto. Attenuation of microwave filters for single-electron tunneling experiments. *Instrumentation and Measurement, IEEE Transactions on*, 46(2):289–293, Apr 1997.

[52] A. B. Zorin. The thermocoax cable as the microwave frequency filter for single electron circuits. *Review of Scientific Instruments*, 66(8):4296–4300, 1995.

[53] M.M. Khapaev, A.Yu. Kidiyarova-Shevchenko, P. Magnelind, and M.Yu. Kupriyanov. 3d-mlsi: software package for inductance calculation in multilayer superconducting integrated circuits. *Applied Superconductivity, IEEE Transactions on*, 11(1):1090–1093, Mar 2001.

[54] Theodore Van Duzer and Charles W. Turner. *Principles of Superconductive Devices and Circuits*. Prentice Hall, 1999.

[55] Antonio Barone and Gianfranco Paternò. *Physics and Applications of the Josephson Effect*. John Wiley and Sons, 1982.

[56] Tatsuya Kutsuzawa, Hirotaka Tanaka, Shiro Saito, Hayato Nakano, Kouichi Semba, and Hideaki Takayanagi. Coherent control of a flux qubit by phase-shifted resonant microwave pulses. *Applied Physics Letters*, 87(7):073501, 2005.

[57] V. Patel and J.E. Lukens. Self-shunted Nb/AlOx/Nb josephson junctions. *Applied Superconductivity, IEEE Transactions on*, 9(2):3247–3250, Jun 1999.

[58] D. Nakada, K.K. Berggren, E. Macedo, V. Liberman, and T.P. Orlando. Improved critical-current-density uniformity by using anodization. *Applied Superconductivity, IEEE Transactions on*, 13(2):111–114, June 2003.

[59] Wei Chen, Vijay Patel, and James E. Lukens. Fabrication of high-quality Josephson junctions for quantum computation using a self-aligned process. *Microelectronic Engineering*, 73-74:767, 2004.

[60] V. Patel, Wei Chen, S. Pottorf, and J.E. Lukens. A fast turn-around time process for fabrication of qubit circuits. *Applied Superconductivity, IEEE Transactions on*, 15(2):117–120, June 2005.

[61] K.C. Gupta, Ramesh Garg, and I.J. Bahl. *Microstrip Lines and Slotlines*. Artech House Inc., 1979.

[62] D. V. Averin, Jonathan R. Friedman, and J. E. Lukens. Macroscopic resonant tunneling of magnetic flux. *Physical Review B (Condensed Matter and Materials Physics)*, 62(17):11802–11811, Nov 2000.

[63] Claude Cohen-Tannoudji, Jacques Dupont-Roc, and Gilbert Grynberg. *Atom-Photon Interactions*. John Wiley and Sons Inc., 1992.

[64] Shawn Pottorf, Vijay Patel, and James E. Lukens. Temperature dependence of critical current fluctuations in Nb/AlOx/Nb josephson junctions. *Applied Physics Letters*, 94(4):043501, 2009.

[65] L. Longobardi, S. Pottorf, V. Patel, and J. E. Lukens. Development and testing of a persistent flux bias for qubits. *IEEE Transactions on Applied Superconductivity*, 17:88, 2007.

[66] K. B. Cooper, Matthias Steffen, R. McDermott, R. W. Simmonds, Seongshik Oh, D. A. Hite, D. P. Pappas, and John M. Martinis. Observation of quantum oscillations between a Josephson phase qubit and a microscopic resonator using fast readout. *Physical Review Letters*, 93 (18):180401, 2004.

[67] Sangkook Choi, Dung-Hai Lee, Steven G. Louie, and John Clarke. Flux 1/f noise in squids and superconducting qubits:localized metal-induced gap states at the metal-insulator interface, 2009. URL http://www.citebase.org/abstract?id=oai:arXiv.org:0907.3904.

[68] Radoslaw C. Bialczak, R. McDermott, M. Ansmann, M. Hofheinz, N. Katz, Erik Lucero, Matthew Neeley, A. D. O'Connell, H. Wang, A. N.

Cleland, and John M. Martinis. 1/f flux noise in josephson phase qubits. *Physical Review Letters*, 99(18):187006, 2007.

[69] P. Bertet, I. Chiorescu, G. Burkard, K. Semba, C. J. P. M. Harmans, D. P. DiVincenzo, and J. E. Mooij. Dephasing of a superconducting qubit induced by photon noise. *Physical Review Letters*, 95(25):257002, 2005.

[70] G. Ithier, E. Collin, P. Joyez, P. J. Meeson, D. Vion, D. Esteve, F. Chiarello, A. Shnirman, Y. Makhlin, J. Schriefl, and G. Schön. Decoherence in a superconducting quantum bit circuit. *Physical Review B (Condensed Matter and Materials Physics)*, 72(13):134519, 2005.

[71] J. Gao, M. Daal, A. Vayonakis, S. Kumar, J. Zmuidzinas, B. Sadoulet, B. A. Mazin, P. K. Day, and H. G. Leduc. Experimental evidence of surface distribution of two-level systems in superconducting lithographed microwave resonators. *Applied Physics Letters*, 92(15):152505, Apr 2008.

[72] J. Gao, M. Daal, J. M. Martinis, A. Vayonakis, J. Zmuidzinas, B. Sadoulet, B. A. Mazin, P. K. Day, and H. G. Leduc. A semiempirical model for two-level system noise in superconducting microresonators. *Applied Physics Letters*, 92(21):212504, May 2008.

[73] Dirk Bluhm. *A deconvolution method for switching current histograms as a fast diagnosis tool*. MA thesis, Stony Brook University, Department of Physics and Astronomy, August 2008.

[74] Peter Kopietz and Sudip Chakravarty. Lifetime of metastable voltage states of superconducting tunnel junctions. *Physical Review B (Condensed Matter and Materials Physics)*, 38(1):97, Jul 1988.

[75] H. A. Kramers. Brownian motion in a field of force and the diffusion model of chemical reactions. *Physica*, 7:284, 1940.

[76] J. Lapointe Siyuan Han and J.E. Lukens. Thermally activated barrier crossings in superconducting quantum interference devices. In Graham R. Fleming and Peter Hanggi, editors, *Activated Barrier Crossings: Applications in Physics, Chemistry and Biology*, pages 241–267, 1993.

[77] Peter Hänggi, Peter Talkner, and Michal Borkovec. Reaction-rate theory: fifty years after kramers. *Reviews of Modern Physics*, 62(2):251–341, Apr 1990.

[78] Matthias Steffen, M. Ansmann, R. McDermott, N. Katz, Radoslaw C. Bialczak, Erik Lucero, Matthew Neeley, E. M. Weig, A. N. Cleland, and John M. Martinis. State tomography of capacitively shunted phase qubits with high fidelity. *Physical Review Letters*, 97(5):050502, 2006.

[79] J. Claudon, F. Balestro, F. W. J. Hekking, and O. Buisson. Coherent oscillations in a superconducting multilevel quantum system. *Physical Review Letters*, 93(18):187003, 2004.

[80] Y. Nakamura, Y.A. Pashkin, and J.S. Tsai. Coherent control of macroscopic quantum states in a single-cooper-pair box. *Nature*, 398:6730, 1999.

[81] I. Chiorescu, Y. Nakamura, C.J.P.M. Harmans, and J.E. Mooij. Coherent quantum dynamics of a superconducting flux qubit. *Science*, 299: 5614, 2003.

[82] D. Vion, A. Aassime, A. Cottet, P. Joyez, H. Pothier, C. Urbina, D. Esteve, and M.H. Devoret. Manipulating the quantum state of an electrical circuit. *Science*, 296:886, 2002.

[83] John M. Martinis, S. Nam, J. Aumentado, and C. Urbina. Rabi oscillations in a large Josephson-junction qubit. *Physical Review Letters*, 89 (11):117901, Aug 2002.

[84] A. Wallraff, D. I. Schuster, A. Blais, L. Frunzio, J. Majer, M. H. Devoret, S. M. Girvin, and R. J. Schoelkopf. Approaching unit visibility for control of a superconducting qubit with dispersive readout. *Physical Review Letters*, 95(6):060501, 2005.

[85] R. McDermott. Materials origins of decoherence in superconducting qubits. *Applied Superconductivity, IEEE Transactions on*, 19(1):2–13, Feb. 2009.

[86] T.A. Palomaki, S. K. Dutta, R. M. Lewis, A. J. Przybysz, Hanhee Paik, B. K. Cooper, H. Kwon, E. Tiesinga, A. J. Dragt, J. R. Anerson, C. J. Lobb, and F. C. Wellstood. Evidence of microstates in dc SQUID phase qubits. In *Extended Abstatracts of the 11th International Superconductive Electronics Conference*, 2007.

[87] Philip R. Johnson, William T. Parsons, Frederick W. Strauch, J. R. Anderson, Alex J. Dragt, C. J. Lobb, and F. C. Wellstood. Macroscopic tunnel splittings in superconducting phase qubits. *Physical Review Letters*, 94(18):187004, 2005.

[88] R. Harris, M. W. Johnson, S. Han, A. J. Berkley, J. Johansson, P. Bunyk, E. Ladizinsky, S. Govorkov, M. C. Thom, S. Uchaikin, B. Bumble, A. Fung, A. Kaul, A. Kleinsasser, M. H. S. Amin, and D. V. Averin. Probing noise in flux qubits via macroscopic resonant tunneling. *Physical Review Letters*, 101(11):117003, 2008.

[89] R. H. Koch, G. A. Keefe, F. P. Milliken, J. R. Rozen, C. C. Tsuei, and J. R. Kirtley. Experimental demonstration of an oscillator stabilized josephson flux qubit. *Physical Review Letters*, 96(12):127001, 2006.

[90] F. G. Paauw, A. Fedorow, C. J. P. M. Harmans, and J. E. Mooij. Tuning the gap of a superconducting flux qubit. *Physical Review Letters*, 102 (9):090501, 2009.

[91] S Poletto, F Chiariello, M G Castellano, J Lisenfeld, A Lukashenko, C Cosmelli, G Torrioli, P Carelli, and A V Ustinov. Coherent ocillations in a superconducting tunable flux qubit manipulated without microwaves. *New Journal of Physics*, 11(1):013009, 2009.

[92] J. B. Majer, J. R. Butcher, and J. E. Mooij. Simple phase bias for superconducting circuits. *Applied Physics Letters*, 80(19):3638–3640, 2002.

[93] C. C. Lim. Indium seals for low-temperature and moderate-pressure applications. *Review of Scientific Instruments*, 57(1):108–114, 1986.

[94] Stycast 2850 ft, technical data sheet. Technical report, Emerson & Cuming. URL http://www.emersoncuming.com.

[95] J. H. Moore, C. C. Davies, and M. A. Coplan. *Building Scientific Apparatus*. Addison-Wesley, London, 1983.

[96] Guy K. White. *Experimental Techniques in Low-Temperature Physics*. Oxford Science Publications, 1989.

[97] O. V. Lounasmaa. *Experimental Principles and Methods Below 1K*. Academic Press, Inc., 1974.

[98] W. David Lee and J. Thomas Broach. Simple, repeatable method for soldering superconducting wire to cryogenic leads. *Review of Scientific Instruments*, 50(10):1312–1313, 1979.

[99] S. V. Radcliffe and J.S. White. Two simple methods for spot welding wires. *Journal of Scientific Instruments*, 38:363, 1961.

[100] Rong Chen and Fuqian Yang. Electrocontact heating in a sn60-pb40 solder alloy. *Journal of Physics D: Applied Physics*, 41(6):065404, 2008.

Appendix A

Development and Testing of a Persistent Flux Bias for a Gradiometric rf SQUID

A.1 Introduction

Reducing possible sources of decoherence, is key to any qubit experiment. In this appendix we primarily address decoherence due to the bias circuitry for the qubit. Our qubit is insensitive to ambient field fluctuations to first order because of the gradiometric design, hence a source of external flux noise is the qubit flux bias. To reduce fluctuations due to the flux bias it is desirable to include a π shift in the qubit allowing operation without external bias [92].

We have integrated an on-chip superconducting shunt inductance in the flux bias coil. The shunt can close the flux bias loop and trap persistent current allowing the external flux bias current source to be switched off during qubit operation. To tune the persistent current, a local heater, which acts as a heat switch, has been coupled to the shunt and makes it possible to drive the shunt to its normal state momentarily to change the flux without evident heating of the whole device at 300 mK.

The schematic of the flux bias lines with filtering is shown in Fig. A.1. We have simulated noise from an external current source as well as Johnson noise from bias, filter and wire resistances at their respective temperatures for coupling to the qubit with and without the inductive shunt. As shown in Fig. A.2 our simulations indicate that the inductive shunt reduces the spectral density of the noise coupled to the qubit by a factor $(L_{sh}/L_p)^2$ where L_{sh} is the inductance of the shunt and L_p is the inductance of the flux bias coil.

In this appendix we discuss the development of an integrated superconduc-

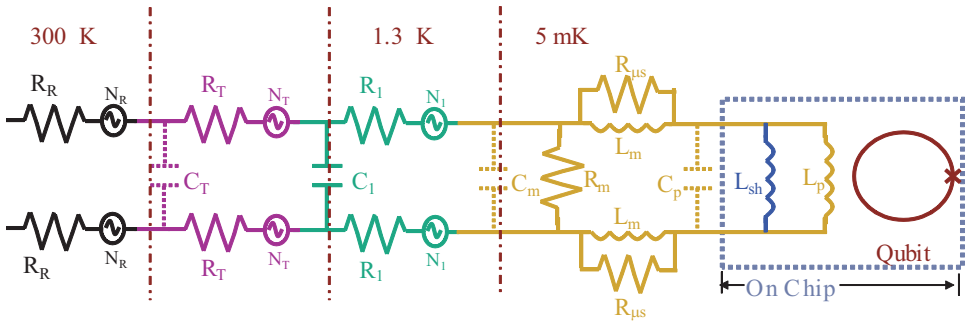

Figure A.1: Schematic of flux bias lines with partial filtering. Calculations of low frequency noise spectra with and without the shunt inductance (L_{sh}) show that the spectral density of the flux noise coupled to the qubit goes as $(L_{sh}/L_p)^2$ and therefore is reduced by a factor 1/100 in our design.

tive shunt to the flux bias, using a test microchip in which the qubit has been replaced by a non-hysteretic dc-SQUID that allows us to study the coupling of the flux bias coil on the dc-SQUID.

A.2 Design and Fabrication

The basic idea is to operate the shunted flux bias coil in a persistent current mode similar to that of a superconducting magnet. To achieve this we have designed an Al shunt to close the flux bias loop and form a continuous superconductive loop. A Cr resistor is fabricated underneath the Al shunt to act as a heat switch. The main flux bias coil is fabricated in Nb ($T_c \approx 9.2K$) so the Al shunt ($T_c \approx 1.19K$) can be driven normal briefly without effecting the main coil. We used 3D-MLSI [53] to calculate the inductances for the circuit. The shunt inductance was designed an order of magnitude smaller than the flux bias coil inductance providing two order of magnitude reduction of the noise spectral density coupled to the qubit.

The important features of the microchip are shown in Fig. A.3. The dc-SQUID magnetometers coupled to the flux bias coil are designed to be non-hysteretic with a β_c of approximately 0.5.

The fabrication process is based on our SAL-EBL process [60] [59] but modified to allow the deposition and patterning of the Cr heater and the Al shunt [65]. The first step has been the patterning of the $Nb/AlO_x/Nb$ trilayer through lift-off. We coated a 50 mm oxidized Si wafer with a layer of PMMA resist then patterned with UV lithography and electron beam lithography (EBL). The trilayer is DC magnetron sputtered in a vacuum system at

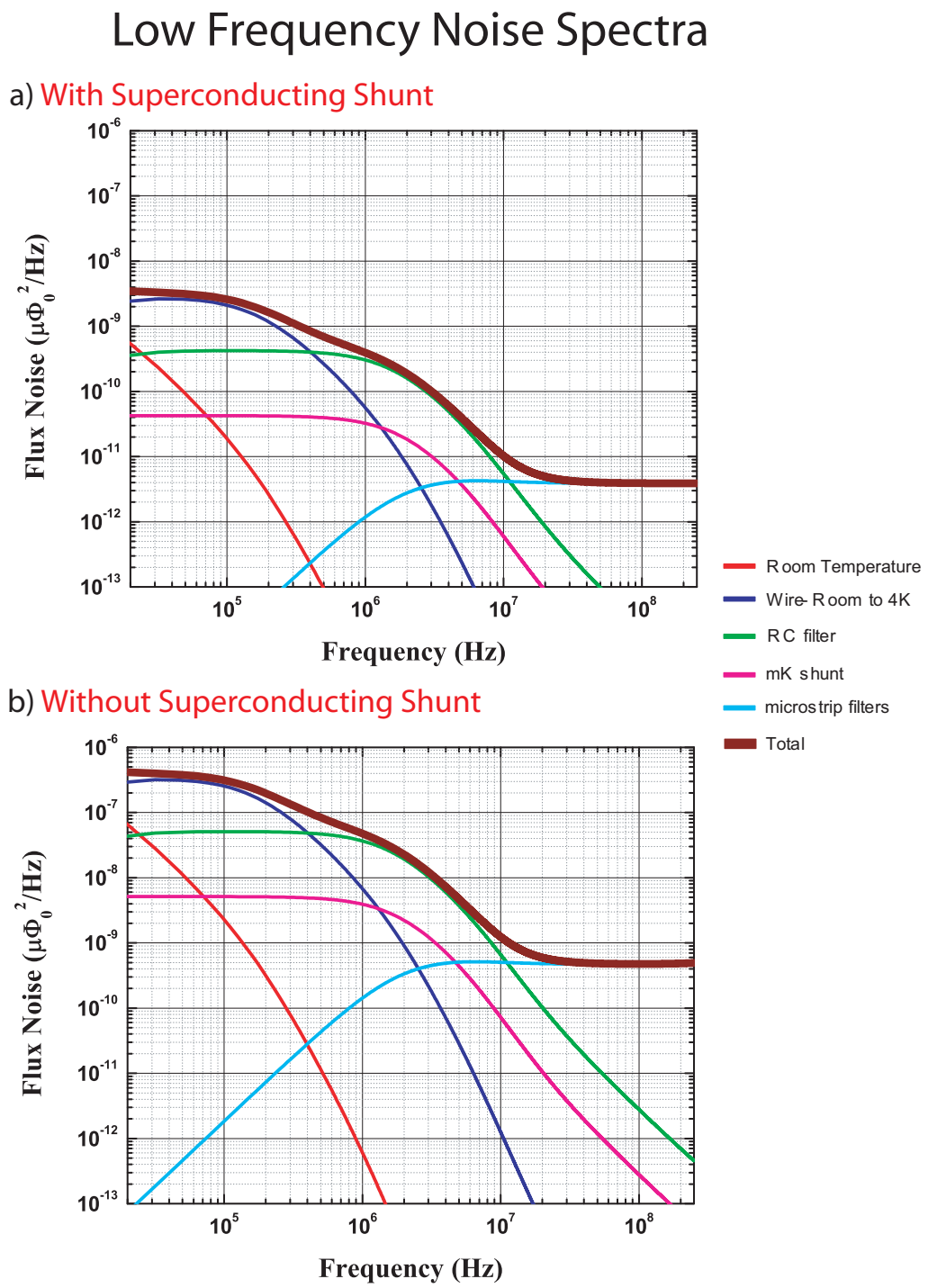

Figure A.2: Calculation of the low frequency noise spectra for the various components of the Φ_x bias circuit a) including the superconducting shunt and b) without the superconducting shunt. For these simulations we used a ratio $(L_p/L_{sh}) = 10$

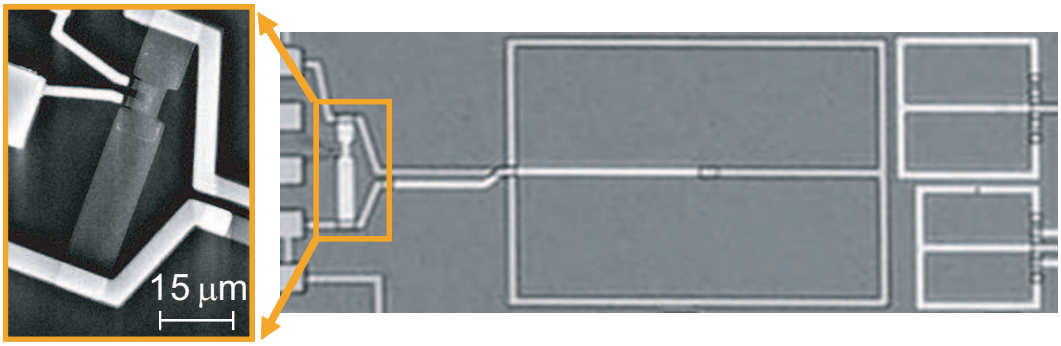

Figure A.3: Test structure for flux bias with superconducting (Al) noise reduction shunt and pulsed heater to reset flux bias at base temperature. The central structure of the chip is the flux bias coil. On the right side of the pictures are shown the two dc-SQUIDs magnetometers used for the measurements. On the left we show a SEM picture of the Al shunt and of the Cr heater.

base pressures around 1×10^{-7} Torr. The deposited Nb base (BE) and counter (CE) electrodes are 150 nm thick while the Al interlayer is 8-10 nm thick. The oxide barrier is formed by thermal oxidation in a static atmosphere of dry O_2.

After the trilayer lift-off, we patterned and defined the junctions (CE) using a UVN-30 resist (from Shipley Inc.) and a Reactive Ion Etch (RIE) in SF_6 plasma. A 200 nm SiO_2 dielectric is then RF sputtered on the wafer. We then completed the self-aligned lift-off by stripping UVN-30 resist and exposing the Nb CEs.

Contact holes are initially defined as junctions and are subsequently formed by SF_6 RIE of the CE followed by an Al wet etch. A 35 nm e-beam evaporated Cr film was used to define the resistors of the magnetometers and the heater. Before depositing the Al shunt we deposited a thin (40 nm) layer of SiO_2 dielectric to isolate the Cr resistor from the shunt.

Next, in order to realize the superconducting shunt, we DC magnetron sputtered 290 nm of Al and patterned it by EBL and lift-off. Finally we formed a 330 nm thick Nb wiring layer, again by lift-off.

A.3 Device Testing

The microchip was mounted inside a copper cell connected to the sample stage of a He-3 refrigerator, which has a base temperature of 300 mK. Magnetic shielding is provided by $\mu - metal$ shields fitted around the vacuum can of the cryostat. The connections to the dc-SQUIDs and bias lines are filtered using

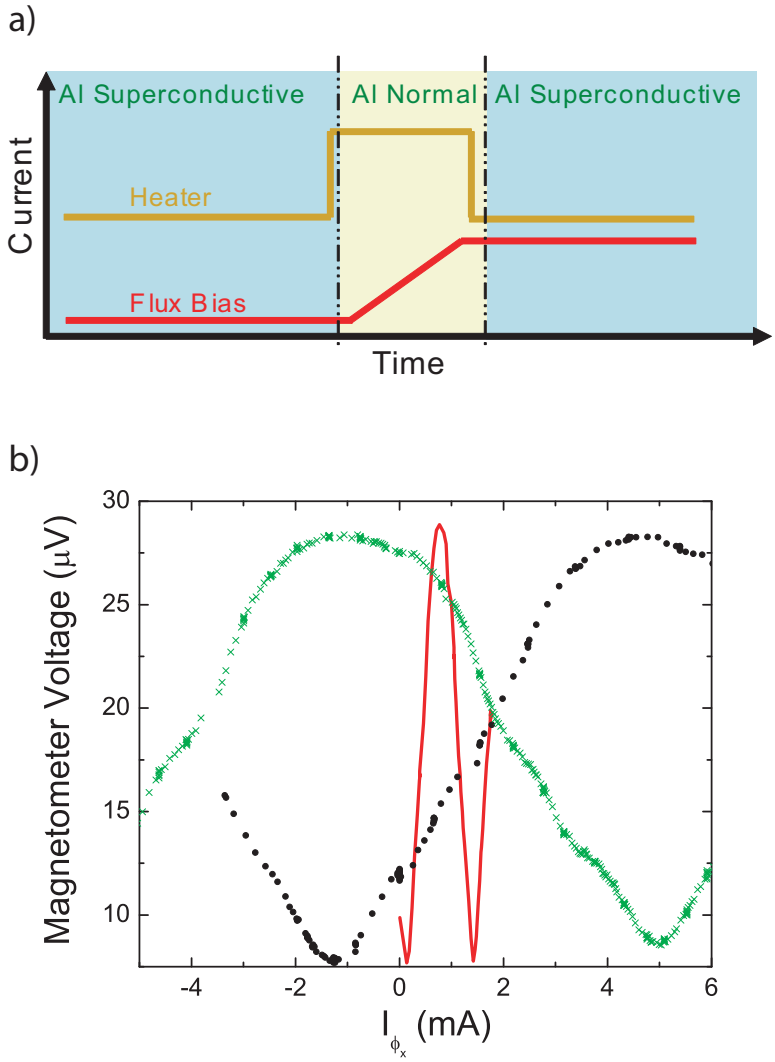

Figure A.4: a) Signal sequence for the operation of the flux bias as an integrated superconductive magnet. The heater is operated using a "heat pulse" of 0.5 μW to induce a transition of the Al shunt into the normal state. The duration of the pulse can be optimized to reduce the energy applied to the chip during the operation. At the same time a ramp is given to the flux bias to "charge" the persistent bias coil. b) Voltage modulation measured using a dc-SQUID magnetometer during the various phases of operation. Before the heat is applied the Al is superconductive and the modulation has a larger periodicity (black dots). During the heat pulse the periodicity is reduced due to the Al being normal (red solid line). After the heat pulse the previous periodicity is restored (green crosses) and the trapped flux can be detected as a horizontal shift in the voltage modulation.

low-pass RC filters anchored at 4.2 K. Because large bias current (in the few mA range) is required for the flux bias lines while the flux bias coil is in a persistent current state, superconducting wire for the flux bias was used between the 1 K and He-3 cooling stages of the cryostat to avoid heating and provide good thermal isolation.

Our circuit consisted of bias and readout lines for the dc-SQUID and bias lines for the flux bias coil and chromium heater. The heater has a resistance of 400Ω and a current of approximately $35\mu A$ (corresponding to a power of about $0.5\mu W$) are required to ensure the transition of the shunt to the normal state. The minimum value for the heater bias current was determined by distinguishing when the magnetometer switched between the two voltage modulation curves corresponding to the two coupling states of the flux bias coil.

When the Al is superconductive most of the current in the flux bias coil will flow through the path with lower inductance, i.e. the shunt, while no current would flow through the shunt when the Al is in its normal state. As shown in Fig. A.4 the transition between the normal and the superconductive state of the Al shunt (or states of high and low coupling) can be detected by measuring the period of the voltage modulation of the dc-SQUID magnetometer biased at a constant current value above the critical current I_c. The two coupling states of the flux bias coil were found to be $1.39mA/\Phi_0$ for the normal state and $11.8mA/\Phi_0$ for the superconductive state.

To demonstrate the persistent flux bias of our coil, we operate the coil in the typical manner as one would operate a large field superconducting magnet. That is, initially the flux bias coil is kept at zero current while the heat switch is off. We then charge the superconducting flux bias coil with current while the Al shunt is resistive (heater on). Figure A.4a shows the bias sequence for the flux coil and heater. First the heater is turned on and biased to drive the shunt normal. Next, current in the flux bias coil is ramped to some desired level (charged). The heater is then turned off to trap the current in the coil. At this point, the room temperature external bias can be ramped to zero and disconnected from the flux bias circuit if so desired. To discharge the coil we simply reverse the process.

Before, during, and after the coil is charged the voltage modulation of the magnetometer dc-SQUID is recorded in order to determine the amount of current trapped by measuring the shift in flux between the two curves. To verify that the coil has trapped a persistent flux we ramp the current back to the initial bias current value before trapping, turn on the heater, and check whether the same modulation curve previously measured is followed while ramping down the coil (discharged). Figure A.4b shows the voltage modula-

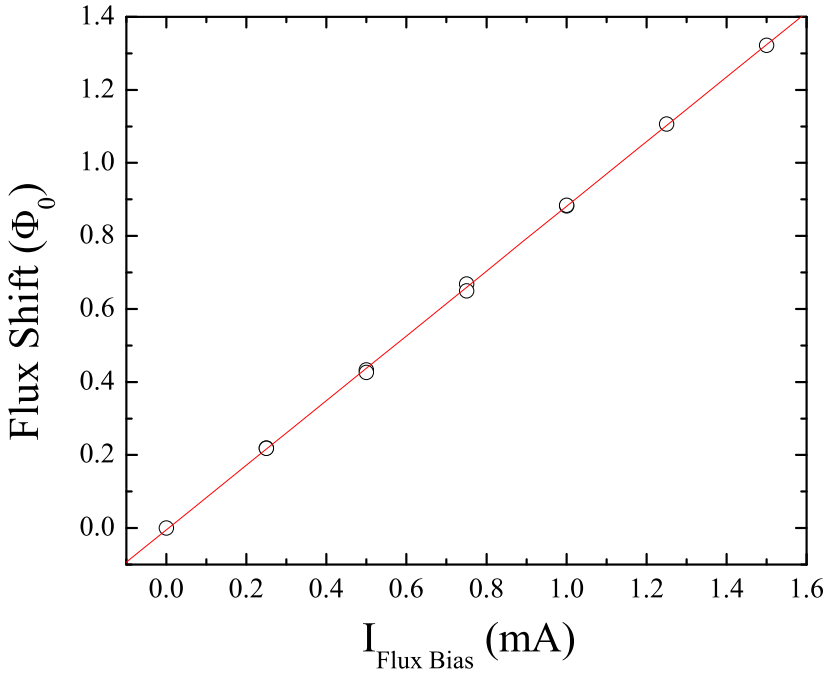

Figure A.5: Measurement of the flux shift vs. the flux bias current at which the flux bias coil is ramped while the Al shunt is in the superconductive state (circles), and linear fit of the data (solid line). From the slope of the linear fit we found that the amount of flux shift is equal to $0.886 \pm 0.004 m\Phi_0/\mu A$.

tions during the steps to charge the flux bias coil. With the heater turned off (shunt is superconducting) the large period curve (black dots) corresponds to the discharged coil. The short period curve (red solid line) corresponds to the charging state of the coil. The other large period curve (green crosses) corresponds to a persistent flux state of the coil after the coil has been charged.

We repeat this measurement for different values of the flux bias current. The amount of persistent flux is obtained from measuring the flux shift between the voltage modulations corresponding to the uncharged and charged states of the flux bias coil and is directly related to the bias current as is evident in Fig. A.5. A flux shift of $0.886 \pm 0.004 m\Phi_0/\mu A$ has been estimated from the slope of the linear fit of the data in Fig. A.5.

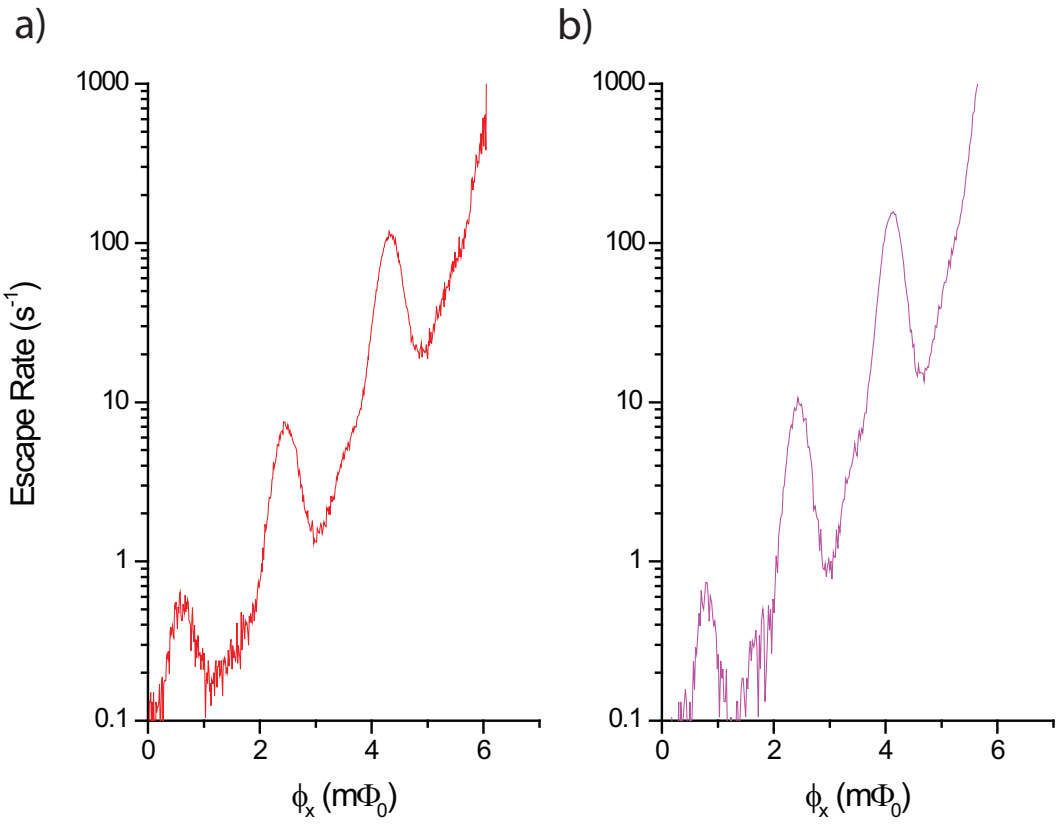

Figure A.6: Measured escape rates as a function of ϕ_x a) with and b) without an aluminum wire bond shunt.

A.4 Conclusion

We have realized an on-chip persistent flux bias for our flux qubit by adding an aluminum shunt to the niobium bias coil. We have also included a heat switch for in-situ modulation of the persistent current. The trapped flux is proportional to the flux bias current applied while the Al shunt is in its normal state. The estimated reduction in the flux noise coupled to the qubit from the biasing circuitry is 100.

As a first check of this idea on a qubit chip, a superconducting aluminum shunt was added to the ϕ_x bias circuit that allowed flux to be trapped in a superconducting loop that included the shunt. The shunt was made by wire bonding across the leads of the bias coil. By setting the current in the loop while cooling through the critical temperature of the Al the amount of flux trapped in the loop is set close to the desired working point. The effects of this modification can be tested using a measurement of macroscopic resonant

tunneling. Fig. A.6 shows resonant tunneling peaks with and without the shunt. There is no obvious change in widths of the peaks, indicating that external bias noise is not the most important source of noise in the qubit device.

Appendix B

Some technical considerations

B.1 Introduction

Many technical challenges arose while setting up the experiment. In this appendix we report a few techniques that have been developed for the realization and maintenance of the experimental setup. Specifically we report on the crucial steps used to make the sample can leak tight, we also report on all the necessary modification that had to be set in place in order to install the sample can into a He3 cryostat while keeping the thermal load to a minimum, and finally we report on an alternative soldering method used to reflow a indium seal used at the vacuum flange of the He3 cryostat.

B.2 Realization of Vacuum Seal and Feedthroughs for the Sample Cell Enclosure

One of the many challenges related to the experimental setup was the realization of a low temperature vacuum seal for the sample cell enclosure. As mentioned in chapter 2 the sample can has two chambers separated by a rf tight block which contains the microstrip filters. The lower chamber houses the NbTi sample cell and can be enclosed using a custom built copper can meanwhile a custom lid has been designed and realized for the top part of the sample can. Both the bottom can and the upper lid are designed to allow for a vacuum seal using an indium wire which can work reliably down to very cold temperatures [93].

When realizing an indium seal it is important that both seal surfaces and the indium are kept as clean as possible, to that extent acetone does an adequate job. Indium can be purchased as wires of a selected diameter from

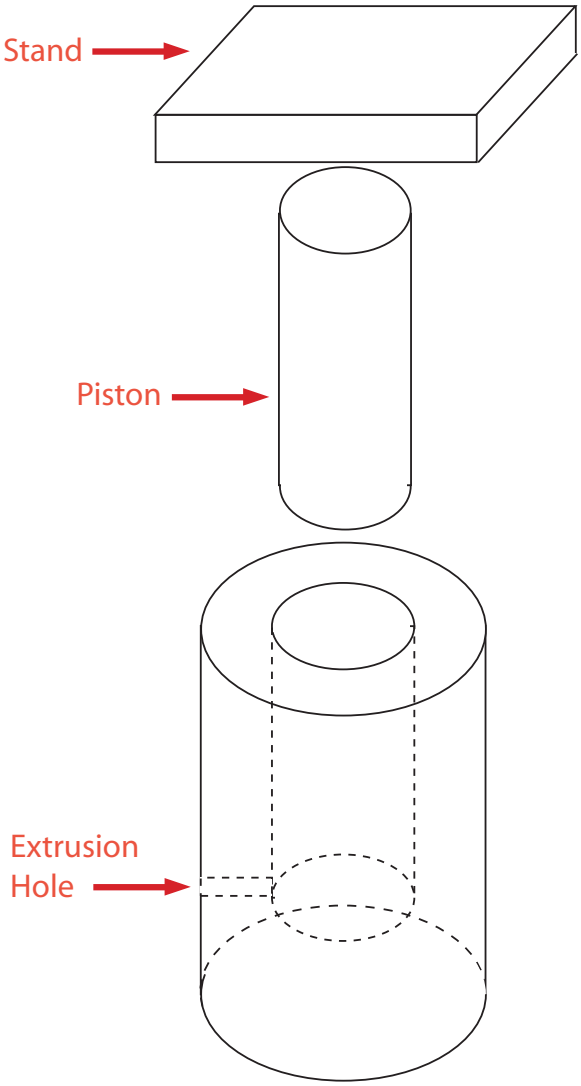

Figure B.1: A diagram of the setup for reclaiming the used Indium. To extrude indium wire it is necessary to apply both pressure and heat.

various vendors. The metal used in our lab was purchased from *Alfa Aesar*, a laboratory chemical supplier, and for a wire of 1.5mm in diameter the cost was just under $100 per meter of length. This cost can be partially offset considering that used indium can be reclaimed and reformed into useful seals. The setup used to recycle used indium (shown in Fig. B.1) consists of a piston, a stand and a vertical 4 inches high cylinder which has been hollowed up to 1/2 inch from the bottom, at which height an horizontal hole of 1.5mm diameter has been drilled. The indium was first melted and poured into the hollow cylinder, then a combination of pressure, from a hydraulic press, and heat, from a butane torch, was used to extrude new indium wire from the setup.

However the biggest task for a fully leak tight sample can was the realization of electric feedthroughs for both low and high frequency lines. Key to solving the problem was the use of STYCAST® 2850 FT from Emerson & Cuming [94]. The STYCAST 2850 FT is a two component highly filled epoxy encapsulant which features high thermal conductivity, a low coefficient of thermal expansion and excellent electrical insulating properties. For our specific application we choose to use a catalyst 24 LV (also from Emerson & Cuming) as a curing agent. The choice of this specific catalyst was dictated by the fact that, once mixed with the stycast, it offers the lowest viscosity, the best response to thermal and mechanical shocks and the best adhesion.

Figure B.2 shows various stages of the realization of the top lid. The vacuum seal for the low frequency lines was realized by feeding a bundle of copper wire twisted pairs [95] through a NiCu tube, and subsequently by pouring cured stycast into a cylindrical mold so that once the epoxy had set, all the twisted pairs and the top part of the NiCu tube would be fully encapsulated into a stycast cylinder.

A similar procedure was used for the high frequency feedthroughs. In this case the lid was machined to house MMCX connectors on the part of the lid that will be housed inside the enclosure and SMA connectors on the outside part. A clean section of copper wire was soldered to the central conductor of a MMCX connector, which was then screwed on the lid. Once all four MMCX connectors are in place, a syringe was used to fill the holes on the outside part of the lid with stycast. Finally the SMA connectors were screwed in place.

In this procedure the most important step is the preparation of the stycast. To remove air bubbles we first slightly warm up the stycast in an oven at 40°C for one hour. We then blend 6.5 to 7.5 parts of catalyst 24 LV by weight for each 100 parts by weight of STYCAST 2850 FT. To ensure a void-free embedment, we used vacuum deairing to remove any entrapped air introduced during the mixing operation. This last process is continued until most of the bubbling has ceased, which usually requires 5 to 10 minutes. This step is

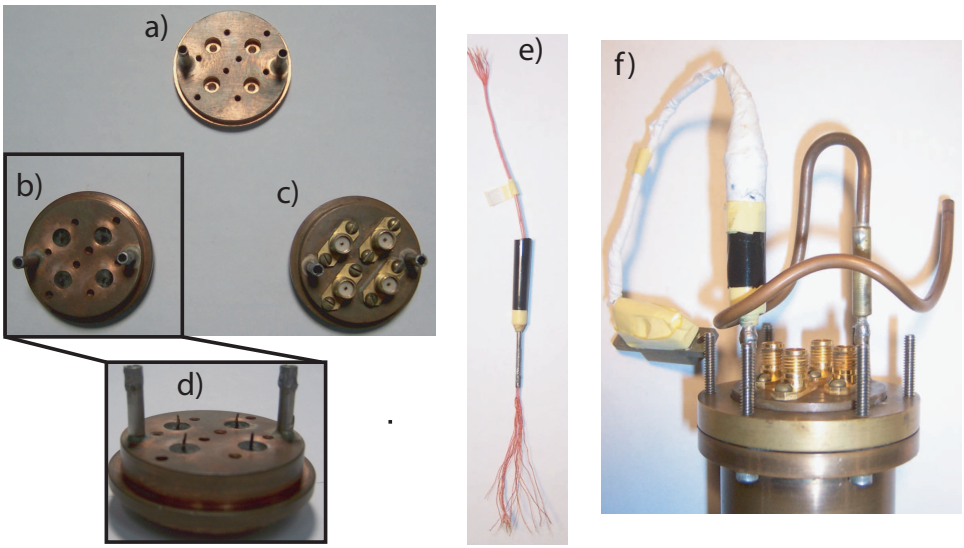

Figure B.2: Pictures of the top lid of the sample can. a) The lid as obtained after Cu machining. b) The lid with high frequency feedthrough obtained using Stycast around the central conductor. c) The lid after the SMA connectors have been installed. d) A side view of the lid after Stycast. e) A picture of the low frequency line feedthrough. f) The lid fully assembled on top of the vacuum can. On the left is the low frequency feedthrough soft solder to a bypass on top of the lid. The second bypass is used to connect a tube for vacuum pumping.

critical. Without vacuum deairing it is very likely that top lid would leak at liquid nitrogen temperatures or lower. Finally, when pouring the mixture in the mold, the adhesion of the mixture to the material to be encapsulated can be improved by gently warming the mold (for instance on a hot plate) to reduce the viscosity of the mixture.

B.3 Set-up of a He3 Refrigerator

Most of the experiments described in this thesis have been performed using a dilution refrigerator, however it is sometimes useful to run some preliminary tests on a microchip using a He3 refrigerator. This type of cryostat has a higher base temperature when compared to a dilution refrigerator but has the advantage of requiring less resources, since it is faster and less labor intensive to set-up for a cooldown, and less liquid He is needed for its operation.

The He3 refrigerator used for our experiments is a He3 Insertable Cryostat manufactured by RMC Research and Manufacturing Company, Inc and it is designed to have a sample stage directly linked to a He3 pot which represents the lowest temperature stage. For a typical experiment a sample cell would be directly attached and thermally anchored to the sample stage, however as described in chapter 2, the sample enclosure used for the work presented in this thesis is bigger and heavier than cells normally used on this particular fridge. When attached to the sample stage the cell might put too much mechanical stress on the He3 line and the pot due to its excessive weight and length. To prevent the sample cell from causing any damage to the structure of the refrigerator, we decided to reinforce the structure by attaching the cell to the 4.2K plate using 4 cylindrical posts, as shown in Fig. B.3. To create a thermal link between the sample stage and the cell we used gold plated copper strips. To improve thermal contact between the gold plated strips and the surface of the sample cell and of the sample stage we used a homemade copper paste realized by mixing together roughly equal quantities of a copper powder with particle size of 44 μm or smaller, from A.D. Mackay Chemicals, and of a high vacuum grease from Dow Corning. The application of the copper paste increased the effective surface contact area of the gold plated strip thus improving the overall cooldown performance of the He3 fridge.

It should be noted that the posts create an unwanted direct link between the sample cell and the 4.2K stage, thus increasing the base temperature of operation. To improve the final temperature that can be achieved by the fridge we employed a few tactics to minimize the heat transfer $\dot{Q}$ from the 4.2K stage.

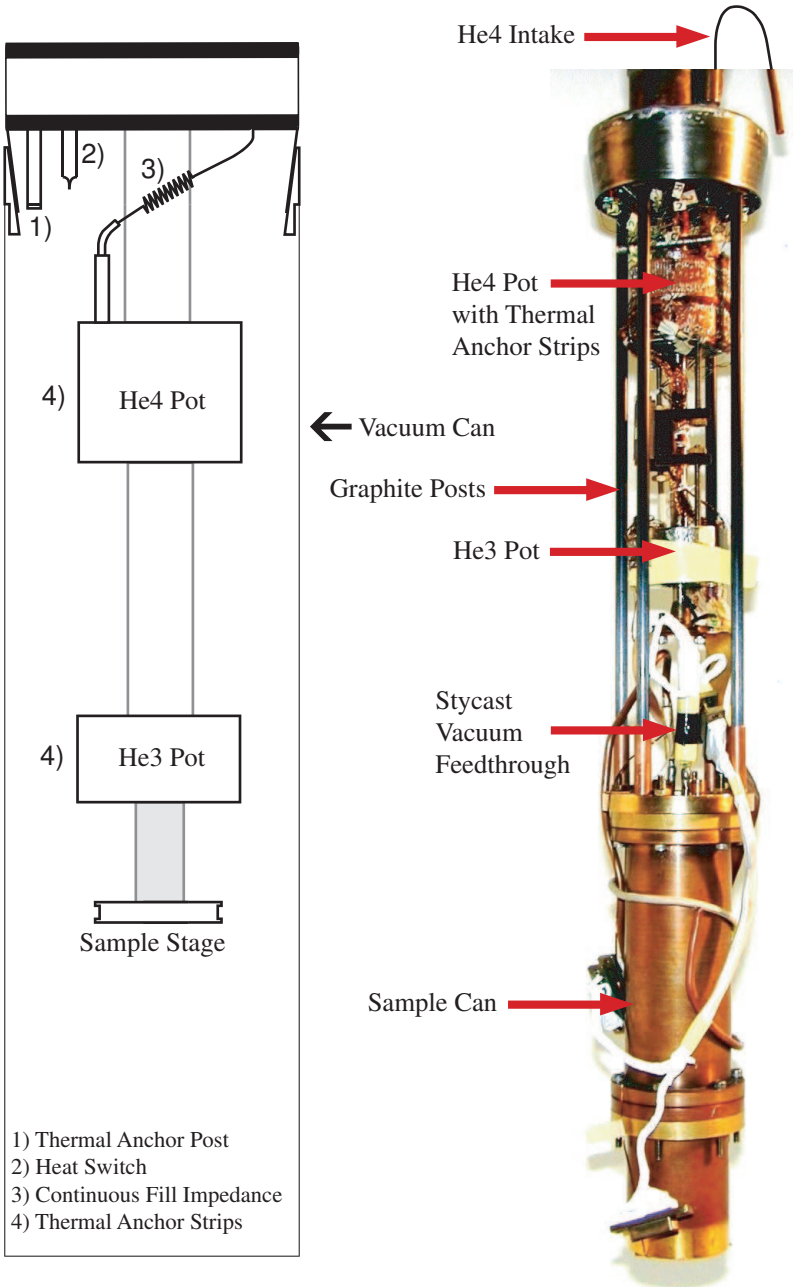

Figure B.3: Schematic (left) and photograph (right) of the lower section of the He3 cryostat. Two gold plated copper strips provide thermal contact between the He3 pot respectively to the top and bottom of the sample cell.

The heat transfer $\dot{Q}$ is given by [96]:

$$\dot{Q} = 4\frac{A}{l}\int_{0.3\ K}^{4.2\ K} d\lambda\ \lambda(T), \tag{B.1}$$

In this formula the factor 4 accounts for the number posts used, A is the cross-sectional area of the posts and l is their length, $\lambda(T)$ is the temperature-dependent thermal conductivity of the material the posts are made of. To reduce the heat transfer we maximized the length of the posts and we minimized their effective area by choosing to use hollow cylindrical tubes rather than rods. The tubes were realized using graphite, which is a sturdy enough material to keep from breaking during thermal cycling and has a low coefficient of thermal conductivity ($\lambda \approx 10^{-4} W/Km$ at 400mK [97]).

To further reduce the thermal load deriving from higher temperature stages in the He3 fridge, we replaced the wiring between the 1.4K stage and the He3 pot, substituting the already existing, resistive, phosphor bronze wires with superconductive NbTi wires which are poor thermal conductor and do not cause any resistive heating. This step allowed to obtain a better stability of the cryostat base temperature during normal experimental operation.

The task of soldering NbTi wires to the existing electrodes is far from trivial. These wires tend to grow a thick oxide that makes them hard to keep clean and most of the time solder would not adhere to the wires even after the surface has been prepared with the application of acid flux. Several method have been engineered in order to realize reliable soldering of superconducting wires [98], for this application we decided to use a spot welding technique [99] that involves terminating the NbTi wires with a platinum foil. The platinum has a thermal conductivity low enough to allow for reliable spot welding of the wire, also it does not require any particular surface preparation for regular solder (in our case a common Sn60-Pb40 alloy [100]) to adhere to its surface, which makes it ideal for the application here described.

After all these improvements had taken place, the cryostat could achieve a stable base temperature of 390 mK.

B.4 Indium Soldering

Figure B.4 shows a cross section of the bottom part of the He3 cryostat. The instrument has a stainless steel vacuum flange which is sealed, using indium wire as solder, to a brass plate. Occasionally, on average every twenty thermal cycles, a low temperature leak opens in the solder and it becomes necessary to realize a new indium seal. Because of the location of the seal

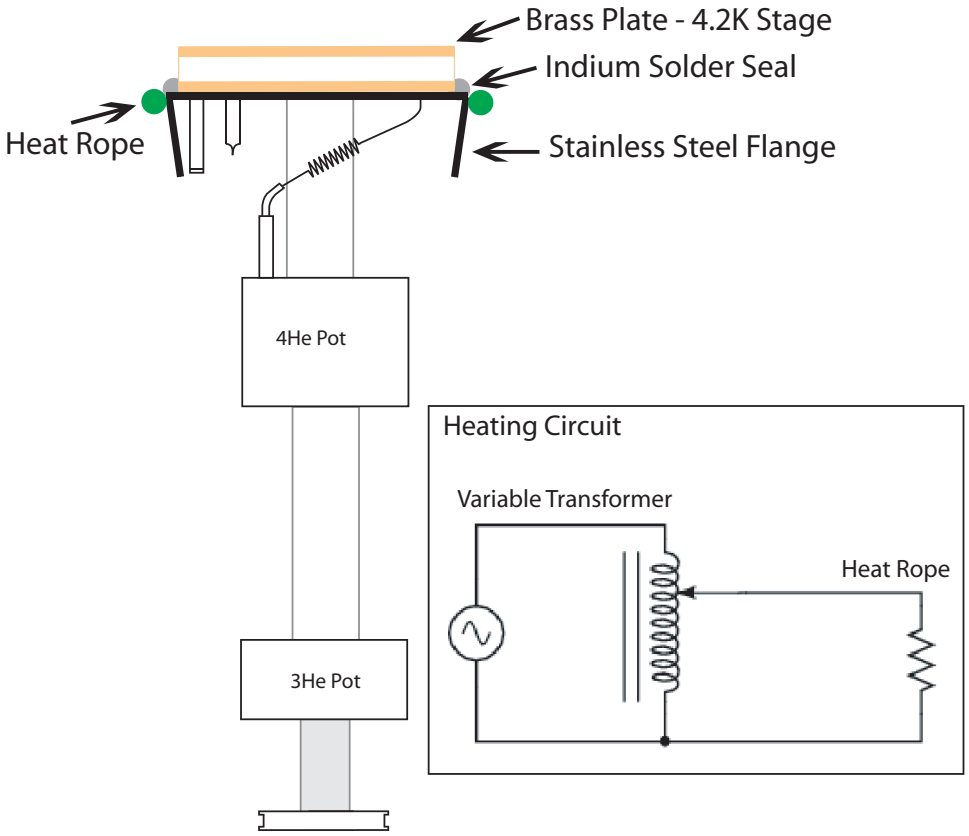

Figure B.4: Schematic of the lower section of the He3 cryostat. The 4.2K brass plate is soldered to the stainless steel vacuum flange using In wire as solder. The figure also illustrate the position of the heat rod when the soldering circuit is set in place. The bottom right corner shows the circuit used to melt the indium solder with a controllable heat.

and the fact that RC filters are thermally anchored at the 4.2K stage, extra precautions are required to avoid applying excessive heat to re-flow the indium solder, since this would damage the electrical lines.

Taking advantage of the low melting point for indium ($156.6°C$), we have developed an alternative way to apply a controllable amount of heat to the seal and the surrounding metals, which allows for the indium to melt but does not cause damage to electric lines, filters and all the necessary controls to run the fridge and monitor the temperature.

We use a high temperature heat rope purchased by McMaster-Carr (part number 3641K22) capable of reaching a temperature of $480°C$. Using a heat rope has two fundamental advantages; it can be powered with an adjustable voltage, which allows for controlling the produced heat, and it can be set in place so to heat up the interested metal surfaces evenly.

As shown in Fig. B.4, the heat rope was placed along the circumference of the vacuum flange using a hose clamp and then electrically connected to a *Powerstat* Variable Transformer produced by Superior Electric. The variable transformer provides a simple, rugged method of controlling electrical voltage, current and power, by taking in utility line voltage and providing continuously adjustable output voltage. To keep the applied heat to a minimum, the applied voltage is slowly raised until the indium seal begins to melt. Once all the material has melted, a metal brush was used to remove it and to clean the surface. Subsequently we reduced the heat, we then prepared the surface for a new soldering by applying a small amount of acid flux, and then we set in place a clean section of indium wire along the full circumference of the flange. We then re-applied heat until the indium was fully melted and a new seal was formed. Once cooled we proceeded in cleaning the area to remove excess acid flux that, over time, could cause damage to the structure.